UNIONE EUROPEA

Ministero dell'Istruzione dell'Università e Ricerca

UNIVERSITÀ DEGLI STUDI DI SALERNO

DIPARTIMENTO DI INGEGNERIA INDUSTRIALE

Dottorato di Ricerca in Ingegneria Meccanica

X Ciclo N.S. (2008-2011)

"Models for design and control of a solar-hybrid vehicle with a tracking solar roof"

Ing. Cecilia Pisanti

Il Tutor	*Il Coordinatore*
Ch.mo Prof. Gianfranco Rizzo	*Ch.mo Prof. Vincenzo Sergi*

…a coloro che amo e che mi amano

TABLE OF CONTENTS

LIST OF FIGURES

LIST OF TABLES

NOMENCLATURE

ACRONYMS

AFR	Air to Fuel Ratio
APV	Area photovoltaic panels
AR	Air Ratio
AU	Astronomical unit
B	Battery pack
Dof	Degrees of freedom
DP	Dynamic programming
EG	Electric Generator
EM	Electric Motor
EMS	Energy management strategy
EN	Electric Node
GA	Genetic algorithm
HEV	Hybrid electric vehicle
HSV	Hybrid solar vehicle
ICE	Internal combustion engine
PKM	Parallel Kinematics Machine
PV	Photovoltaic panels
RB	Rule – Based strategy
SDP	Stochastic Dynamic Programming
SOC	State of charge
VMU	Vehicle management unit
VR	Virtual reality

SYMBOLS

α_s	Solar altitude
β	Tilt angle
δ	Solar declination
d_0	Earth – Sun distance
E	Equation of time
E_b	Direct solar radiation
E_d	Diffuse solar radiation
E_r	Reflected solar radiation
E_s	Global solar radiation

φ	Latitude
γ_s	Solar azimuth
γ_v	Azimuth of the surface
h_d	Daily angle
h_{sun}	Hour sun angles
$I_{b0,d0}$	Mean instantaneous direct and diffuse radiation
Λ	Longitude
λ_{mr}	Longitude of the place considered
λ_{rf}	Longitude of reference
m_0	Air mass at sea level
m_z	Air mass in the place considered
Ω	Hour angle
$\tau_{b,d}$	Transmittance of direct and diffuse radiation
Θ	Angle of incidence
θ_z	Zenith
$R_{b,d,r}$	Factor angle of direct, diffuse and reflected radiation.
P	Albedo

CHAPTER 1

1 Introduction: solar energy and PV systems

1.1 Introduction

Our planet faces significant challenges in the twenty-first century because energy consumption is expected to double globally during the first half of this century. Faced with increasingly constrained oil supplies, humanity must look to other sources of energy, such as solar, to help us meet the growing energy demand (Figure 1).

A useful measure of the level of a country's development is through its energy consumption and efficiency. Excessive fossil fuel energy use not only has caused severe and growing damage to the environment from greenhouse gas emissions and oil spills, but also has brought political crises to countries in the form of global resource conflicts and food shortages.

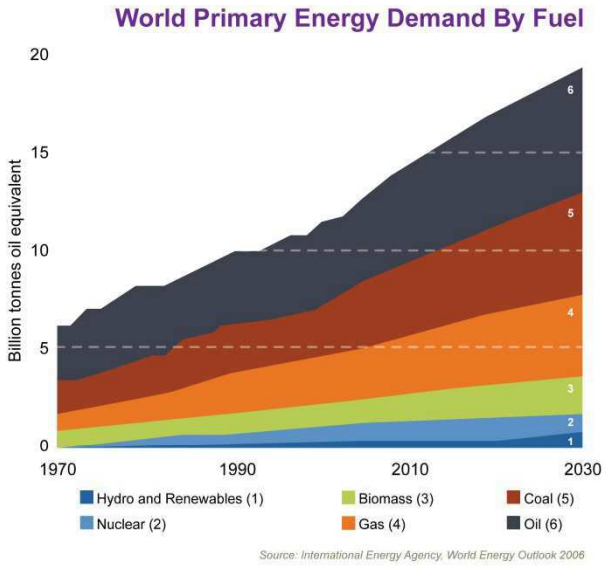

Figure 1 – World primary energy demand by fuel.

Solar and other forms of renewable energy offer a practical, clean, and viable solution to meet our planet's growing environmental and energy challenges.

Solar radiation is the most important natural energy resource because it is a renewable, free and largely diffused source. The Sun provides the Earth with an enormous amount of energy. A pictorial view of the potentialities of photovoltaic: the areas defined by the dark disks shown in Figure 2 could provide more than the world's total primary energy demand (assuming a conversion efficiency of 8%).

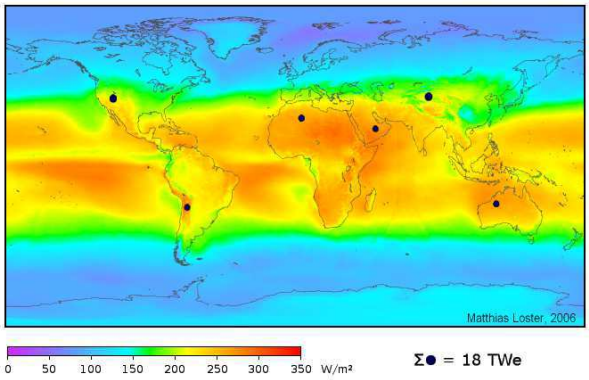

Figure 2 – Distribution of solar energy in the world.

Naturally, the Sun has always held the attention of humanity and been the subject of worship by many cultures over the millennia, such as the Egyptians, Incans, Greeks, and Mayans, among many others. The potential of solar energy to produce heat and electricity to be supplied for our modern economies in a variety of productive activities has been widely demonstrated but not yet widely adopted around the globe due to relatively cheap fossil fuels. The main problem of this kind of energy source is that it is not constant during the day and not readily dispatched. In contrast, modern lifestyles demand a continuous and reliable supply of energy. However, there are ways to overcome these shortfalls.

In this chapter the elements that compose global solar irradiance, the geometrical relationship between the Sun and the Earth and solar technologies are presented.[1]

1.2 Geometric relationship

The amount and intensity of solar radiation reaching the Earth's surface depends on the geometric relationship of the Earth with respect to the Sun. Figure 3 shows this geometric relationship and its effects for different seasons in both hemispheres.

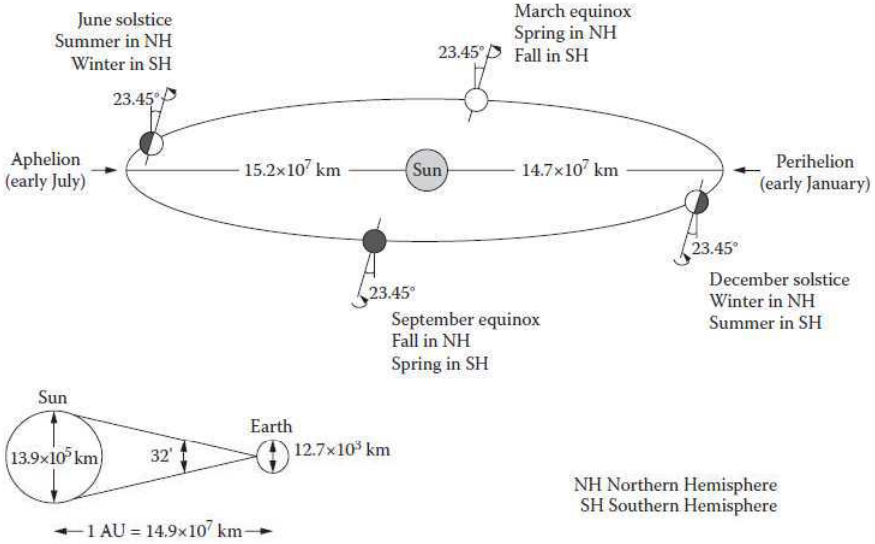

Figure 3 – Earth- sun geometric relationship.

The position of the Sun, at any moment at any place on Earth, can be estimated by two types of calculations: first, by simple equations where the inputs are the day of the year, time, latitude, and longitude, and, secondly, by calculations through complex algorithms providing the exact position of the Sun.

1.2.1 Earth – sun distance

The Earth has a diameter of 12.7 × 103 km, which is approximately 110 times less than the Sun's.

The Earth orbits approximately once around the Sun every 365 days. The Earth's orbit's eccentricity is very small, about 0.0167, which causes the elliptical path to be nearly circular. The elliptical path of the Earth varies from 14.7 × 107 km in early January—the closest distance to the

Sun, called perihelion (to 15.2 × 107 km in early July) the farthest distance, called aphelion. The average Earth–Sun distance of 14.9 × 107 km is defined as the astronomical unit (AU), which is used for calculating distances within the solar system. However, the Earth is about 4% closer to the Sun at the perihelion than the aphelion. The Sun subtends an angle of 32′ on the Earth at a 1 AU distance.

Eq. (1) gives the Earth–Sun distance (d_0) in astronomical units with a maximum error of ±0.0001

$$d_0 = \left(\frac{r_0}{r}\right)^2 = 1.000110 + 0.03422\cos h_d + 0.00128\sin h_d + \\ + 0.000719\cos 2h_d + 0.000077\sin 2h_d \quad (1)$$

where r_0 is equal to 1 AU, r is the Earth–Sun distance, h_d is the daily angle in radians given as

$$h_d = 2\pi\frac{n-1}{365} \quad (2)$$

and n is the day of the year ($1 \le n \le 365$); for example if 18th February is the day considered, i=18 n=31+18=49, where 31 are the number of the days of January.

A simpler calculation of d_0 is given by an experimental equation :

$$d_0 = 1 + 0.033\cos\left(\frac{360n}{365}\right) \quad (3)$$

1.2.2 Earth coordinate system

Any location on Earth is described by two angles, latitude (φ) and longitude (λ). Figure 4 sketches the Earth coordinate system indicating the latitude and longitude as constant lines. The latitude corresponds to the elevation angle between a hypothetical line from the center of Earth to any point on the surface and its projection on the equator plane. Latitude values fall between -90° <φ< 90°; latitude is zero at the equator, 90° at the northern pole, and –90° at the southern pole. As for the longitude angle, imaginary lines extended from pole to pole are called meridians; these lines are at constant longitude. For each meridian crossing the equator's circle, there is an angle assigned.

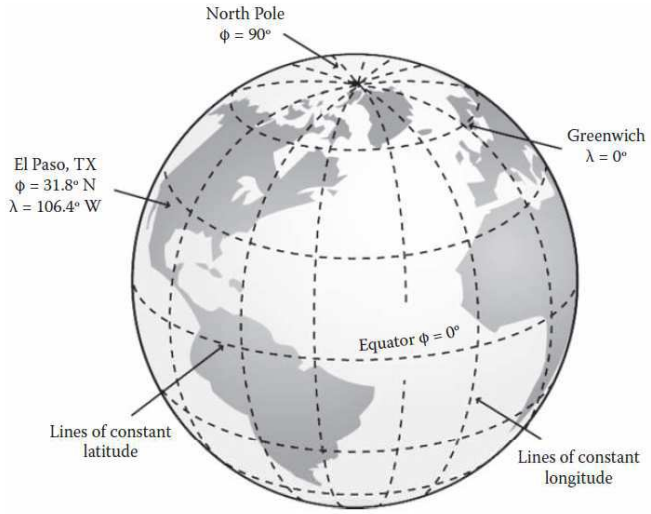

Figure 4 – Earth coordinate system [1]

The meridian passing through the old Royal Astronomical Observatory in Greenwich, England, is the one chosen as zero longitude and known as the Prime Meridian. Longitudes are measured from 0 to 180° east of the Prime Meridian and 180° west (or –180°). For a particular location, the imaginary line that divides the sky in two and passes directly overhead is then the location's meridian. The abbreviations a.m. and p.m. come from the terms ante meridian and post meridian, respectively. To determine the amount of solar energy received on any point of the Earth's surface, more than latitude and longitude angles are needed.

When the Earth coordinate system is extended to the celestial sphere, it is possible to calculate the exact position of the Sun with respect to a horizontal surface at any point on Earth. The celestial sphere is an hypothetical sphere of infinite radius whose center is the Earth and on which the stars are projected. This concept is used to measure the position of stars in terms of angles, independently of their distances. The north and south celestial poles of the celestial sphere are aligned with the northern and southern poles of the Earth.

Similarly to the latitude concept on Earth, the declination δ (Figure 5) on the celestial sphere is measured northward or southward from the celestial equator plane. Lines of constant declination run parallel to the

celestial equator and run in numerical values from +90° to –90°. Because of the Earth's yearly orbital motion, the Sun appears to circle the ecliptic up to an inclination of 23.45° to the celestial equator, –23.45° < δ < 23.45° with δ = 0° at the equator for the equinoxes, –23.45° on the December solstice, and +23.45° on the June solstice.

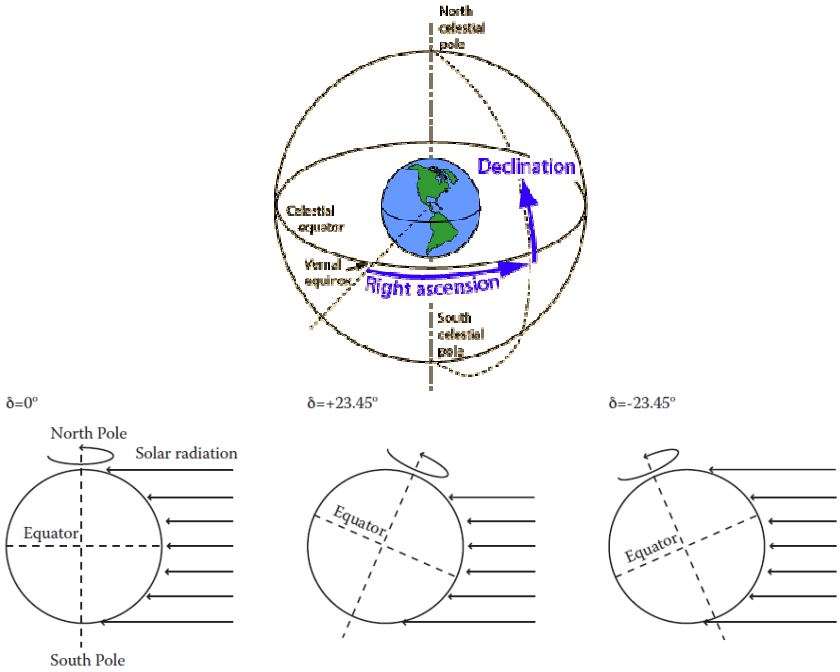

Figure 5 – Sun declination and Right ascension.

There are several expressions to calculate declination but in this work is used Cooper's equation:

$$\delta = 23.45 \cdot \left(\frac{360}{365} \cdot (n+284) \right) \qquad (4)$$

1.2.3 Angles for Sun's position

In addition to the fixed celestial coordinate systems on the sky, to describe the Sun's position with respect to an horizontal surface on Earth at any time, other angles are presented: solar altitude (α_s), zenith (θ_z), solar azimuth (γ_s), and hour angles (ω). Figure 6 presents the geometric

relationships among these angles to determine the position of the Sun in the sky at any time.

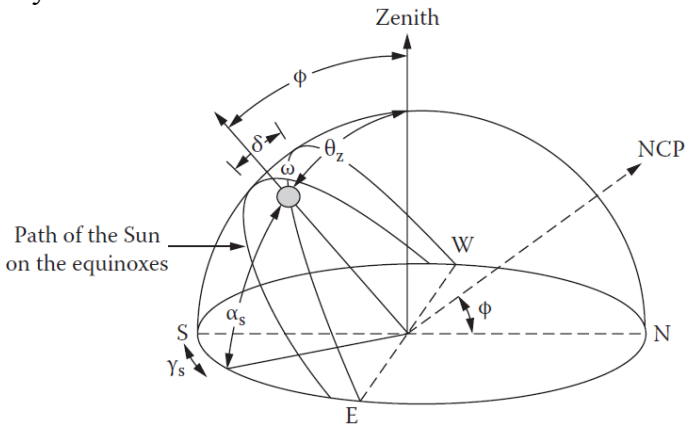

Figure 6 – Main solar angles.

The solar altitude is measured in degrees from the horizon of the projection of the radiation beam to the position of the Sun. When the Sun is over the horizon, $\alpha_s = 0°$ and when it is directly overhead, $\alpha_s = 90°$. In most latitudes, the Sun will never be directly overhead; that only happens within the tropics. Because the zenith is the point directly overhead and 90° away from the horizon, the angle of the Sun relative to a line perpendicular to the Earth's surface is called the zenith angle, θ_z, so that

$$\alpha_s + \theta_z = 90 \quad (5)$$

and the zenith angle is given by:

$$\cos\theta_z = \sin\varphi \sin\delta + \cos\delta \cos\varphi \cos\omega \quad (6)$$

Also, there is a strong relationship between the solar azimuth and hour angles. The solar azimuth is the angle on the horizontal plane between the projection of the beam radiation and the north–south direction line. Positive values of γ_s indicate the Sun is west of south and negative values indicate when the Sun is east of south. The hour angle ω is the angular distance between the Sun's position at a particular time and its highest position for that day when crossing the local meridian at the solar noon. Because the Earth rotates approximately once every 24 hours, the hour angle changes by 15° per hour and moves through 360° over the course of the day. The hour angle is defined to be zero at solar noon, a negative value before crossing the meridian, and a positive after crossing.

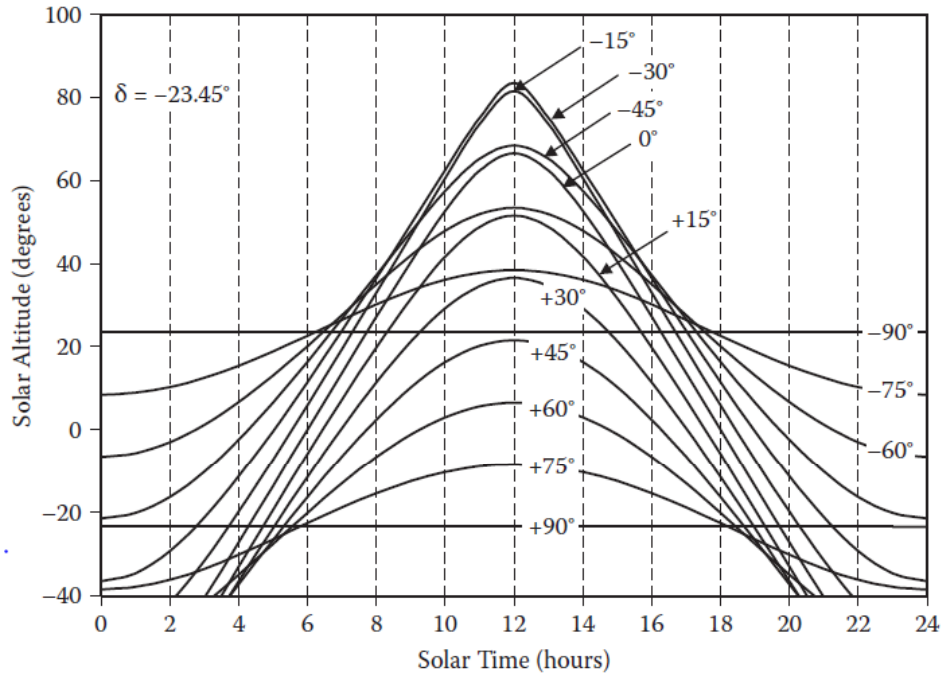

Figure 7 - Solar altitude during the day for different latitudes during the December solstice when δ =–23.45°.[1]

As mentioned before, the length of the day varies for all latitudes during the year and, with this, the solar altitude α_s also changes hourly and daily. This angle can be calculated in terms of declination δ, latitude φ, and hour angles ω by using the equation (10), knowing that:

$$E=-10.1\cdot \sin\left(360\frac{2d+31}{366}\right)-6.9\sin\left(360\frac{d}{366}\right) \quad (7)$$

$$h_{sun} = hour + \frac{E - 4(\lambda_{rf} - \lambda_{mr})}{60} \quad (8)$$

$$\omega = 15 \cdot h_{sun} - 180 \quad (9)$$

$$\sin\alpha_s = \sin\varphi \sin\delta + \cos\varphi \cos\delta \cos\omega \quad (10)$$

E is known as the equation of time as function of the day, computed by the equation (7), λ_{rf} is the longitude of reference instead λ_{mr} is the longitude of the place considered. The solar azimuth angle, γ_s, can be calculated in terms of declination δ, latitude φ, and hour angles ω.

$$\sin \gamma_s = \frac{\sin \omega \sin \delta}{\sin \theta_z} \quad (11)$$

All these equations are presented in the work [2].

1.2.4 Position of the Sun with respect to a surface

The maximum solar energy collection is achieved when the Sun's rays are perpendicular to the collecting area (i.e., parallel to the surface normal). This can be achieved only when solar tracking systems are used to modify the slope or the surface azimuth or both angles during the collector's operation. The angle between the surface and the horizontal plane is called tilt angle and it is signed as β.

However, these systems are more expensive than the fixed ones due to their moving components. The fixed-β collectors are the most practical receivers and the most widely installed throughout the world. In order that the fixed-β collectors capture most of the annual incoming solar radiation, the surfaces must always be tilted facing the equator. The maximum solar altitude for each day is reached around noon when the solar azimuth angle is around zero (i.e., around the north–south line). For dates when the Sun is at low maximum solar altitudes, it is convenient to install the collectors with greater β to minimize the angle between the Sun's rays and the normal surface. For periods when the Sun follows higher paths through the sky, β must be small. Several criteria might be used to select β, such as maximum collection for the greatest energy demand period or optimization during the whole year. Another option could be having several positions in the systems so that the collector could be manually fixed at several β values over the year.

The last angle to be defined, which completely relates the solar radiation to a surface, is the **solar incidence angle** (θ). This is the angle between the solar radiation beam incident on a surface and the imaginary line normal to such a surface. At θ = 0°, the Sun's rays are perpendicular to the surface and, when θ = 90°, the Sun's rays are parallel to the surface. Maximum solar gain for any solar intensity is achieved when the incidence angle is zero because the cross section of light is not spread out and also because surfaces reflect more light when the light rays are not perpendicular to the surface. Figure 8 presents the geometric relationship between the solar angles in an horizontal surface and in one tilted by a β

slope. The angle of incidence can be calculated by any of the following equation:

$$\cos\theta = \cos\theta_z \cos\beta + \sin\theta_z \sin\beta \cos(\gamma_s - \gamma) \quad (12)$$

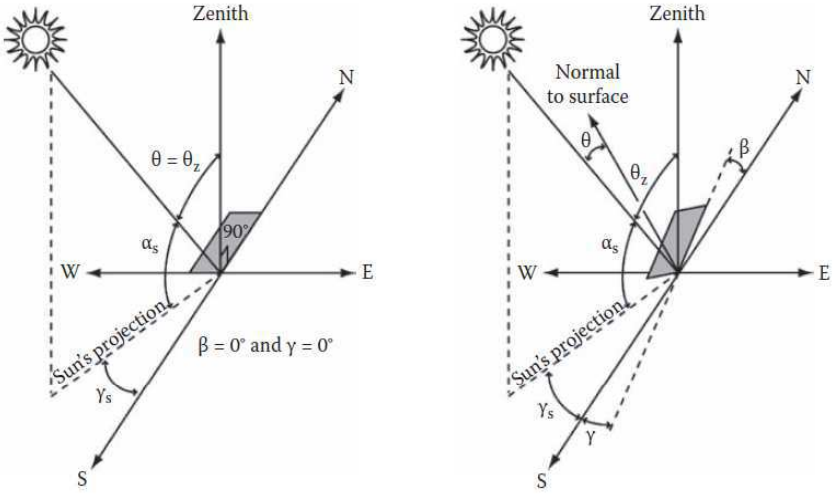

Figure 8 - Solar angles for an horizontal solar, facing south (left), and a tilted surface, facing south, with an arbitrary one azimuth angle.

1.3 Solar radiation

Solar radiation is a general term for the electromagnetic radiation emitted by the sun. It is possible to capture and convert solar radiation into useful forms of energy, such as heat and electricity, using a variety of technologies. The technical feasibility and economical operation of these technologies at a specific location depends on the available solar radiation or solar resource.[3]

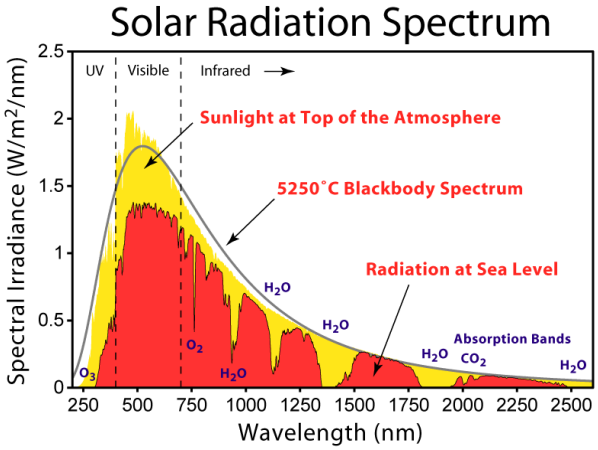

Figure 9 – Spectral irradiance depending on wavelength

Every location on Earth receives sunlight at least part of the year. The amount of solar radiation that reaches any one "spot" on the Earth's surface varies according to these factors:

- geographic location;
- time of day;
- season;
- local landscape;
- local weather.

Because the Earth is round, the sun strikes the surface at different angles ranging from 0º (just above the horizon) to 90º (directly overhead). When the sun's rays are vertical, the Earth's surface gets all the possible energy. The more slanted the sun's rays are, the longer they travel through the atmosphere, becoming more scattered and diffuse. Because the Earth is round, the frigid Polar Regions never get a high sun, and because of the tilted axis of rotation, these areas receive no sun at all during a large part of the year.

The Earth revolves around the sun in an elliptical orbit and is closer to the sun during part of the year. When the sun is nearer the Earth, the Earth's surface receives a little more solar energy. The Earth is nearer the sun when it is summer in the southern hemisphere and winter in the northern hemisphere. However the presence of vast oceans moderates the hotter summers and colder winters one would expect to see in the southern hemisphere as a result of this difference.

The 23.5º tilt in the Earth's axis of rotation is a more significant factor in determining the amount of sunlight striking the Earth at a particular location. Tilting results in longer days in the northern hemisphere from the spring (vernal) equinox to the fall (autumnal) equinox and longer days in the southern hemisphere during the other six months. Days and nights are both exactly 12 hours long on the equinoxes, which occur each year on or around March 23 and September 22.

Countries like the United States, which lie in the middle latitudes, receive more solar energy in the summer not only because days are longer, but also because the sun is nearly overhead. The sun's rays are far more slanted during the shorter days of the winter months. Cities like Denver, Colorado, (near 40º latitude) receive nearly three times more solar energy in June than they do in December.

The rotation of the Earth is responsible for hourly variations in sunlight. In the early morning and late afternoon, the sun is low in the sky. Its rays travel further through the atmosphere than at noon when the sun is at its highest point. On a clear day, the greatest amount of solar energy reaches a solar collector around solar noon.

1.3.1 Diffuse, Direct and Reflected Solar Radiation

The global solar radiation is composed by direct, diffuse and reflected radiation. First it must be explained the difference between direct, diffuse and reflected radiation.

Direct radiation is also sometimes called "beam radiation" or "direct beam radiation". It is used to describe solar radiation traveling on a straight line from the sun down to the surface of the earth.

Diffuse radiation, on the other hand, describes the sunlight that has been scattered by molecules and particles in the atmosphere but that has still made it down to the surface of the earth.

Direct radiation has a definite direction but diffuse radiation is just going any which way. Because when the radiation is direct, the rays are all travelling in the same direction, an object can block them all at once. This is why shadows are only produced when direct radiation is blocked.

When the sky is clear and the sun is very high in the sky, direct radiation is around 85% of the total insulation striking the ground and diffuse radiation is about 15%. As the sun goes lower in the sky, the percent of diffuse radiation keeps going up until it reaches 40% when the

sun is 10° above the horizon. Atmospheric conditions like clouds and pollution also increase the percentage of diffuse radiation. On an extremely overcast day, pretty much 100% of the solar radiation is diffuse radiation. Generally speaking, the larger the percentage of diffuse radiation, the less the total insulation.

The percentage of the sky's radiation that is diffuse is much greater in higher latitude, cloudier places than in lower latitude, sunnier places. Also, the percentage of the total radiation that is diffuse radiation tends to be higher in the winter than the summer in these higher latitude, cloudier places. The sunniest places, by contrast, tend to have less seasonal variation in the ratio between diffuse and direct radiation.

Reflected radiation describes sunlight that has been reflected off of non-atmospheric things such as the ground. Asphalt reflects about 4% of the light that strikes it and a lawn about 25%. However, solar panels tend to be tilted away from where the reflected light is going and reflected radiation rarely accounts for a significant part of the sunlight striking their surface.

Global insulation is the total insulation: direct + diffuse + reflected light. Often people use it to refer to the total insulation on a horizontal surface and if they want to talk about the total radiation striking a surface with some specific tilt, they will say something like "total insulation on an XYZ° tilt", etc. **Normal radiation** describes the radiation that strikes a surface that is at a 90° angle to the sun's rays. As discussed in sun angle and insulation, by constantly keeping our solar collectors at a 90° angle with the sun, we maximize the direct radiation received on that day.

The air mass is another important factor: the air mass coefficient defines the direct optical path length through the Earth's atmosphere, expressed as a ratio relative to the path length vertically upwards, i.e. at the zenith. The air mass coefficient can be used to help characterize the solar spectrum after solar radiation has traveled through the atmosphere.

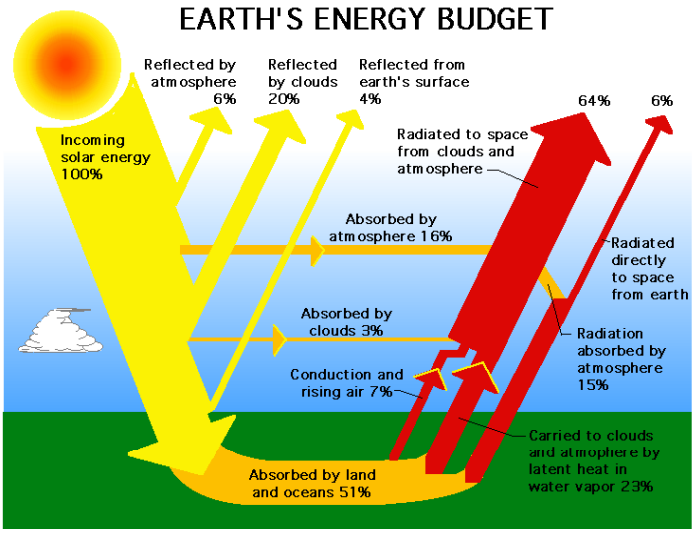

Figure 10 – Main components of the global solar irradiation.

The mean instantaneous direct radiation on horizontal surface is about $I_0=1356\frac{W}{m^2}$. Considering that p_0 is the pressure at sea level, p_z is the pressure of the place considered, it is possible to calculate the air mass at sea level (m_0) and the air mass in the place considered (m_z).

$$m_0=\frac{1}{\sin(\alpha_s)} \quad (13)$$

$$m_z=m_0\frac{p_z}{p_0} \quad (14)$$

The transmittance of direct radiation is τ_b:

$$\tau_b=e^{-\frac{0.65m_z}{2}-\frac{0.095m_z}{2}} \quad (15)$$

$$I_{bn}=I_0\cdot\tau_b \quad (16)$$

At this point is possible to calculate the direct solar radiation considering that θ is the angle of incidence. In fact the direct solar radiation on a tilted surface can be computed by next equation:

$$E_b=I_{bn}\cos(\theta) \quad (17)$$

In Figure 11 the percent ratio between the solar energy captured and the direct solar energy is presented:

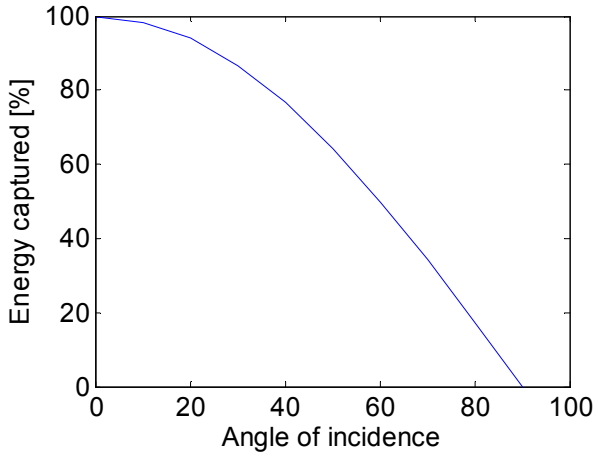

Figure 11 – Per cent ratio between energy caught and direct solar energy.

To compute the solar radiation diffuse it is necessary to know the factor angle of diffuse radiation (R_d), the mean instantaneous direct radiation on horizontal surface (I_{d0}) and the orientation of the horizontal surface respect the south (γ_v).

$$R_d = (1 + \cos\beta)/2 \quad (18)$$

$$\tau_d = 0.2710 - 0.2939\tau_b \quad (19)$$

$$I_{d0} = I_0 \sin(\alpha_s) \cdot \tau_d \quad (20)$$

So the diffuse radiation is:

$$E_d = I_{d0} R_d \quad (21)$$

The reflected radiation is evaluated starting from the albedo coefficient ρ, which varies depending on the type of material and is presented in tables for easy consultation, and the following relationship is used to compute it:

$$E_r = (I_{b0} + I_{d0}) R_r \quad (22)$$

where R_r is a coefficient referring to the reflect radiation.

$$R_r = \rho(1 - \cos\beta)/2 \quad (23)$$

Finally can be computed the global solar radiation;

$$E_s = E_b + E_d + E_r \quad (24)$$

1.4 PV system

Photovoltaic (PV) solar cells as they are often referred to, are semiconductor devices that convert sunlight into direct current (DC) electricity. Groups of PV cells are electrically configured into modules and arrays, which can be used to charge batteries, operate motors, and to power any number of electrical loads. With the appropriate power conversion equipment, PV systems can produce alternating current (AC) compatible with any conventional appliances, and operate in parallel with and interconnected to the utility grid.

1.4.1 Historical notes

The first conventional photovoltaic cells were produced in the late 1950s, and throughout the 1960s were principally used to provide electrical power for earth orbiting satellites.

In the 1970s, improvements in manufacturing, performance and quality of PV modules helped to reduce costs and opened up a number of opportunities for powering remote terrestrial applications, including battery charging for navigational aids, signals, telecommunications equipment and other critical, low power needs.

In the 1980s, photovoltaic became a popular power source for consumer electronic devices, including calculators, watches, radios, lanterns and other small battery charging applications. Following the energy crises of the 1970s, significant efforts also began to develop PV power systems for residential and commercial uses both for stand-alone, remote power as well as for utility connected applications. During the same period, international applications for PV systems to power rural health clinics, refrigeration, water pumping, telecommunications, and off-grid households increased dramatically, and remain a major portion of the present world market for PV products. Today, the industry's production of PV modules is growing at approximately 25 percent annually, and major programs in the U.S., Japan and Europe are rapidly accelerating the implementation of PV systems on buildings and interconnection to utility networks.

1.4.2 How photovoltaic cells work

A typical silicon PV cell is composed of a thin wafer consisting of an ultra-thin layer of phosphorus-doped (N-type) silicon on top of a thicker layer of boron doped (P-type) silicon. An electrical field is created near the top surface of the cell where these two materials are in contact, called the P-N junction. Since the top of the cell must be open to sunlight, a thin grid of metal is applied to the top instead of a continuous layer. The grid must be thin enough to admit adequate amounts of sunlight, but wide enough to carry adequate amounts of electrical energy.

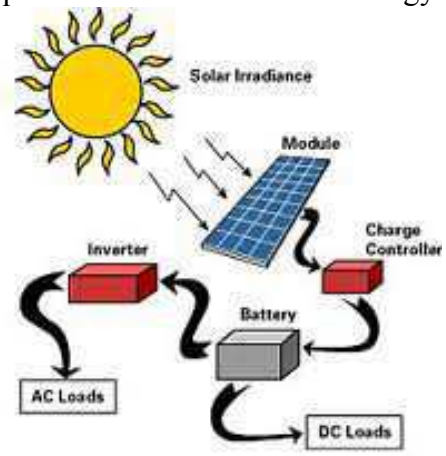

Figure 12 – A PV cell converts solar energy into electrical energy.

Light, including sunlight, is sometimes described as particles called "photons". As sunlight strikes a photovoltaic cell, photons move into the cell. When a photon strikes an electron, it dislodges it, leaving an empty "hole". The loose electron moves toward the top layer of the cell. As photons continue to enter the cell, electrons continue to be dislodged and move upwards. If an electrical path exists outside the cell between the top grid and the back plane of the cell, a flow of electrons begins. Loose electrons move out the top of the cell and into the external electrical circuit. Electrons from further back in the circuit move up to fill the empty electron holes. Most cells produce a voltage of about one-half volt, regardless of the surface area of the cell. However, the larger the cell, the more current it will produce. The resistance of the circuit of the cell will affect the current and voltage. The amount of available light affects current production. The temperature of the cell affects its voltage.

Regardless of size, a typical silicon PV cell produces about 0.5 – 0.6 volt DC under open-circuit, no-load conditions. The current (and power) output of a PV cell depends on its efficiency and size (surface area), and is proportional to the intensity of sunlight striking the surface of the cell. For example, under peak sunlight conditions a typical commercial PV cell with a surface area of 160 cm^2 (~25 in^2) will produce about 2 watts peak power. If the sunlight intensity were 40 percent of peak, this cell would produce about 0.8 watts.

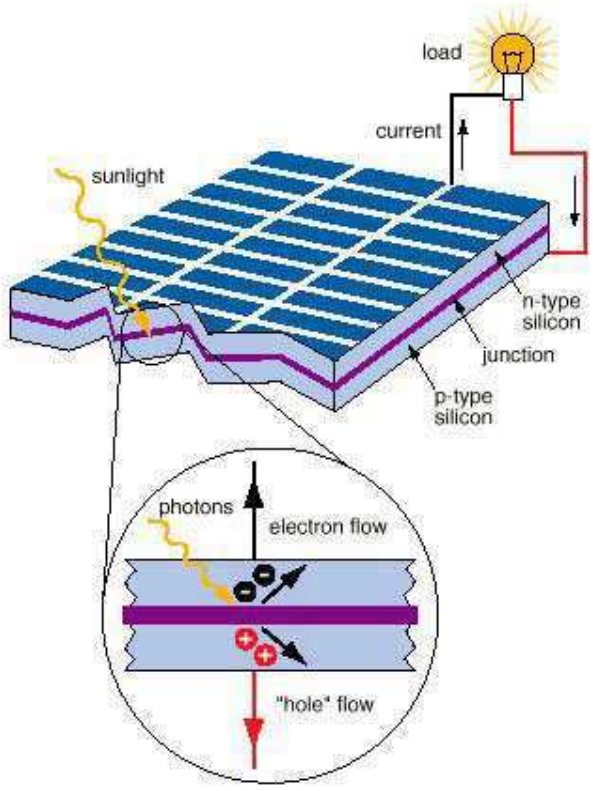

Figure 13 – Structure of a photovoltaic cell.

1.4.3 Types of photovoltaic cells

The four general types of photovoltaic cells are:

- **Single-crystal silicon**: Most photovoltaic cells are single-crystal types. To make them, silicon is purified, melted, and crystallized into ingots. The ingots are sliced into thin wafers

to make individual cells. The cells have a uniform color, usually blue or black.

- **Polycrystalline silicon** (also known as multicrystalline silicon): Polycrystalline cells are manufactured and operate in a similar manner. The difference is that lower cost silicon is used. This usually results in slightly lower efficiency, but polycrystalline cell manufacturers assert that the cost benefits outweigh the efficiency losses. The surface of polycrystalline cells has a random pattern of crystal borders instead of the solid color of single crystal cells.
- **Ribbon silicon**: Growing a ribbon from the molten silicon instead of an ingot makes ribbon-type photovoltaic cells. These cells operate the same as single and polycrystalline cells. The anti-reflective coating used on most ribbon silicon cells gives them a prismatic rainbow appearance.
- **Amorphous silicon** (abbreviated as "aSi," also known as thin film silicon): The previous three types of silicon used for photovoltaic cells have a distinct crystal structure. Amorphous silicon has no such structure. Amorphous silicon is sometimes abbreviated "aSi" and is also called thin film silicon. Amorphous silicon units are made by depositing very thin layers of vaporized silicon in a vacuum onto a support of glass, plastic, or metal.

1.4.4 Photovoltaic modules

For almost all applications, the one-half volt produced by a single cell is inadequate. Therefore, cells are connected together in series to increase the voltage. Several of these series strings of cells may be connected together in parallel to increase the current as well.

These interconnected cells and their electrical connections are then sandwiched between a top layer of glass or clear plastic and a lower level of plastic or plastic and metal. An outer frame is attached to increase mechanical strength, and to provide a way to mount the unit. This package is called a “module” or “panel” . Typically, a module is the basic building block of photovoltaic systems. Groups of modules can be interconnected in series and/or parallel to form an “array” by adding “balance of system” (BOS) components such as storage batteries, charge

controllers, and power conditioning devices, a complete photovoltaic system is obtained.

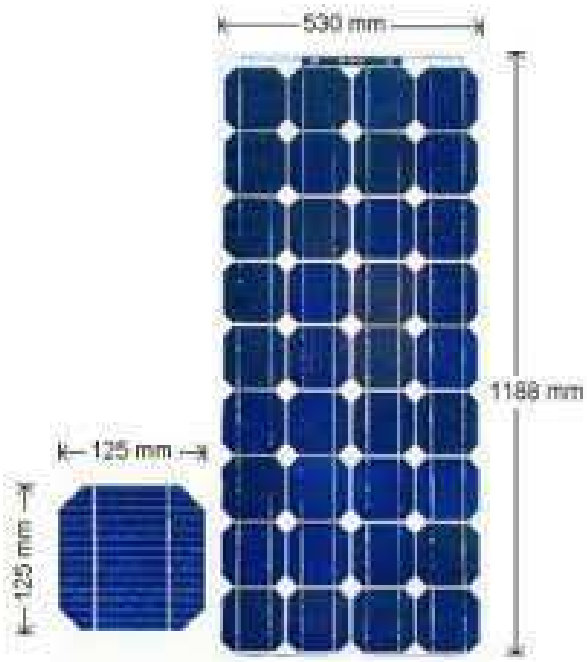

Figure 14 – Photovoltaic module.

1.5 Photovoltaic arrays

In many applications the power available from one module is inadequate for the load. Individual modules can be connected in series, parallel, or both to increase either output voltage or current. This also increases the output power. When modules are connected in parallel, the current increases. For example, three modules which produce 15 volts and 3 amps each, connected in parallel, will produce 15 volts and 9 amps (Figure 15).

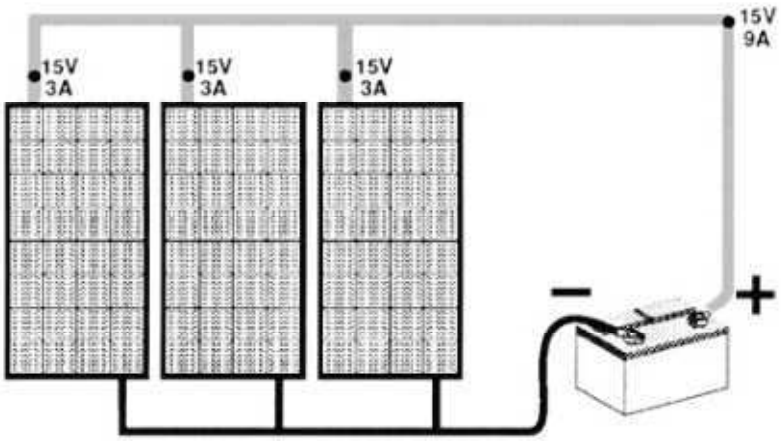

Figure 15 - Three Modules Connected in Parallel

If the system includes a battery storage system, a reverse flow of current from the batteries through the photovoltaic array can occur at night. This flow will drain power from the batteries. A diode is used to stop this reverse current flow. Diodes are electrical devices which only allow current to flow in one direction (Figure 16). A blocking diode is shown in the array in Figure 16.

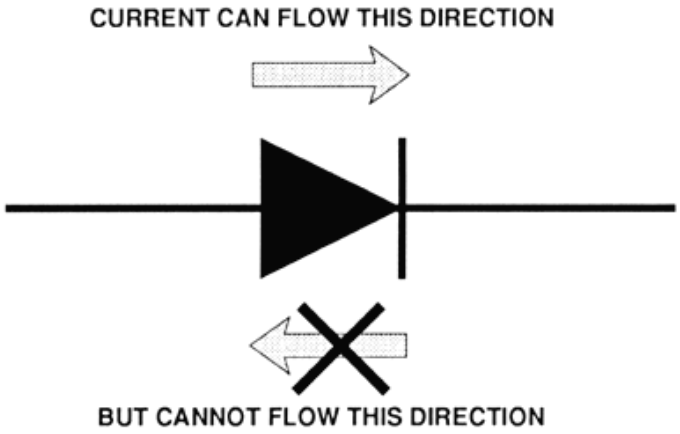

Figure 16 - Basic Operation of a Diode

Because diodes create a voltage drop, some systems use a controller which opens the circuit instead of using a blocking diode. If the same

three modules are connected in series, the output voltage will be 45 volts, and the current will be 3 amps.

If one module in a series string fails, it provides so much resistance that other modules in the string may not be able to operate either. A bypass path around the disabled module will eliminate this problem (Figure 17). The bypass diode allows the current from the other modules to flow through in the "right" direction. Many modules are supplied with a bypass diode right at their electrical terminals. Larger modules may consist of three groups of cells, each with its own bypass diode. Built in bypass diodes are usually adequate unless the series string produces 48 volts or higher, or serious shading occurs regularly.

Combinations of series and parallel connections are also used in arrays (Figure 18). If parallel groups of modules are connected in a series string, large bypass diodes are usually required.

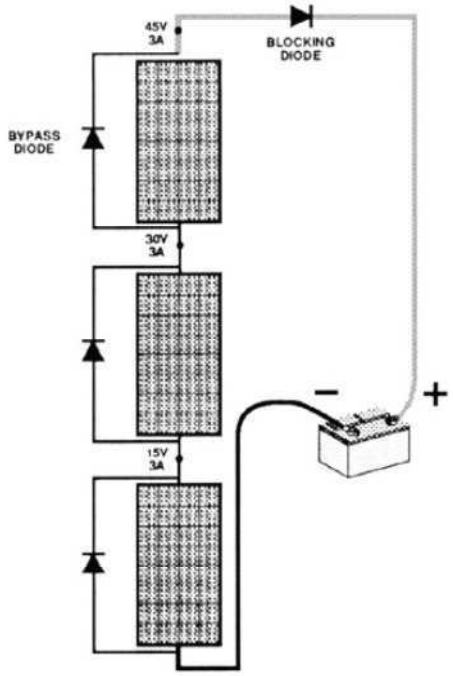

Figure 17 - Three Modules Connected in Series with a Blocking Diode and Bypass Diodes

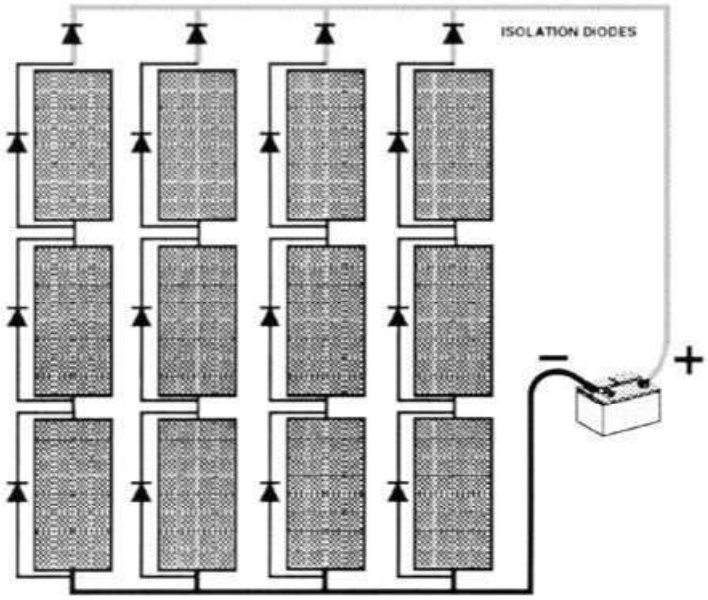

Figure 18 - Twelve Modules in a Parallel-Series Array with Bypass Diodes and Isolation Diodes.

1.5.1 Types of PV arrays

There are different types of PV arrays: the main types are:

- Flat – plate stationary arrays;
- Portable arrays;
- Tracking arrays.

1.5.1.1 Flat – plate stationary arrays

Stationary arrays are the most common. Some allow adjustments in their tilt angle from the horizontal. These changes can be made any number of times throughout the year, although they are normally changed only twice a year. The modules in the array do not move throughout the day (Figure 19). Although a stationary array does not capture as much energy as a tracking array that follows the sun across the sky, and more modules may be required, there are no moving parts to fail. This reliability is why a stationary array is often used for remote or dangerous locations.

Figure 19 – Adjustable tilted arrays.

1.5.1.2 Portable arrays

A portable array may be as small as a one square foot module easily carried by one person to recharge batteries for communications or flashlights. They can be mounted on vehicles to maintain the engine battery during long periods of inactivity. Larger ones can be installed on trailers or truck beds to provide a portable power supply for field operations (Figure 20).

Figure 20 – A portable array.

1.5.1.3 Tracking arrays

Arrays that track, or follow the sun across the sky, can follow the sun in one axis or in two (Figure 12). Tracking arrays perform best in areas with very clear climates. This is because following the sun yields significantly greater amounts of energy when the sun's energy is predominantly direct. Direct radiation comes straight from the sun, rather than the entire sky.

Figure 21 – Tracking array system.

CHAPTER 2

2 Hybrid electric and solar vehicles

2.1 Introduction

In the last years, increasing attention has been spent towards the applications of solar energy to cars. Various solar car prototypes have been built and tested, mainly for racing and demonstrative purposes [4][5]. Despite a significant technological effort and some spectacular outcomes, several limitations, such as low power density, unpredictable availability of solar source and energetic drawbacks (i.e. increase in weight and friction and aerodynamic losses due to additional components), cause pure solar cars to be still far from practical feasibility. On the other hand, the concept of a hybrid electric car assisted by solar panels appears more realistic [6][7][8][9][10]. In fact, due to relevant research efforts [11], in the last decades Hybrid Electric Vehicles (HEV) have evolved to industrial maturity. These vehicles now represent a realistic solution to important issues, such as the reduction of gaseous pollution in urban drive as well as the energy saving requirements.

The above considerations open promising perspectives with regard to the integration of solar panels with "pure" electric hybrid vehicles (i.e. "trihybrid" cars), with particular interest in the opportunity of storing energy even during parking phases. In spite of their potential interest, solar hybrid cars have received relatively little attention in literature [10]. An innovative prototype has been developed at Western Washington University [8][9] in the 90s, adopting advanced solutions for materials, aerodynamic drag reduction and PV power maximization with peak power tracking. Other studies and prototypes on solar hybrid vehicles have been presented by Japanese researchers [6][7] and at the Queensland University [12]. Although these works demonstrate the general feasibility of such an idea, detailed presentation of results and performance, along with a systematic approach to solar hybrid vehicle design, seem still missing in literature. Therefore, appropriate methodologies are required to address both the rapid changes in the technological scenario and the

increasing availability of innovative, more efficient components and solutions. A specific difficulty in developing a Hybrid Solar Vehicle (HSV) model relates to the many mutual interactions between energy flows, power-train balance of plant and sizing, vehicle dimension, performance, weight and costs, whose connections are much more critical than in either conventional or hybrid electric vehicles. Preliminary studies on energy flows in an HSV has been recently conducted by the authors [13][14].

2.2 Sustainable mobility

Sustainable Mobility issues are gaining increasing attention both among specialists and in public opinion, due to the major impact of automotive systems on carbon dioxide production, climate changes and fossil fuel depletion. In fact is possible to notice that:

- The oil price is going to increase and is subject to large and unpredictable oscillations.

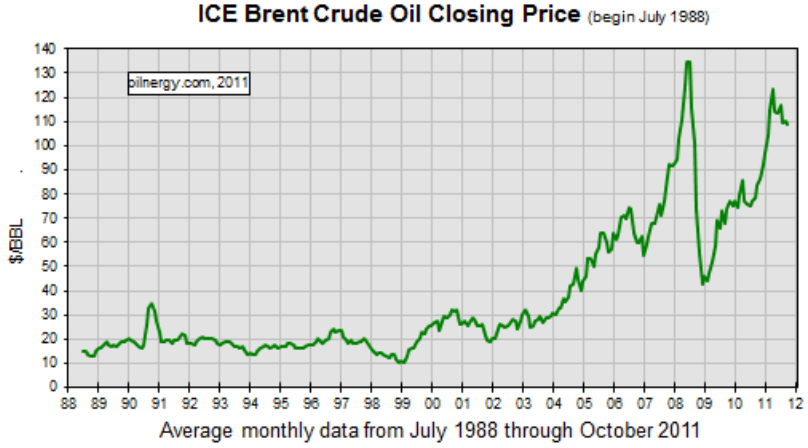

Figure 22 – Trend of oil price from 1988 to 2011

- The degree of electrification is expected to grow significantly in next years in terms of fleet distribution.

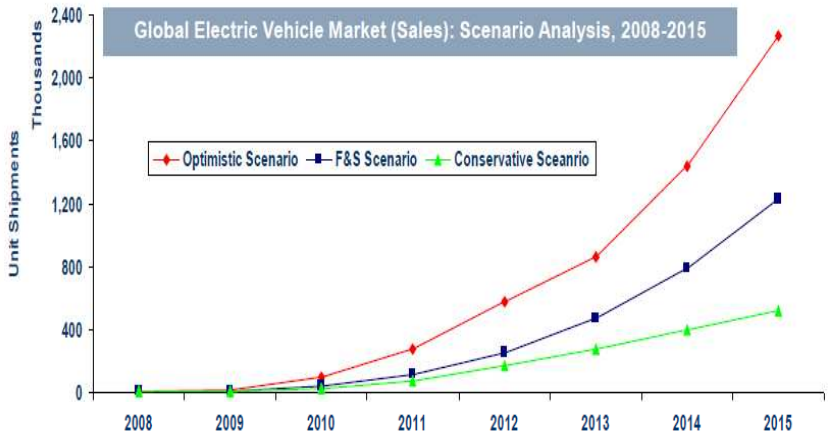

Figure 23 – Trend of degree of electrification from known days to next future.

- There is a growing demand for mobility especially in especially in countries such as China and Indi: the factor of world population is 1/3 in Chindia, so it represent a considerable contribute.

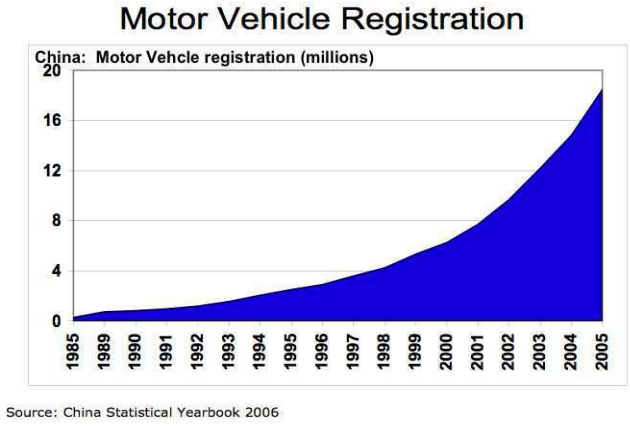

Figure 24 – The growth of motor vehicle registration in china

- The oil production will reach the peak in the next feature in the west of Europe, while it could be already falling in several countries.

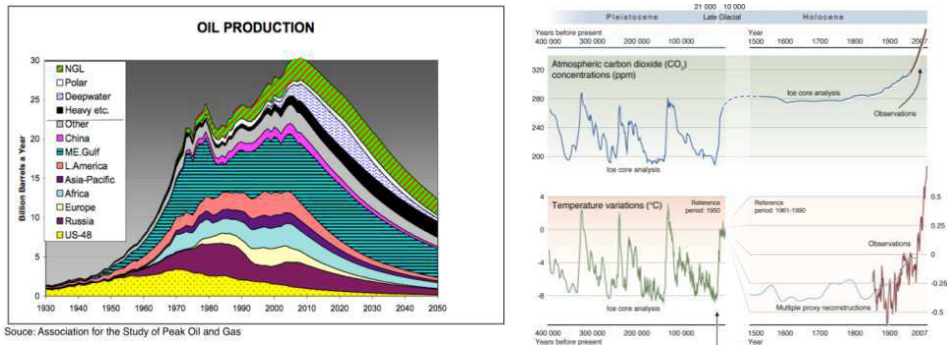

Figure 25 – Trend of oil production from the past to the future.

- There is a strong correlation between CO_2 and mean temperature: in fact measurements in last 150 years evidence a significant increase of both CO_2 and temperature, and also CO_2 emission for transport is increased in last 30 years both in relative and absolute values and there could be dramatic consequences.

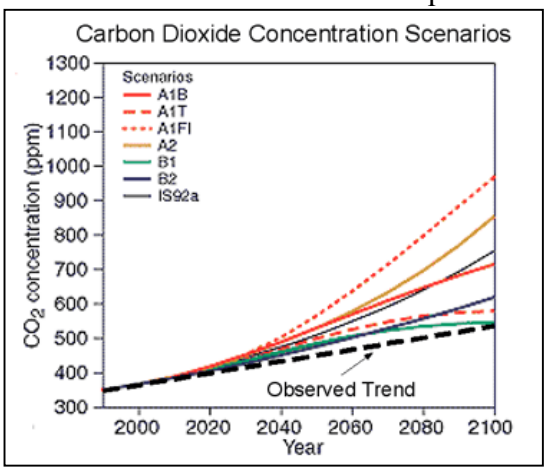

Figure 26 – Trend of CO_2 emissions and mean temperature

2.3 Hybrid electric vehicles

2.3.1 Background

The first hybrid electric vehicle dates back to 1899, developed by Ferdinand Porsche. The motivation for the development of an HEV was to overcome the limited range and the long recharge time of a pure electric vehicle [16]. Despite this early development, HEVs disappeared due to poor battery technology and cheap fuel. Meanwhile, significant improvement in the fuel economy of conventional powertrain was achieved by reducing the vehicle weight, and improving the engine efficiency through controlling fuelling, ignition and valve timing, etc. However these efforts were confined by the low conversion efficiency of the internal combustion engine (ICE). To further improve the energy efficiency of vehicle, researchers started look back to early HEVs for potential improvement, motivated by rising fuel price and environmental pollution.

Early development of HEV was led by several automobile manufacturers and research groups. A number of prototype hybrid test vehicles were built to experimentally validate the potentials of hybrid power train. The hybrid test vehicle, 'Mule', from the California Institute of Technology [17], was built to meet the contemporary conventional vehicle standards in its performance, ergonomics and emission. Outstanding technical improvements were in the smooth power blending between two energy sources, turning engine on and off, and fuel savings that contributed towards the hybrid technology advancement.

Through the development over a decade, Toyota was the first to release the mass-produced hybrid vehicle named Prius in 1997. Since its first release, Prius has achieved cumulative global sales of 2 million units by September 2010.

With growing popularity of HEVs, competitors have accelerated the release of their hybrid model in the market, releasing approximately 30 different models so far. Consumers' high demand for fuel efficient vehicle is evident, as reflected in the rapid growth in the total number of HEV sales in the U.S market, as shown in Figure 27. A slight decline in the sales is observed since 2008, partly due to the recession in the world's economy, and discontinuance of some of the HEV models. The market

forecast, however, expects the sales to rise from 2011 with release of new HEV models [18].

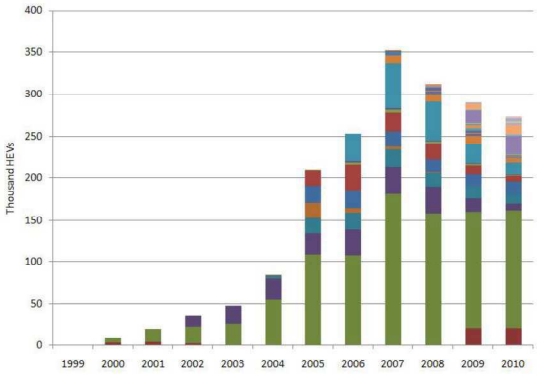

Figure 27 - Total HEV sales in U.S. between 1999 -2010 [18]

Hybrid configuration is not only limited to gasoline-electric combination. Other combinations such as Diesel-electric (e.g. Peugeot 3008 Hybrid4) and LPG electric (e.g. Hyundai Elantra hybrid) are already out in the market. More recently, research is being conducted on new potential combinations such as the pneumatic hybrid (compressed air & gasoline) [19] and solar hybrid [20][21], seeking for viable and energy efficient alternatives.

As discussed, increasing popularity and potential improvement indicate the promising future of hybrid vehicles, which warrant further research and development.

2.3.2 Main prototypes

Hybrid passenger cars arrived in the United States in model year 2000, following their introduction in Japan a few years earlier. First came was the two-seat Honda Insight, followed by the Toyota Prius in model year 2001.

Figure 28 – Honda Insight

Figure 29 – Toyota Prius 2001

Honda then introduced a hybrid version of its Civic sedan, and Toyota offered a second-generation Prius. Ford plans to introduce its first hybrid, a version of the Escape sport utility vehicle, in model year 2005. Several other major automakers now either offer HEVs or plan to do so in the near future.

Figure 30 – Ford Escape

Hybrid systems have also proved effective in buses and heavy trucks. For example, Oshkosh Truck Corporation has demonstrated a diesel-electric system that may significantly improve the fuel economy and driving range of military vehicles. As a bonus, hybrids can be devised to generate alternating current electricity for other applications such as plug-in power tools. General Motors, through its Allison Transmission Division, produces a diesel-electric hybrid drivetrain for transit buses.

Figure 31 - Coca-Cola hybrid electric truck

2.3.3 Configuration and features

Present-day hybrids are equipped with ICEs and electric motors. A hybrid's ICE engine, as in any ICE-powered car, produces power through continuous, controlled combustion that push down pistons connected to a rotating crankshaft. That rotating force (torque) is ultimately transmitted to the vehicle's wheels.

A hybrid's electric motor is energized by a battery, which produces power through a chemical reaction. The battery is continuously recharged by a generator that, like the alternator of a conventional car, is driven by the ICE [15].

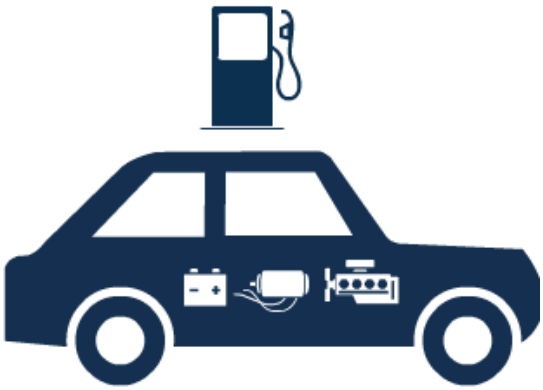

Figure 32 - Hybrid vehicles are powered by an alternative or a conventional fuel, and a battery, which is charged by regenerative braking.

Hybrids can have a parallel design, a series design, or a combination of both:

- In a **parallel design**, the energy conversion unit and electric propulsion system are connected directly to the vehicle's wheels. The primary engine is used for highway driving; the electric motor provides added power during hill climbs, acceleration, and other periods of high demand.
- In a **series design**, the primary engine is connected to a generator that produces electricity. The electricity charges the batteries, which drive an electric motor that powers the wheels. HEVs can

also be built to use the series configuration at low speeds and the parallel configuration for highway driving and acceleration.

In conventional vehicles, energy from deceleration is wasted as it dissipates. In some hybrid vehicles, regenerative braking systems capture that energy, store it, and convert it to electricity to help propel the vehicle, ultimately increasing overall efficiency. Some hybrids also use ultra-capacitors to extend the life of a hybrid vehicle's on-board battery system because they are better suited to capturing high power from regenerative braking and releasing it for initial acceleration.

2.4 Solar energy applied to hybrid vehicles

2.4.1 Why solar energy?

The main problem nowadays is to discover a possible solution to fossil fuel depletion and global warming. The solution has been partially done by Kyoto Protocol: an increased recourse to **Renewable Energy** (RE).

It is why solar energy has become a good alternative energy: solar energy is renewable, free and largely diffused, and Solar energy technologies include solar heating, solar photovoltaic, solar thermal electricity and solar architecture, which can make considerable contributions to solving some of the most urgent problems the world now faces.

Solar technologies are broadly characterized as either passive solar or active solar depending on the way they capture, convert and distribute solar energy. Active solar techniques include the use of photovoltaic panels and solar thermal collectors to harness the energy. Passive solar techniques include orienting a building to the Sun, selecting materials with favorable thermal mass or light dispersing properties, and designing spaces that naturally circulate air.

The importance of the use of solar technologies is underline by some data:

The Earth receives 174 petawatts (PW) of incoming solar radiation (insulation) at the upper atmosphere. Approximately 30% is reflected back to space while the rest is absorbed by clouds, oceans and land masses. The spectrum of solar light at the Earth's surface is mostly spread

across the visible and near-infrared ranges with a small part in the near-ultraviolet.

Earth's land surface, oceans and atmosphere absorb solar radiation, and this raises their temperature. Warm air containing evaporated water from the oceans rises, causing atmospheric circulation or convection. When the air reaches a high altitude, where the temperature is low, water vapor condenses into clouds, which rain onto the Earth's surface, completing the water cycle. The latent heat of water condensation amplifies convection, producing atmospheric phenomena such as wind, cyclones and anti-cyclones. Sunlight absorbed by the oceans and land masses keeps the surface at an average temperature of 14 °C. By photosynthesis green plants convert solar energy into chemical energy, which produces food, wood and the biomass from which fossil fuels are derived.

Yearly Solar fluxes & Human Energy Consumption	
Solar	3850000 EJ
Wind	2250 EJ
Biomass	3000 EJ
Primary energy use (2005)	487 EJ
Electricity (2005)	56.7 EJ

The total solar energy absorbed by Earth's atmosphere, oceans and land masses is approximately 3,850,000 exajoules (EJ) per year. In 2002, this was more energy in one hour than the world used in one year. Photosynthesis captures approximately 3,000 EJ per year in biomass. The

amount of solar energy reaching the surface of the planet is so vast that in one year it is about twice as much as will ever be obtained from all of the Earth's non-renewable resources of coal, oil, natural gas, and mined uranium combined.

Solar energy can be harnessed in different levels around the world. Depending on a geographical location the closer to the equator the more "potential" solar energy is available.

For all these reasons now an increasing importance is given to photovoltaic panels. This happens for many reasons:

- Their cost is decreasing, due to a fast growing diffusion of this technology, and their production is increasing (Figure 33);

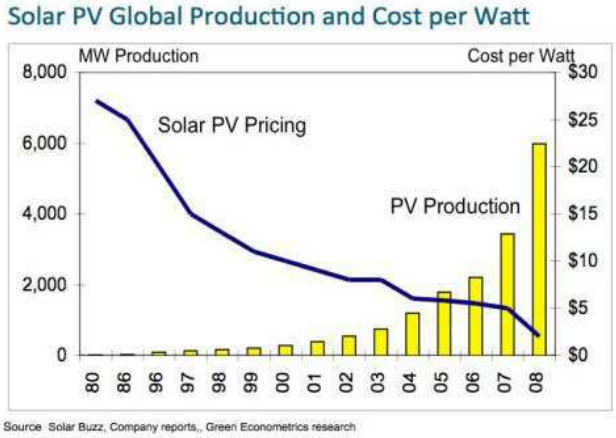

Figure 33 – Trend in PV production and price in last years

- PV efficiency is increasing (Figure 34).

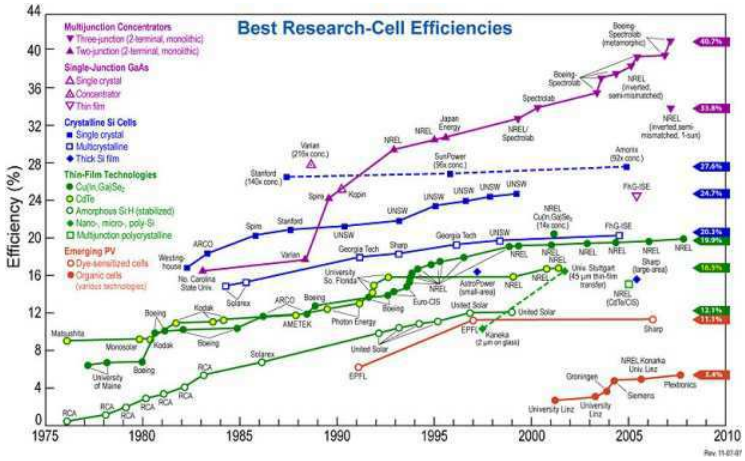

Figure 34 – Trend of PV efficiency

2.4.2 Hybrid Solar Vehicles

Despite their potential interest, solar hybrid cars have received relatively little attention in literature, particularly if compared with the great effort spent in last years toward other solutions, as hydrogen cars, whose perspectives are affected by critical issues regard to hydrogen production, distribution and storage.

Some prototypes have been developed in last decade in Japan [6][7], at Western Washington University [9], at the Queensland University (see for instance [23]) and, more recently, by the French company Venturi Figure 35.

Figure 35 - Venturi Automobiles' Astrolab, the first commercially available PV integrated hybrid.

A prototype of Solar Prius (Figure 36) has also been recently developed by Solar Electric Vehicles, equipped with a PV panel of 16% nominal efficiency. It has been estimated that the PV Prius can have a range based on solar power alone between 5 and 8 miles per day, and that it can consume between 17% and 29% less gasoline than the standard Prius.

Figure 36 – Toyota solar Prius

A prototype of HSV (Figure 37) has been developed at University of Salerno during Leonardo da Vinci project "Energy conversions systems

and environmental impact". The main characteristics of this prototype will be batter explained after.

Figure 37 – Micro-Vett porter van, the HSV prototype developed at University of Salerno

First of all it is obvious to do the comparison between hybrid electric vehicle and hybrid solar vehicle.

In principle it is clear to think that Hybrid Solar Vehicles (HSV) could sum up the advantages of HEV and solar power, by the integration of Photovoltaic Panels in a Hybrid Electric Vehicle. But it would be simplistic to consider the development of a HSV as the simple addition of photovoltaic panels to an existing Hybrid Electric Vehicle. In fact, the development of HEV's, despite it was based on well-established technologies, showed how considerable research efforts were required for both optimizing the power-train design and defining the most suitable control and energy management strategies. Analogously, to maximize the benefits coming from the integration of photovoltaic with HEV technology, it is required performing accurate re-design and optimization of the whole vehicle-powertrain system. In these vehicles, in fact, there are many mutual interactions between energy flows, propulsion system component sizing, vehicle dimension, performance, weight and costs, whose connections are much more critical than in conventional and also in hybrid cars.

Another difference between HEV and HSV may concern their structure. In fact, the prevailing architectures for HEV are parallel and

parallel-series, while in case of HSV the series structure seems preferable [20]. Despite some known disadvantages (higher efficiency losses due to more energy conversion stages), series structure is simpler and may offer some advantages:

- It more suitable for plug-in and V2G applications (the generator can be used as co-generator when the vehicle is parked at home).
- Due to absence of mechanical links between generator and wheels, very effective vibration insulation can be achieved, with fewer constraints for vehicle layout.
- Advanced techniques for noise reduction (i.e. active noise reduction) could be more easily applied, since the engine can work at fixed conditions.
- Engines specifically optimized for steady operation can be used (i.e. D.I. stratified charge engines, Micro gas turbine, and other solutions not suitable for classical vehicles due to lack of stability or low efficiency in the whole operating range).
- It is compatible with the use of in-wheel motors with built-in traction control and antiskid.
- It will potentially act as a bridge towards the introduction of hybrid fuel cell power trains.

A possible layout of a HSV with series structure is presented in Figure 38, with reference to the symbols presented in the nomenclature.

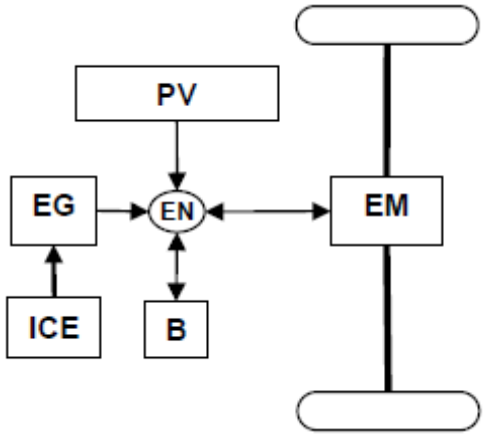

Figure 38 - Scheme of a series hybrid solar vehicle

In spite of solar energy is a great source of energy as it has been explained in previous paragraph, the use of solar energy on cars has been considered with certain skepticism by most users, including automotive engineers. This may be due to the simple observation that the net power achievable in a car with current photovoltaic panels is about two order of magnitude less than maximum power of most of today cars. But a more careful analysis of the energy involved demonstrates that this perception may be misleading. In fact, there is a large number of drivers utilizing daily their car for short trips and with limited power demand. For instance, some recent studies conducted by the UK government report that about 71 % of UK users reach their office by car, and 46 % of them have trips shorter than 20 minutes, mostly with only one person on board, i.e. the driver (www.statistics.gov.uk/CCI/nscl.asp?ID=8100).

In those conditions, the solar energy collected by solar panels on the car along a day may represent a significant fraction of the energy required for traction [14][22][21].

	Power [kW]	**Average power [kW]**	**Time [h/day]**	**Energy [kWh/day]**
Car	70	10	1	10
PV Panel	0.3	0.3	10	3
Ratio	0.004	0.03	10	0.3

Table 1 – Solar energy required by traditional cars daily used

The results presented in Table 1 explain why nowadays there is a growing interest for this other kind of sustainable mobility.

2.4.2.1 HSV prototype developed at University of Salerno

Also at University of Salerno has grown the interest for this kind of vehicles, enough to decide to develop an HSV. This activity has been started in the framework of the UE funded Leonardo project “Energy Conversion Systems and Their Environmental Impact”, a project with research and educational objectives. Many universities (the departments DIMEC and DIIE of University of Salerno, University of Mulhouse (F), Budapest (HU), Istanbul (TR) and Galati (RO)), industries (Elettrosannio and Auto Consulting) and authorities (“Parco scientifico e tecnologico di Salerno” and ERPAF) has participated at this project (2005-2007), and

many sponsors have been interested by it (Automobile club Salerno, Lombardini, CIMEP, Saggese).

The prototype has been realized changing an electric vehicle, Porter Piaggio Figure 37. A photovoltaic roof, an ICE-EG group, data acquisition and control system have been the main elements introduced.

Vehicle	**Piaggio Porter**
Length	3.370 m
Width	1.395 m
Height	1.870 m
Driver ratio	1:4.875
Electric Motor	**BRUSA MV 200 – 84V**
Peak Power	15 KW
Batteries	16 6V Modules Pb-Gel
Mass	520 Kg
Capacity	180 Ah
Photovoltaic Panels	**Polycrystalline**
Surface APV	1.44 m^2
Weight	60 kg
Efficiency (including converter)	0.1
Electric Generator	**Yanmar S 6000**
Power COP/LTP	5.67/6.92 kVA
Weight	120 kg
Overall weight (w driver)	
m_{HSV}	1950 kg

Table 2 - Actual HSV prototype specifications.

Vehicle lay-out is organized according to a series - hybrid architecture, as shown on Figure 39. With this approach, the photovoltaic panels PV (placed on vehicle roof as shown on Figure 37) assist the Electric Generator EG, powered by an Internal Combustion Engine (ICE), in recharging the Battery pack (B) in both parking mode and driving

conditions, through the Electric Node (EN). The Electric Motor (EM) can either provide the mechanical power for the propulsion .or restore part of the braking power during regenerative braking. In this structure, the thermal engine can work mostly at constant power, corresponding to its optimal efficiency, while the electric motor EM is designed to assure the attainment of the vehicle peak power.

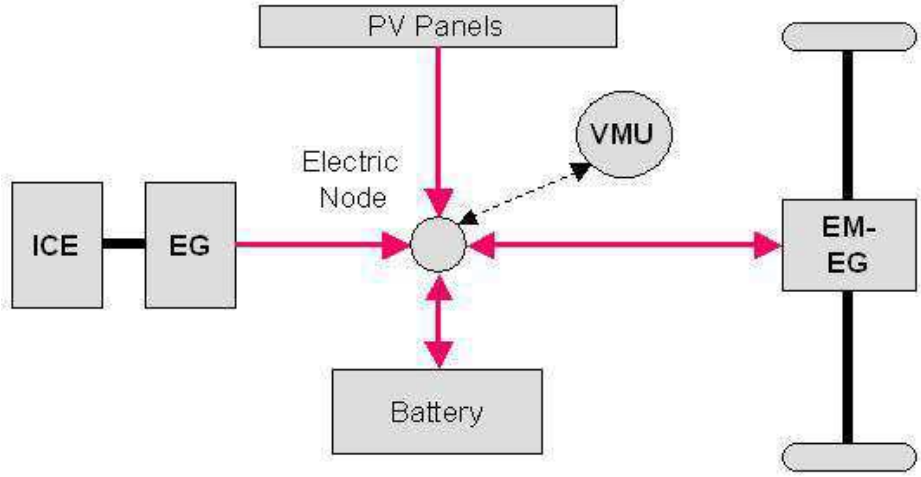

Figure 39 –Scheme of the series hybrid solar vehicle

There is also the vehicle management unit (VMU), a control system that established the energy flows and develops a start and stop system of ICE-EG, depending on the state of charge of the battery (SOC), the power required by the vehicle and the sun power.

Thanks to this prototype, it has been possible to make experiments for this kind of vehicle and to study problems. But, due to economic and time problems, this prototype is not the optimal solution: fuel consumptions of the actual configuration are little more than the ones of a Toyota Solar Prius.

Figure 40 – The HSV prototype at Motor Show Bologna in 2010.

This vehicle has participated to numerous trade fairs and exhibitions industry, such as Eco targa 2007 and Motor Show in Bologna in 2009 and 2010.

CHAPTER 3

3 Strategies for energy management of HSVs

3.1 Introduction

Until now in literature a little interest has been given to the hybrid solar vehicles. About HEV the main research focus is on minimizing fuel consumption by controlling the torque split between engine and motor. Even for HSV, main research activities focus on the better structure and control systems especially to have the most convenient fuel economy. As formerly discussed, the motivation behind their control is that significant fuel saving can be achieved by optimally utilizing the efficiencies of engine and electric motor, whose variations are large across the operating ranges. At the same time, the battery state of charge needs to be maintained. Formulating the control algorithm for determining the fuel efficient power split between two energy sources is referred to as the supervisory control or energy management problem.

In this chapter, the main control strategies, used also for the energy management of HEV, are examined. Control strategies may be classified into non-causal and causal controllers respectively. Furthermore, a second classification can be made among heuristic, optimal and sub-optimal controllers.

Great importance has given to three different strategies: Dynamic Programming DP, Genetic Algorithm GA and Rule–Based strategy RB. For each one the techniques of optimizations are described.

An HSV vehicle has been modeled, and for this model especially RB strategy and GA optimization have been applied to see the most convenient one to apply on HSV prototype developed at University of Salerno. So a comparison of RB strategy with the other two is shown, and its advantages and facilities are described through experimental data.

3.2 HSV modeling

A dynamic model for the simulation of a HSV and of the reference conventional vehicle over a driving cycle has been used:

- Vehicle longitudinal model (2 DoF);
- Simulation of engine thermal transient in start and stop operation;
- Modeling of HC emissions.

3.2.1 Vehicle longitudinal model

HSV simulation was performed by means of a longitudinal vehicle model developed under the following hypotheses:

- Drag (C_x) and rolling (C_r) coefficients are assumed equal to 0.4 and 0.02, respectively;
- The drag force is considered acting on vehicle center of gravity;
- Overall transmission efficiency η_{tr} is set to 0.9;
- Rotational inertia is accounted for increasing vehicle weight by 10%, therefore effective mass M_{eff} equals 1.1 M_{HSV}.

The resulting longitudinal model relates requested power at wheels to the road load, as follows:

$$P_W=W_{HSV}\cdot g\cdot v\cdot[C_r\cos\alpha+\sin\alpha]+0.5\rho C_x A v^3+M_{eff}\frac{dv}{dt}v \quad (25)$$

where α and v are the road grade and vehicle speed, respectively. For non-negative P_w values, the mechanical power requested to the EM is:

$$P_{EM}=\frac{P_W}{\eta_{tr}} \quad \text{if } P_W\geq 0 \quad (26)$$

P_{EM} can also be expressed as function of power contributions coming from electric generator, battery and PV array, as follows:

$$P_{EM}=\eta_{EM}\left(P_{EM}\cdot\eta_{AC/DC}+P_B+P_{PV}\right) \quad \text{if } P_W\geq 0 \quad (27)$$

where P_x is the power supplied by the x component, η_{EM} is the EM efficiency and $\eta_{AC/DC}$ is the AC/DC converter efficiency, here set to 0.92. For the current application, a 3.3 kW battery charger will be coupled to the existing one, thus allowing increasing the power drivable from the electric generator up to 5.4 kW.

On the other hand, when $P_w<0$, the regenerative braking mode is active, resulting in the following expression for the electrical energy delivered by the EM:

$$P_{EM}=P_W \cdot \eta_{EM} \cdot \eta_{tr} \quad \text{if} \quad P_w < 0 \qquad (28)$$

During regenerative braking, battery can be charged by EG and PV also, thus the following equation holds for negative Pw values:

$$P_B = P_{EM} - P_{EG} \cdot \eta_{AC/DC} \quad \text{if} \quad P_w < 0 \qquad (29)$$

3.2.2 Simulation of engine thermal transient

The effects of thermal transients have been accounted for assuming that:

- the ICE power does not reach instantaneously its reference value;
- the specific consumption depends not only on ICE power but also on the actual engine temperature.

The coolant temperature T has been assumed as engine reference temperature. The time variation of T has been estimated as a first order process by the following equation:

$$T(t)=T_{ss}+(T_{in}-T_{ss})e^{-\frac{t}{k}} \qquad (30)$$

The values of steady state temperature T_{ss} and of the time constant k have been assigned according to the following table, based on some experimental tests performed at the test bench:

ICE operation	T_{ss} [°C]	k [s]
ON	82	150
OFF	27	600

Table 3 – Values of steady state temperature and time constant k.

Fuel consumption Eq. (32) is estimated by correcting the steady-state values, corresponding to thermal equilibrium conditions, by a factor depending on the ratio between the actual and steady-state values of engine temperature.

$$P(t)=P_{ss}\cdot f\left(\frac{T_{eng}}{T_{ss}}\right) \quad (31)$$

$$SFC(t)=\frac{SFC_{ss}(P)}{f\left(\frac{T_{eng}}{T_{ss}}\right)} \quad (32)$$

In next figure it is possible to see the trend of **f** depending on time.

$$f=\beta_1+\beta_2 e^{-\left(\frac{T_{eng}}{T_{ss}}\right)\beta_3} \quad (33)$$

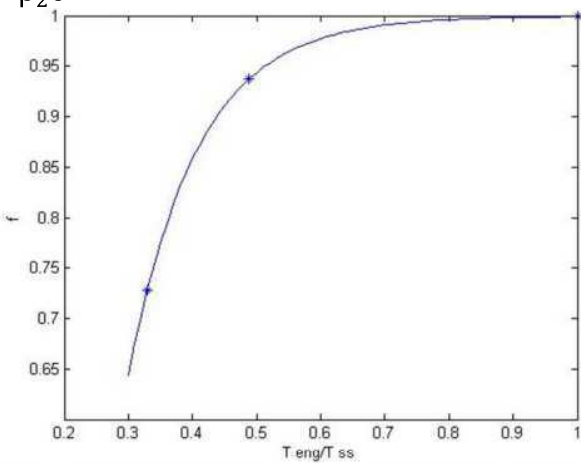

Figure 41 – Trend of function f (33).

3.2.3 Modeling of HC emissions

HC emissions are of major concern when frequent engine start/stop maneuvers are performed, as in the case of the ICE intermittent use proposed for HSV operation. Therefore, appropriate estimation of HC emissions during engine thermal transient could be useful to optimize energy management strategies also with respect to HC impact.

A simple model for HC emissions has been developed, based on the observation of experimental data measured on the engine test bench during a cold-start transient on a 4 cylinder SI engine 1.2 liters. The experimental trajectory, plotted in Figure 42, shows that HC tail pipe emissions exhibit a dramatic decrease during the first 20 seconds, starting from a very high HC concentration mainly due to fuel enrichment and eventually misfiring in the early stages of engine operation. Afterwards, the HC trend follows the catalyst thermal dynamics and approaches almost negligible concentration after about 400 s.

According to this behavior and to experimental evidences derived from literature analyses [24][25], in the first 20 seconds HC emissions are modeled as first order process, as follows:

$$HC(t)=HC_{ss}+(HC_{in}-HC_{ss})e^{\frac{t}{\tau}} \quad (34)$$

The initial value HC_{in} is computed by correcting the experimental value detected during the cold start test (about 1000 ppm) by a factor accounting for the actual engine temperature:

$$HC_{in}=HC_{in\_cold}\cdot f\left(\frac{T_{in}}{T_{in\_cold}}\right) \quad (35)$$

this way the model can predict HC emissions even in case of engine warm start. The correcting factor has been evaluated as function of a fuel delivery efficiency that expresses the ratio between actuated and effective Air to Fuel Ratio (AFR) [24]. Actually, the fuel delivery efficiency accounts for the wall wetting process and the effect of fuel enrichment on HC formation mechanism. Of course, assuming fixed engine speed, load and spark advance, the correcting factor mainly depends on the engine thermal state [24][26].

The steady state value HC_{ss} is computed by a look-up table expressing the dependence of HC concentration from engine temperature. Hence, when the early transient has been extinguished (i.e. after the first 20 s), the HC emissions are evaluated as function of the engine thermal state, regardless to gas composition and temperature and to catalyst thermal state.

Actually, the experimental data were measured imposing stoichiometric mixture and fixed spark advance, engine speed and load along the whole warm-up maneuver.

Therefore, if a similar transient is imposed for each engine start operation then gas composition and temperature are not affected by anything else than engine temperature. Consequently, also catalyst efficiency can be associated to engine temperature, even if its thermal dynamics differs from the engine.

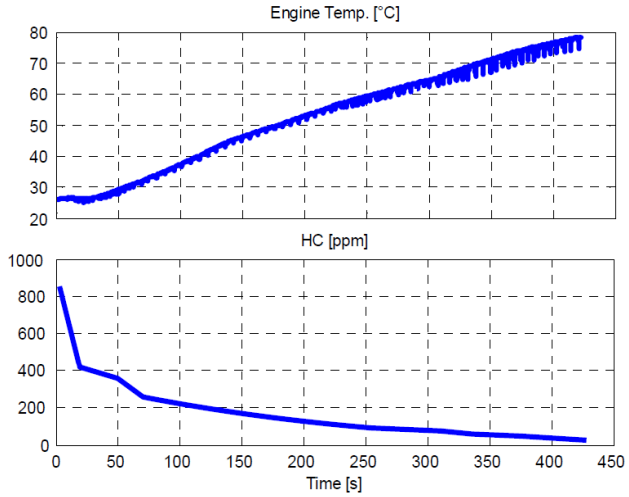

Figure 42 - Measurements of engine temperature and tail-pipe HC emissions along a cold-start maneuver on the engine test bench.

The results of a simulated engine start maneuvers are shown in Figure 43 in case of cold and warm operation. The figure evidences that the amounts of HC tail-pipe emissions differ in the two cases, due to the different temperature transients that in turn influence the catalyst light off time.

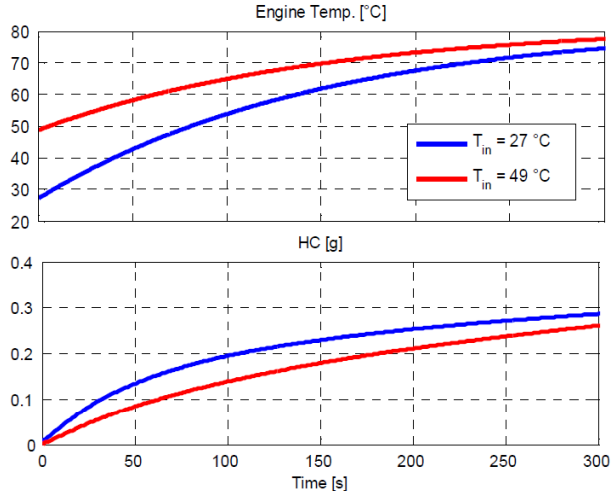

Figure 43 - Simulated engine temperature and tail-pipe HC emissions in case of cold (27 °C) and warm (49°C) engine start maneuver.

3.3 Optimal control strategy - Dynamic Programming

A commonly used technique for determining the globally optimal EMS is Dynamic Programming (DP) [23] [28] and [29]. Using DP, the finite horizon optimization problem is translated into a computation problem [30].

DP is applied over a known drive cycle in reverse manner to find the optimal engine and motor combination by searching through the discretized SOC grid [31][32]. With decreasing grid size, the resulting solution approaches the optimal solution and at the same time the computational burden increases. However, this method is still useful for benchmarking the maximum possible fuel saving. Also the resulting optimal control policy may be utilized as a basis for developing a rule-based strategy as in [33].

Note that, although the DP solution may appear as an unstructured result, in principle the technique results in an optimal solution for the EMS. Using DP it is rather straightforward to handle nonlinear constraints. However, a disadvantage of this technique is the relatively long computation time, due to the relatively large grid density required. The grid density should be taken high, because it influences the accuracy of the result. Furthermore, DP over a drive cycle is clearly infeasible to apply in real time since a full trip information is necessary a priori, as well as the fact that algorithm is very computationally demanding.

The aforementioned DP approaches are deterministic, and it is specific for a given drive cycle. In [34], the HEV power management problem is tackled using stochastic approach as previously applied in other automotive powertrain control problems such as in fuel consumption minimization for conventional powertrain [35].

In Stochastic Dynamic Programming (SDP), power demand from the driver is modeled as a random Markov process. Based on several sample drive cycles, the probability map of power transition is constructed. In order to do this, power demand is discretized into a finite set of torque and speed combination. Unlike in deterministic DP in which SOC boundary conditions act as hard constraint, the state of charge deviation is weighted in the cost function for fuel use as soft constraint, since exact terminal SOC cannot be met using the stochastic method. The control

policy is then derived by minimizing the expected total cost over an infinite horizon. In [34] is demonstrated that SDP performed better than the RB controller trained from the deterministic DP over multiple drive cycles.

However the main drawback of this method is that the discount factor for the cost along the horizon as well as the weight on the state of charge deviation penalty may affect the overall fuel minimization performance. SDP is further extended in [36] by imposing variable state of charge penalty which switches on and off so that it does not consistently penalize the fuel cost. The discount factor is eliminated from the problem formulation so that there is less number of parameters to be tuned compared to [34].

The advantage of SDP method is that the controller may moderately behave in other driving patterns as its Markov model is derived over a number of driving patterns in an average sense. However, there are parameters to be tuned to improve fuel economy and for the state of charge control. Also SDP cannot outperform the deterministic optimal controllers when it is provided with accurate future power demands.

This optimization strategy have not been adopted for the optimization of the HSV prototype for two main reasons:

- The optimization problem will be to mathematically hard;
- It is necessary to have a previously knowledge of the driving cycle, and this is not possible to know it each time.

3.4 Genetic algorithm

The Genetic Algorithms (GA) are random search methods operating in analogy to the mechanisms of natural selection and evolution of living species. The research is done by selecting, for each iteration, the individuals with the best degree of adaptation to the environment (domain of problem) and creating a new population through a random exchange of information between the more efficient elements. The processes performed by these algorithms to change the individuals are very similar to the main biological evolutionary mechanisms, i.e. sexual reproduction and genetic mutation. The GA has been designed and developed by J. Holland in 70s and

are one of the most commonly used methods in the Artificial Intelligence [37].

In Figure 44 the reproduction scheme of GA is presented [38][39]:

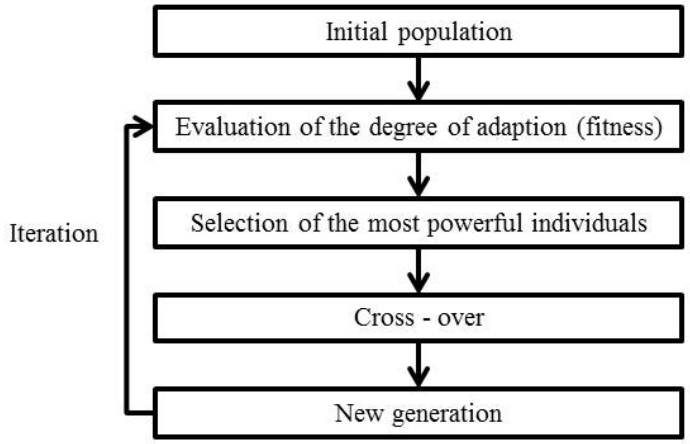

Figure 44 – Optimization with GA.

Firstly it is necessary to explain what fitness is**:** it is the level of the goodness of solutions. It is possible to divide fitness into:

- **Genotypic Fitness**: in the case of finding a minimum or a maximum of a real function, the fitness can be assumed coincident with the value of the function at each individual (variable).
- **Fitness phenotype**: in cases fitness is not suggested by the problem (i.e. classification problems), the criteria used for determining the Fitness "phenotype" should be adopted, i.e. the behavior of the individual employees in their environment.

At each individual a fitness value is assigned (0-2): the highest value is assigned to the individual that minimize the function.

The selection operation is based on the Darwinian theory of evolution, it seems likely that stronger individuals survive and transmit their genes to offspring.

Then, through the use of GA, the algorithm makes a random selection of a pair of individuals and it divides their chromosomes (string) random. The sub – strings are exchanged to produce two new chromosomes of a complete length.

It must be considered also the mutation that alters a gene on chromosome randomly, transforming the bits in a single-bit null and the opposite. It is the same that could happen in human reproduction.

At the end the new generation of individuals is generated. The new population will consist of new individuals, i.e. those generated through crossover and/or mutation, and individuals survived. Sometimes, it is taken the elitist reproduction procedures, in which it is guaranteed that a certain number of copies of the more performance is moved downward to the population.

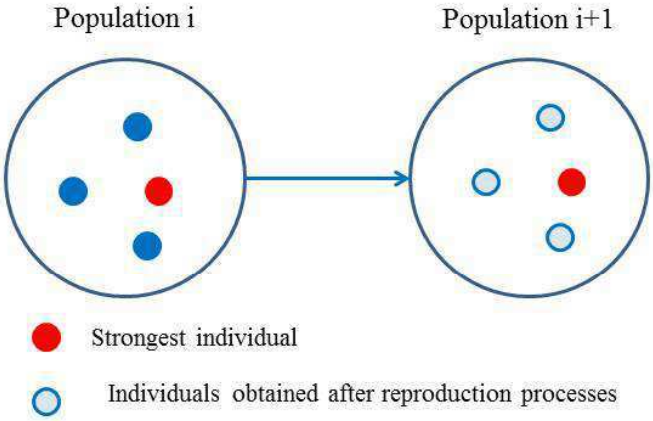

Figure 45- Population after optimization with GA.

This method is based on probabilistic, not deterministic, rules so it is a random search method. The search is performed on group of solutions, some of them have the highest degree of adaptation (fitness) to the problem, the others will simply other of the points of the domain: obviously the selection of individuals is based on the degree of adaptation, encouraging the "survival" of the most powerful (high fitness) ones; but there is the cross-over that generate new individuals combining the genotypes of the solutions "survived", encouraging creation of ever more powerful descendants. But GA make also periodic changes of random genetic solutions (mutations), allowing the creation of new individuals with different degree of adaptation [38].

Previously it has been said that the algorithm is not deterministic, in fact it is not able to assess whether the solution is optimal, since it does not has the concept of optimal solution, but better than the other (higher

fitness). On the other hand it is possible to see that evolutionary algorithms are very robust in terms of efficacy (ability to convergence) and efficiency (computational time compatible).

GA are used for many applications:

- Optimization: in the presence of complex functions (discontinuous, noisy, multimodal Pareto optimality);
- Machine Learning (Neural Networks i.e. education);
- Classification and Recognition (forms, images, sounds).

Like in others optimization algorithm, it is not always convenient to use GA for all optimization problems.

The main advantages are:

- More robust: there is no problem of entrapment in local minima (effectiveness) and operate efficiently;
- It is possible to solve multimodal optimization problems;
- They operate in the presence of discontinuous functions, since that they do not require the calculation of the gradient.

But it must be considered also the main disadvantage that is the necessity to have a time horizon of extensive research in order to ensure the effectiveness of the algorithm.

For the optimization of HSV prototype developed at University of Salerno this strategy has been adopted to optimize the electric generator, as it will be described in next paragraph.

3.4.1 Optimization of EG scheduling by means of GA

In case of intermittent ICE scheduling, the optimal EG power trajectory can be found by solving the following constrained optimization problem:

$$\min_X \int m_{f,HSV}(X)dt \qquad (36)$$

subject to the constraints

$$\Delta SOC_{day}=SOC_f-SOC_0+\Delta SOC_p=0 \qquad (37)$$

$$SOC>SOC_{min} \qquad (38)$$

$$SOC<SOC_{max} \qquad (39)$$

where $m_{f,HSV}$ is the HSV fuel consumption [kg], SOC_f and SOC_0 are the initial and final state of charge in the driving phase, respectively, and

ΔSOC_p is the SOC increase due to PV recharging during vehicle parking. It is worth mentioning here that driving and parking hours are set to 1 and 9, respectively.

The decision variables X include number of EG-on events NEG, along with corresponding starting time $t_{0,EG,i}$, duration $\Delta t_{EG,i}$ and EG power level $P_{EG,i}$, where i is the i-th EG-on event.

The first constraint (i.e. Eq. (37)) allows restoring the initial state of charge within the end of the day, also considering parking phases.

The other constraints (i.e. Eqs. (38)-(39)) were defined accounting for internal resistance dependence on battery state of charge. For lead-acid batteries in the SOC range [0.55 0.9] both charging and discharging resistances are fairly constant while being close to their minimum values [43]. Therefore in this analysis SOC_{min} and SOC_{max} were set to 0.55 and 0.9, respectively.

The problem stated by Eqs. (36)-(39) involves both integer (e.g. N_{EG}) and real variables, thus falling in the field of Mixed Integer Programming (MIP) problems. Among the several techniques that can be adopted to solve such problems, genetic algorithms (GA) is one of the most efficient [44] and has thus been selected for optimizing EG scheduling on a hybrid solar vehicle. The GA search was performed in MATLAB environment by means of the GAtbx tool developed by [37]. Details about GA optimization techniques can be found in the abundant literature on the topic, which the reader is addressed to [44][38][39].

For the current application, the following operating parameters were assumed for the GA search procedure:

Population size	70
Number of generations	100
Crossover probability	0.8
Mutation probability	0.033

Table 4 – GA operating parameters.

A binary representation of the decision variables was selected, as reported in Table 5.

Decision variable	Definition range	Precision	Number of bits
N_{EG}	[1 8]	1	3
t_{EG} (min)	$\left[0\ \frac{78}{N_{EG}}\right]$	$\frac{0.073}{N_{EG}}$	10
Δt_{EG} (min)	$\left[0\ \frac{78}{N_{EG}}\right]$	$\frac{0.073}{N_{EG}}$	10
P_{EG} (kW)	[0 43]	0.040	10

Table 5 – Binary representation of the optimization problem.

3.4.1.1 Optimization results

The GA optimization was applied to minimize the fuel consumption for a driving cycle composed of 4 ECE-EUDC cycles, as the one shown on Figure 46. HSV fuel consumption was simulated by means of the backward longitudinal vehicle model presented in paragraph 3.2.1. In the analysis the effect of thermal transients on ICE performance and HC emissions were also taken into account following the approach proposed in paragraphs 3.2.2 and 3.2.3. Table 2 lists the specifications of the reference HSV.

Table 6 summarizes the results of the current optimization task and also compares new outputs with previous ones obtained by derivative-based minimization (DBM) algorithm [42]. Such comparison indicates that the GA search method (i.e. column "GA" in Table 6) suggests a lower number of ECE-on events, which in turn results in a slightly higher fuel consumption and significantly lower HC emissions, as compared with classical method (i.e. column "DBM" in Table 6).

The reduction in HC emissions not only depends on the lower number of EG-on events, but also on the higher GA average engine temperature (see Table 6 and Figure 47), which of course determines a higher conversion effectiveness of the catalyst.

It is worth remarking that both HC emission levels reported in Table 6 are well below the EURO 5 gasoline emission standard (i.e. 0.1 g/km, [45]), thus confirming the benefits related to ICE intermittent use. Figure 48 shows the required power at wheels, optimal EG and battery trajectories and SOC variation. Particularly, Figure 48 indicates that the

GA search method was able to bound SOC variation within the desired limits (i.e. 0.55 and 0.9).

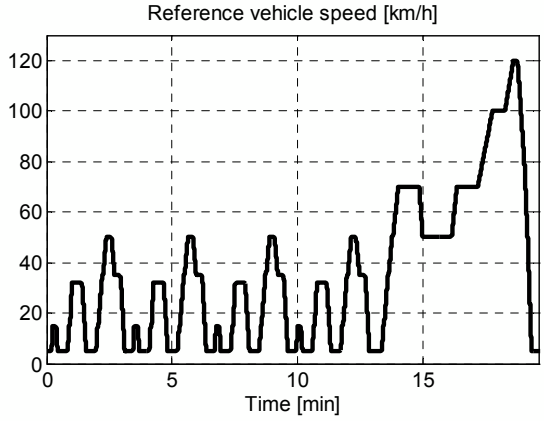

Figure 46 - ECE-EUDC driving module

Finally, a further optimization analysis was run considering an increase in PV horizontal area from 1.44 to 3 m2. Such configuration upgrade results in a fuel consumption reduction down to 2.28 kg.

Optimization outputs	DBM	GA
N_{EG}	4	3
Fuel consumption [kg]	2.41	2.48
HC emissions 1 (g)	1.13	0.85
Average engine temperature [°C]	65	68
Max SOC [/]	0.79	0.88
Min SOC [/]	0.65	0.58
HC emissions 2 (g/km)	0.025	0.018

Table 6 – Optimization analysis.

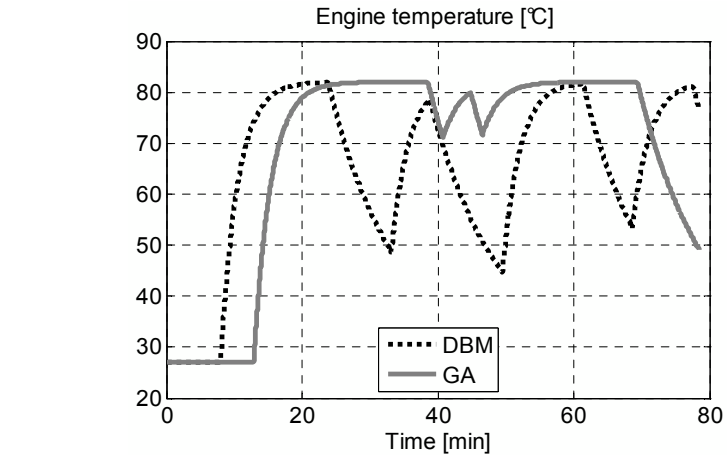

Figure 47 – Comparison between temperature trajectories simulated in DBM and GA optimization task.

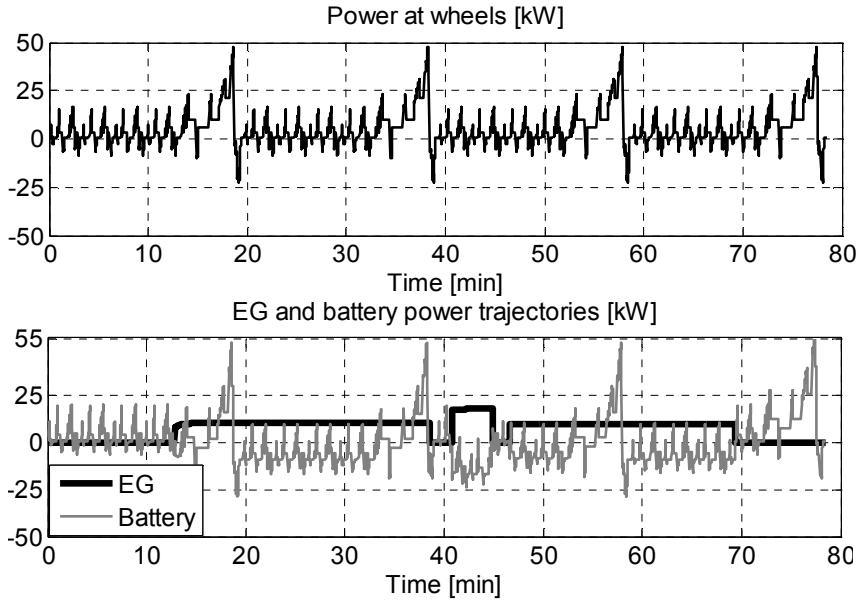

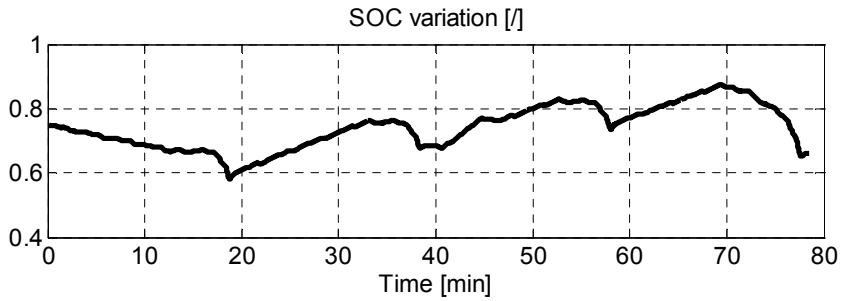

Figure 48 – Time trajectories yielded by the GA optimization

3.5 Rule – based strategy

Another optimization strategy is Rule-based strategy that is an heuristic method. This strategy has been considered efficient and convenient in the energy management of hybrid solar vehicles: this will be better explained in the rest of this chapter and, through a real application, in next chapter.

The RB control architecture consists of two loops, external and internal respectively:

- **external loop**: defines the desired final state of charge SOC_f (see Figure 49), to be reached at the end of the driving cycle to enable full storage of solar energy caught during the following parking phase (i.e., $E_{sun,p}$).
- **internal loop**: estimates the average power delivered by ICE-EG and SOC deviation (dSOC) from SOC_f as function of average traction power and $E_{sun,p}$.

Figure 49 provides a qualitative description of the start&stop strategy enabled by the above-described control loops. For sake of simplicity, in Figure 49 it is assumed that SOC_0=SOC_f and does not vary with time. The battery is initially depleted until SOC becomes lower than SOC_{lo} = SOC_f-dSOC. At this point ICE-EG is turned on at the assigned power level and switches off when the maximum threshold SOC_{up} = SOC_f+dSOC is reached. The procedure is repeated until the end of the driving cycle. It is worth mentioning here that effective final state of charge may differ from the desired SOC_f due to the difficulty of precisely

predicting the end of the driving phase. This consideration entails satisfying the following energetic constraint:

$$\Delta SOC_{up}+\Delta SOC_p<1 \quad (40)$$

where ΔSOC_p represents the state of charge increase subsequent to battery recharging performed by PV panels during parking phases.

The described control strategy relies, on one hand, on the online estimation of current SOC level and, on the other, on predicting or properly estimating over an assigned driving route. The following sub-sections go through a detail description of the rules defined in both external and internal loop.

3.5.1 External-loop rules

As explained above, the objective of the external loop is to ensure all the available $E_{sun,p}$ be stored in the battery pack once the driving phase is over. This can be obtained imposing SOC_f always be safely lower than 1. This constraint can be expressed as follows:

$$SOC_f=0.9-\frac{\Delta SOC_{max,d}}{2}-\Delta SOC_p \quad (41)$$

where $\Delta SOC_{max,d}$ is the maximum allowed battery variation during driving phase, here assumed equal to 0.1. According to Eq. (41), at the end of the day SOC will never overcome 0.9, thus allowing to perform satisfactory battery recharging by PV panels even in the case the car is not used over an entire day (i.e. driving phase h_{car} is 0 hours long).

Of course ΔSOC_pvaries with year season. Figure 50 shows the linear approximation, valid for the PV specifications listed in Table 2, of the relationship $\Delta SOC_p = f(S_f)$. S_f is a factor accounting for seasonal change of solar irradiation:

$$S_f=\frac{E_{sun,day}}{\overline{E}_{sun,day}} \quad (42)$$

where $E_{sun,day}$ and are, respectively, the actual and year-average energy yielded by the PV roof over one day. Figure 50 also shows the variation of desired SOC_f as function of S_f, computed through Eq. (41). It is worth noting that, for $S_f<0.75$, SOC_f is fixed equal to 0.75.

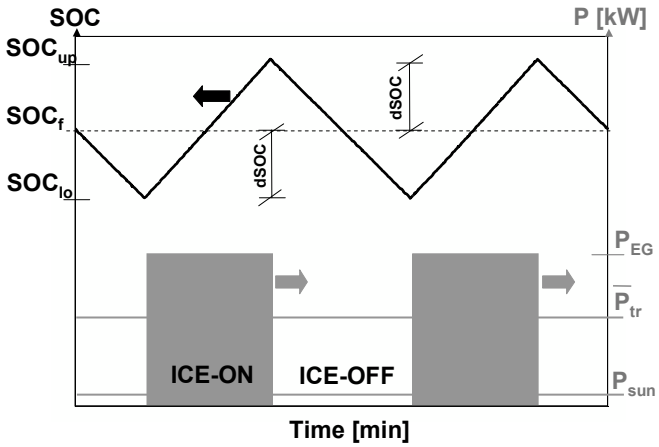

Figure 49 - Schematic representation of the rule-based control strategy for quasi-optimal energy management of a series HSV power train.

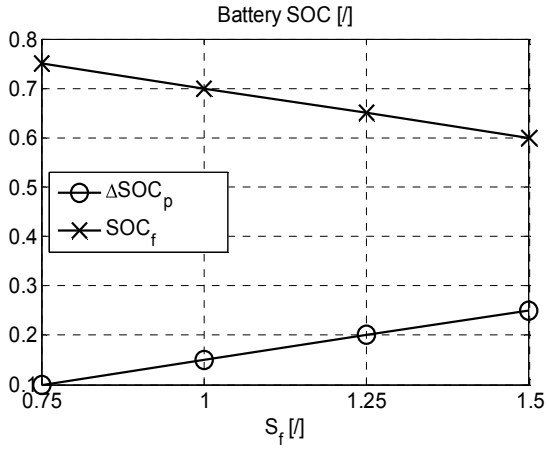

Figure 50 - Variation of optimal final SOC as function of daily solar radiation.

3.5.2 Internal-loop rules

Aim of this loop is to address at which power level the ICE-EG should work and how to manage its intermittent scheduling, alternating start and stop maneuvers.

The average power requested to the generator over an assigned time horizon can be determined as function of traction power, PV power and regenerative braking:

$$\bar{P}_{EG}=\bar{P}_{tr}-\bar{P}_{PV}-\bar{P}_{rb} \quad (43)$$

The terms on the right hand side of Eq. (43) can be either estimated as function of their previous values, by means of forecast techniques such as Recursive Neural Network [11], or derived from GPS data. It is worth noting that Eq. (43) holds valid in correspondence with the electric node EN shown on Figure 39.

In case of intermittent ICE-EG scheduling, the ICE-ON and ICE-OFF duration time, respectively indicated as $\Delta t_{ICE\text{-}ON}$ and $\Delta t_{ICE\text{-}OFF}$, are introduced. The time lag between two ICE-ON events can be defined as:

$$\Delta t_{cranck}=\Delta t_{ICE\text{-}ON}-\Delta t_{ICE\text{-}OFF} \quad (44)$$

The intermittent ratio can thus be introduced:

$$IR=\frac{\Delta t_{ICE\text{-}OFF}}{\Delta t_{ICE\text{-}ON}+\Delta t_{ICE\text{-}OFF}}=\frac{\Delta t_{ICE\text{-}OFF}}{\Delta t_{cranck}} \quad (45)$$

where the extreme cases IR = 0 and IR = 1 indicate, respectively, continuous ICE-ON and always ICE-OFF operation.

Then, a look-up table was developed to estimate optimal PEG as function of and S_f. Particularly, for assigned and S_f, PEG is determined by an optimization procedure expressed by the following equation:

$$\min m_f(X,\bar{P}_{tr}, S_f) \quad (46)$$

with initial condition:

$$SOC(0)=SOC_f \quad (47)$$

and subject to the constraints:

$$SOC(\Delta t_{crank})=SOC_f \quad (48)$$

$$SOC>SOC_f-\Delta SOC_{max,d} \quad (49)$$

In Eq. (46) the decision variables X include: PEG, IR and Δt_{crank}. A scalable η_{ICE} look-up table is used to map the relationship between ICE fuel consumption (m_f) and PEG. It is worth noting here that ICE fuel consumption is computed taking into account the thermal dynamics effects associated to intermittent ICE operation [40][41][42].

Figure 51 shows an example of solution to the problem expressed by Eqs. (46) - (49). The SOC trajectory initially decreases as the ICE-EG group is imposed to be initially off; then, due to ICE switching-on, SOC trend is inverted allowing satisfying the constraint expressed by Eq. (48). The difference between SOC_f and SOC_{min} (see Figure 51) is used to

evaluate the SOC excursion to be adopted in the Rule-Based control strategy depicted in Figure 49:

$$dSOC(\overline{P}_{tr},S_f)=\frac{SOC_f-SOC_{min}}{2} \quad (50)$$

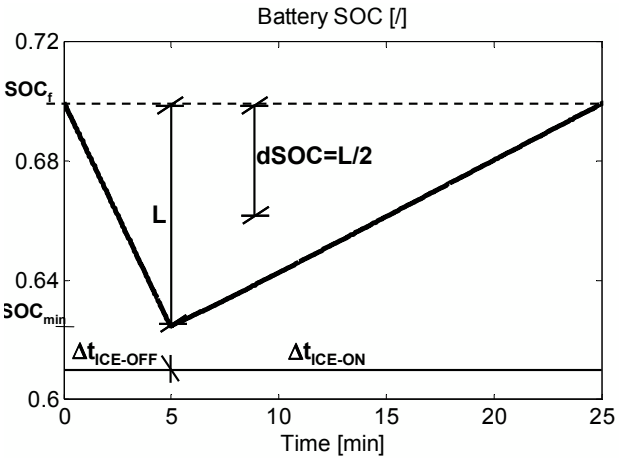

Figure 51 - Example of solution to the optimization problem expressed by Eqs. (46) - (49).

3.5.3 Implementation of rule-based strategy

The overall RB control architecture consists of three look-up tables:

$$SOC_f=f(S_f) \quad (51)$$

$$P_{EG} = f(\overline{P}_{tr}, S_f) \quad (52)$$

$$dSOC=(\overline{P}_{tr},S_f) \quad (53)$$

Figure 52 gives a schematic description of the rule-based control strategy implementation. Eq. (51) provides the desired SOC_f. Then, in the internal loop the average power at which the ICE-EG works is evaluated by Eq. (52). The ON-OFF rules for the ICE-EG will depend on the SOC excursion addressed by Eq. (53). The logic described in Figure 52 results in the control actions qualitatively shown on Figure 49.

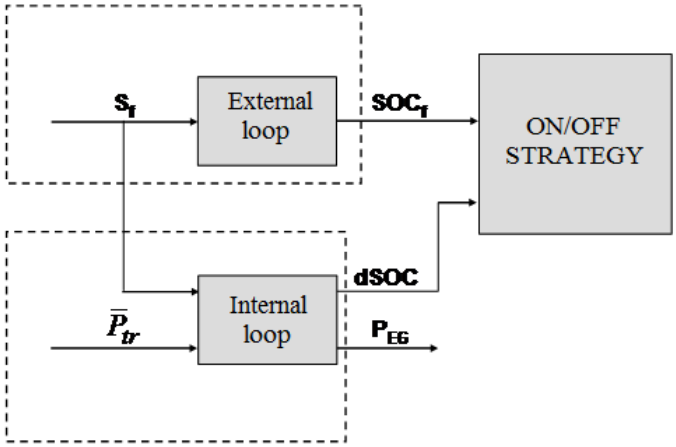

Figure 52 - Schematic description of external and internal loop actions within the RB control strategy.

It is worth discussing here about the determination of average traction power to be fed as input to Eqs. (52)(53). One possibility is to impose be constantly equal to the average power demand at wheels for common driving cycles, usually in the range 5 to 10 kW for passenger cars [40]. Nevertheless, better results are expected if is appropriately updated during the driving route, either by inferring it from available measurements (i.e. a-posteriori knowledge) or by means of forecasting techniques (i.e. a-priori knowledge). The above cases are deeply analyzed and discussed in the results section.

3.5.4 Optimization results

The performance of the RB strategy was tested via simulation of the HSV powertrain detailed in Table 1. It was assumed that the driving phase lasts for about 4700 s (i.e. h_{car} = 1.31 h) and consists of 4 ECE-EUDC modules. The simulations were run by a longitudinal dynamical vehicle model including also engine thermal dynamics effects, previously developed by the authors [20][42] in MATLAB® environment.

HSV specifications	
Nominal ICE power [kW]	46
Fuel	gas
Nominal EG power [kW]	43
Nominal EM power [kW]	90
Number of Lead-acid battery	27
Battery capacity	8
PV horizontal surface [m^2]	3
PV efficiency	0.1
Coefficient of drag (C_d)	0.3
Frontal area [m^2]	2.3
Weight [kg]	146
Scenario analysis assumptions	
$\overline{E}_{sun,day}$ at 30° Latitude and	559
Sun factor, S_f	1
h_{sun} [h]	10

Table 7 - HSV specifications and assumptions considered in the scenario analysis described in Table 9.

Prior to this numerical investigation, the look-up tables expressed by Eqs. (51)(52)(53)were developed. The following intervals were selected for the independent variables: $S_f \in [0 \div 1.5]$, $\overline{P}_{tr} \in [0 \div 11]$kW.

Afterwards, three simulation analyses were performed referring to the three scenarios outlined in Table 9. Particularly, in scenario 1 the $\overline{P}_{tr}$ value fed to Eqs. (52)(53) is never updated while in scenario 2 an a-posteriori based knowledge is adopted to update $\overline{P}_{tr}$ as function of past $P_{tr}(t)$ measurements. On the other hand, in scenario 3 the ideal case of perfect prediction of $\overline{P}_{tr}$ in the next t_h time horizon is assumed. Therefore, the last scenario allows individuating the best-case for the proposed rule-based control strategy for HSV energy management. In scenarios 2 and 3, several simulations were performed to analyze also the effect of time-horizon length on RB performance.

Scenario	$\overline{P}_{tr}$ formula	FE_{RB} [km/l]
1	Constant value: $\overline{P}_{tr} = \overline{P}_{ECE-EUDC}$	15.5
2	a-posteriori update: $\overline{P}_{tr}(t)\|_{t_i<t<t_i+t_h} = \frac{1}{t_h}\int_{t_i-t_h}^{t_i} P_{tr}(t)$	15.96
3	a-priori update: $\overline{P}_{tr}(t)\|_{t_i<t<t_i+t_h} = \frac{1}{t_h}\int_{t_i}^{t_i+t_h} P_{tr}(t)$	16.25

Table 8 - Analyzed scenarios. In the third column on the right hand side, i is an integer varying in the range $[0 \div t_{ECE-EUDC}/t_h]$.

Figure 53 shows the time trajectories of simulated P_{tr}, PEG and T_{eng} in correspondence with scenario 2 and 3 best cases.

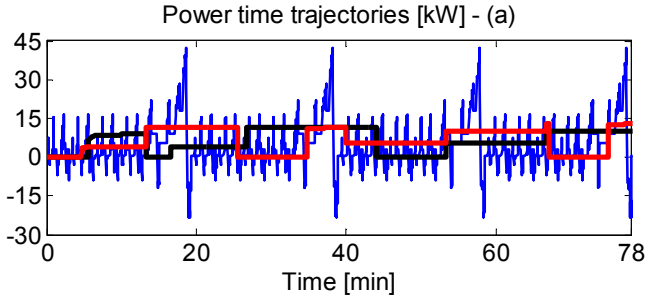

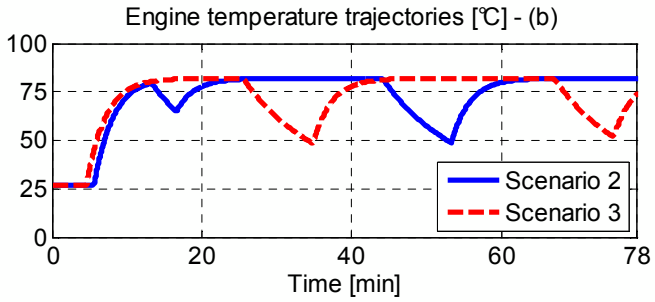

Figure 53 – (a) Simulated power trajectories. Blue line: Ptr; black line: scenario 2 PEG; red line: scenario 3 PEG. (b) Simulated engine temperature profiles.

The figure indicates that in scenario 3 the a-priori update allows increasing P_{EG} power in correspondence with higher traction power demand. Of course this is not the case of scenario 2, whose a-posteriori update causes more-significant SOC depletion when traction power demand increases, as shown on Figure 53 and Figure 54. This way the battery pack tends to be operated in high discharging resistance regions [47], thus explaining the expected lower fuel economy computed in scenario 3, as compared to scenario 2.

Nevertheless, the availability of past P_{tr} information allows well restoring battery charge level in the next time horizon. This aspect clarifies why scenario 2 performance are still acceptable, when compared to scenario 3, and even superior to a constant P_{tr} assumption (i.e. scenario 1, see Table 9).

In Figure 54 it emerges that during the parking phase the SOC increases over the initial value SOC_0. Such an extra battery charge ΔSOC_{ext} was accounted for in the fuel economy estimation by evaluating the equivalent fuel consumption, as follows:

$$m_{f,eq}=m_f-\frac{\Delta SOC_{est}\cdot C_B}{\bar{\eta}_{ICE-EG}\cdot H_i} \qquad (54)$$

where $\bar{\eta}_{ICE-EG}$ is the average efficiency estimated for the ICE-EG system over the ECE-EUDC cycle.

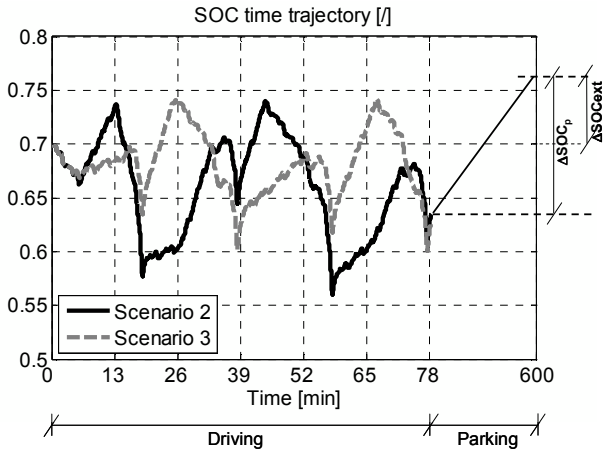

Figure 54 - Simulated SOC profiles.

Table 9 indicates that fuel economy achievable by means of the proposed RB control strategy reaches as up as 16.25 km/l. This corresponds with about 25 % fuel savings with respect to a conventional vehicle with same power to weight ratio as the simulated HSV (see Table 8). Moreover, the simulated HSV fuel consumptions are consistent with other numerical results presented in previous contributions with reference to other hybrid powertrains, such as Toyota Prius, and same driving cycle (i.e. about 17 km/l on ECE-EUDC) [48]. It is also worth noting here that further fuel savings are expected upon introduction of more advanced technologies, such as lithium batteries and new generation high-efficiency PV panels and/or PV films.

3.6 RB vs Genetic algorithms

In order to perform a comparative analysis of RB performance, the fuel economy yielded on output by the simulations is evaluated against a reference benchmark. Such benchmark corresponds with the genetic-algorithm-based optimization method that assumes the previous knowledge of the driving cycle. It is worth mentioning here that the GA method was adapted to the vehicle specifications listed in Table 7 and, more importantly, that the ICE-EG optimization degrees of freedom were

increased to further reduce fuel consumption. This way, a more robust comparative assessment of RB strategy performance was guaranteed.

The comparison of simulated GA and RB performance indicates how the latter gets significantly close to the former, resulting in fuel economy decrease of about 0.1 % on the ECE-EUDC cycle.

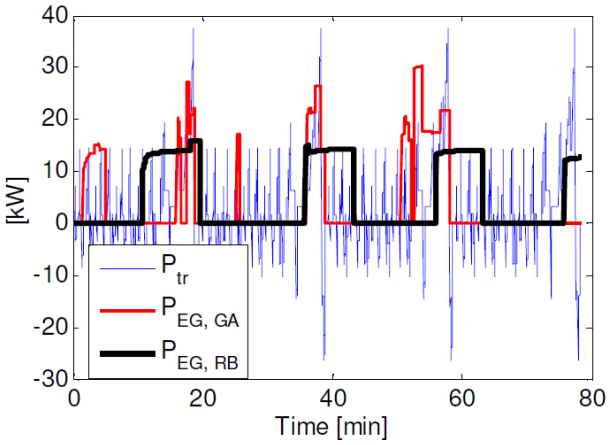

Figure 55 - Simulated power trajectories.

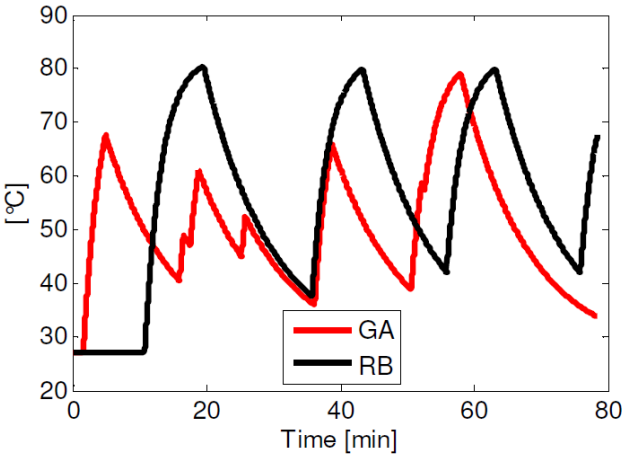

Figure 56 - Simulated engine temperature trajectories.

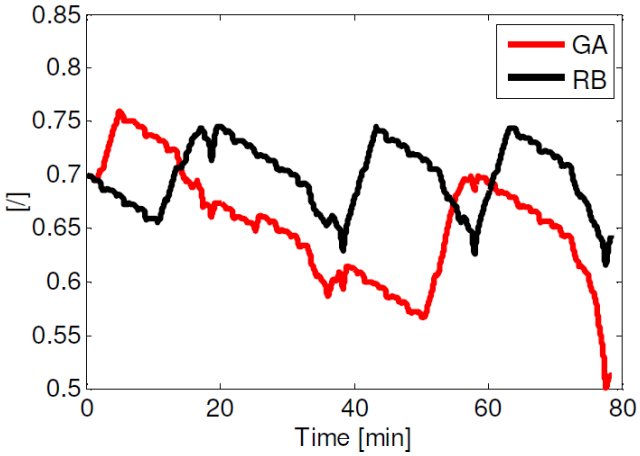

Figure 57 - Simulated battery SOC trajectories.

Figure 55 through Figure 57 compare the EG, engine temperature and SOC trajectory, simulated by means of the RB strategy, with those referring to the reference GA benchmark. It is worth noting that, in order to account for the different SOC that will be reached at the end of the day, HSV equivalent fuel consumption was computed as Eq. (54) [46].

Regarding the prediction time-horizon adopted in the RB simulations, it was found minimizing fuel consumption over the entire ECE-EUDC cycle. In order to analyze the dependence of t_h value on driving cycle characteristics, the procedure was repeated on the other driving cycles listed in Table 9. Figure 58 shows the variation of t_h as function of average traction power. Interestingly, t_h exhibits a linear trend with respect to $\overline{P}_{tr}$. The latter observation can be explained considering that higher $\overline{P}_{tr}$ values are usually associated to constant-speed highway driving, where $\overline{P}_{tr}$ standard deviation is very small. In such conditions, limited variation in future power demands is expected, thus allowing to extend prediction time horizon, as it emerges from Figure 58. It is worth mentioning here that h_{car} was set to 1.3 h for all the driving cycles listed in Table 9. Therefore, the simulated driving routes consist of a sequence of corresponding standard cycles.

Finally, Figure 59 illustrates the impact of solar irradiation on HSV fuel economies for all the analyzed driving cycles. The reference value

(i.e. corresponding to 100 % in Figure 59). As expected, increased irradiation level mainly improves urban-related fuel economies.

Driving cycle	P_{tr} [kW]	RB fuel economy [km/l]
CYC_1015_6PRIUS	1.51	26.32
FUDS	2.33	23.25
ECE-EUDC	2.99	22.45
FHDS	8.31	20.97
US06HWY	16.60	13.54

Table 9 - Selected driving cycles in the prediction time horizon analysis.

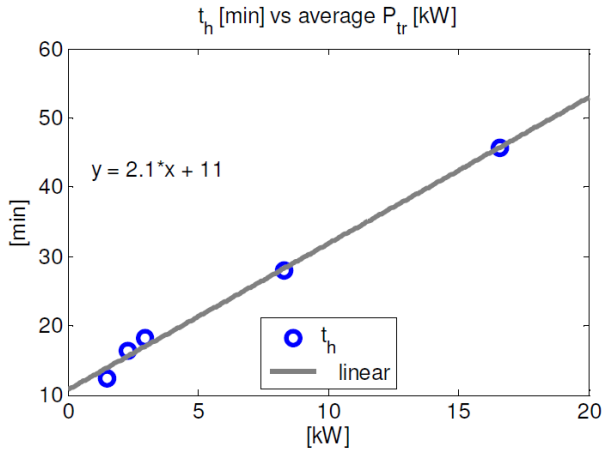

Figure 58 – Variation of prediction time horizon (t_h) as function of average traction power P_{tr}.

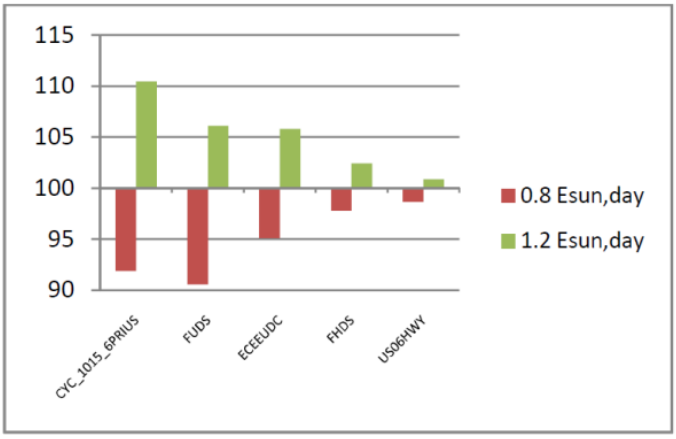

Figure 59 - Impact of daily PV energy contribution on HSV fuel economies. 100% corresponds with the average $E_{sun,\,day}$ value given in Table 3.

Figure 60 shows the variation of percent difference between simulated fuel economy (RB) and reference benchmark (GA), evaluated as:

$$\%\Delta FE=\frac{FE_{GA}-FE_{RB}}{FE_{GA}}\cdot 100 \qquad (55)$$

As stated, Eq. (55) indicates that the more %ΔFE is, the lower are RB performances with respect to the GA benchmark. The first general result emerging from Figure 60 is that RB strategy is always competitive with the reference benchmark, with per-cent differences bounded between 0.13 and 5% in the analyzed t_h interval.

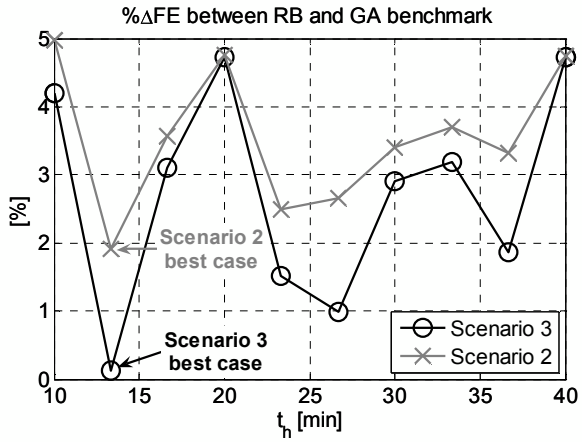

Figure 60 – Variation of % ΔFE as function of Ptr estimation time horizon.

More in detail, scenario 3 fuel economies are always superior to scenario 2, as expected. Particularly, the best-case achieved by the proposed RB strategy, occurring in correspondence with t_h = 13.3 min for scenario 3, is only 0.13 per cent worse than the reference benchmark. Moreover, the best fuel economy computed in scenario 2, which also occurs at t_h = 13.3 min, is slightly inferior (i.e. about 2 %) to the a-priori based RB. This comparative results fully demonstrate the high potential of the proposed RB strategy, even if based on an a-posteriori knowledge of average power requested at wheels.

CHAPTER 4

4 RB strategy applied to the HSV prototype

4.1 Introduction

In the previous chapters the comparison between Rule–Based strategy and the other two main strategies of optimization (Genetic Algorithm and Dynamic Programming) shows that the adoption the results obtained by the optimization through RB strategy are close to the ones obtained with the other two optimizations. So this strategy seems convenient to for two main reasons:

- he previous knowledge of the driving cycle is not always required;
- there are not strict mathematical operations.

To apply Rule-Based strategy Eqs. (51)-(53) show that it is necessary to compute the mean value of power traction and to establish the value of the sun factor Eq.(42).

$\overline{P}_{tr}$ can be evaluated with a backward or forward strategy, presented in Figure 61:

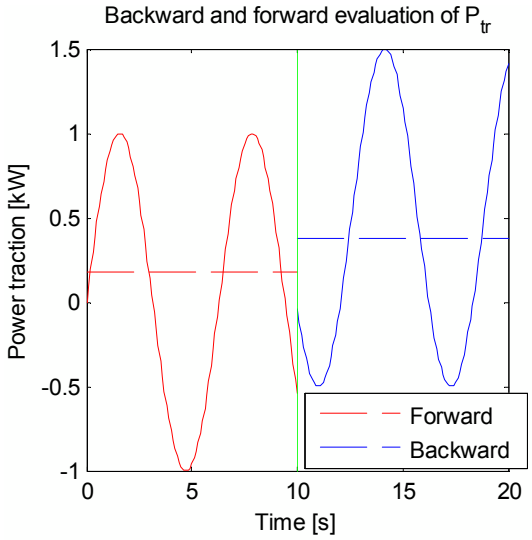

Figure 61 – Backward and Forward evaluation of P_{tr}.

- **Backward:** the mean value is evaluated on the previous knowledge of the data, taking the mean value of the power during a certain period;
- **Forward:** the mean value of the power is predicted.

First of all fuel consumption has been computed through a program developed in MATLAB, taking the driving cycle ECE-EUDC and the technical data of the hybrid solar vehicle presented in Table 7: it has been demonstrated that the values of fuel consumptions computed with backward and forward strategies of power traction are not very different.

Then, through experimental tests, the adoption of on-board solar energy prediction is presented and there is also the demonstration of the beneficial to select the best solution in terms of energy management.

Finally the program, previously developed in MATLAB for a generic HSV, has been adapted to the HSV prototype developed at University of Salerno considering also experimental driving cycles: the validation of Rule–Based strategy applied on the HSV prototype is presented through experimental tests.

After that it has been decided to adopt RB strategy for the on- board energy management of the HSV prototype through the adaptation of the MATLAB program into a program developed in LabVIEW.

4.2 Parametric analysis: P_{tr} backward and forward

Fuel consumption has been evaluated considering $\overline{P}_{tr}$ computed with a backward and forward strategy, making a comparison between the two techniques.

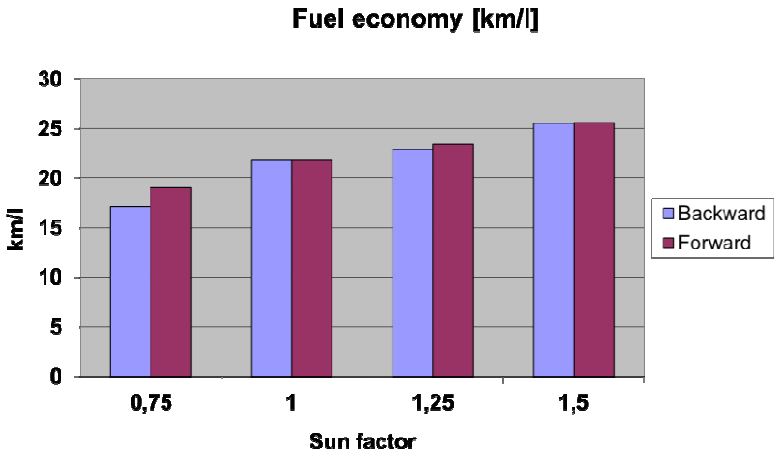

Figure 62 – Fuel economy evaluated with backward and forward strategies for different values of sun factor.

In Figure 62 fuel economy has been computed for the driving cycle ECE-EUDC, with C_r=0.1, and the time horizon t_h=1200 s. In this figure it is possible to see that the case more convenient is when is adopted with forward strategy, but at the same time this gain is not so considerable to justify the adoption of this strategy that is based on a previous prediction. This affirmation will be enhanced by the other experimental results presented in the rest of this work.

In Figure 63 the values of , computed with backward and forward strategy are presented, considering the time horizon t_h= 1200 s.

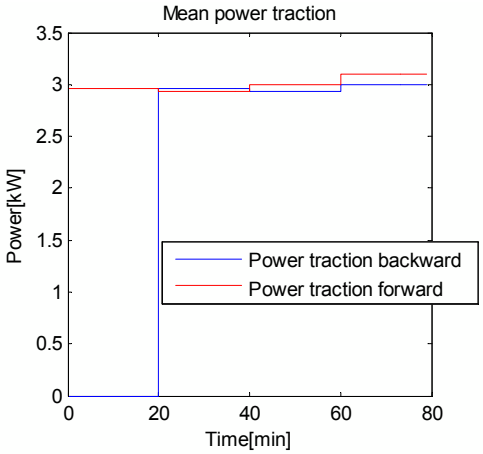

Figure 63 – Computation of the mean power traction with backward and forward strategy.

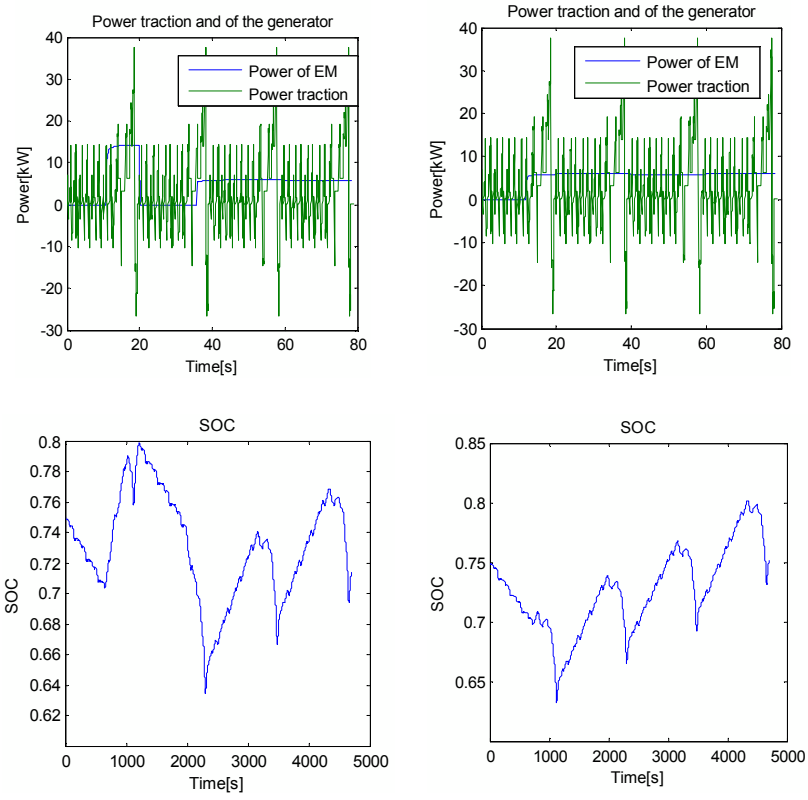

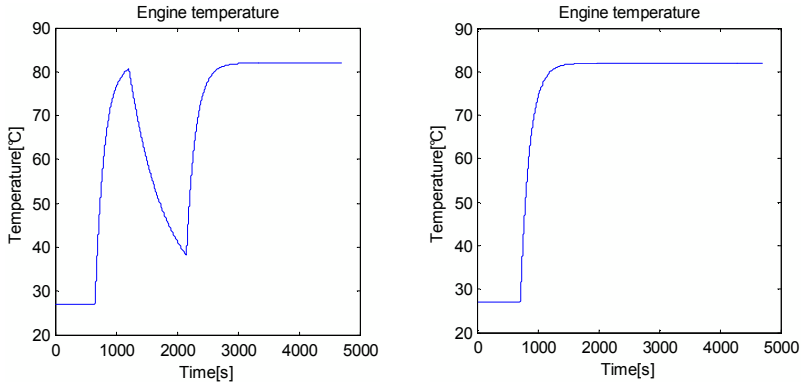

Figure 64 – Main variables obtained with the adoption of backward (on the left) and forward (on the right) strategies

Finally in Figure 64 the main variables of the driving cycle considering both strategies are presented: on the right there are the variable obtained with forward strategy and on the left the ones obtained with backward strategy.

4.3 SOC management in a HSV

In order to maximize the benefits of Hybrid Solar Vehicles, battery management should account for two conflicting requirements: at the end of driving the final state of charge (SOC) should be low enough to allow full storage of solar energy captured in the next parking phase, whereas the adoption of an unnecessary constantly-low value of final SOC would give additional energy losses and compromise battery lifetime. The adoption of on-board solar energy prediction can be therefore beneficial to select the best solution in terms of energy management. In order to assess the benefits achievable by using weather forecast, the effects of different strategies of selection of final SOC are studied by simulation over hourly solar data at different months, and the effects of forecast accuracy on fuel economy is analyzed.

	Scenario 1 η_{PV} **=0.13**	**Scenario 2** η_{PV} **=0.19**	**Scenario 3** η_{PV} **=0.25**

	Best parametric	Rule 1	Best parametric	Rule 1	Best parametric	Rule 1
[km/l] Jan	20,55	20,55	20,98	21,69	22,29	23,8
[km/l] Jul	26,04	26,59	32,81	33,25	42,5	43,21
Average SOC-Jan	0,62	0,72	0,53	0,73	0,45	0,74
Average SOC - Jul	0,66	0,74	0,61	0,7	0,58	0,69

Table 10 - Overall resume of the scenario analysis outcomes.

The simulations are carried out with a dynamic model of a HSV previously explained in paragraph 3.2.1, including a Rule-Based Energy Management Strategy (RBEMS).

Specifically to have this kind of management, the RB strategy has been modified so as to incorporate both perfect and real solar prediction to enhance battery management in driving phases. A solar calculator, based on the analysis of time series of solar radiation over about 30 years, has been used [www.nrel.gov/rredc/PVWATTS] to estimate the hourly solar energy achievable at different locations and months on a solar roof in horizontal position.

Some results have been obtained simulating a Hybrid Solar Vehicle, which characteristics are listed in Table 7, over hourly solar data in Los Angeles over ECE-EUDC cycles for three different efficiencies of solar panels. For each case, the best parametric case, obtained with a fixed choice of final SOC, is compared with the result obtained by the rule based approach, using solar energy forecast.

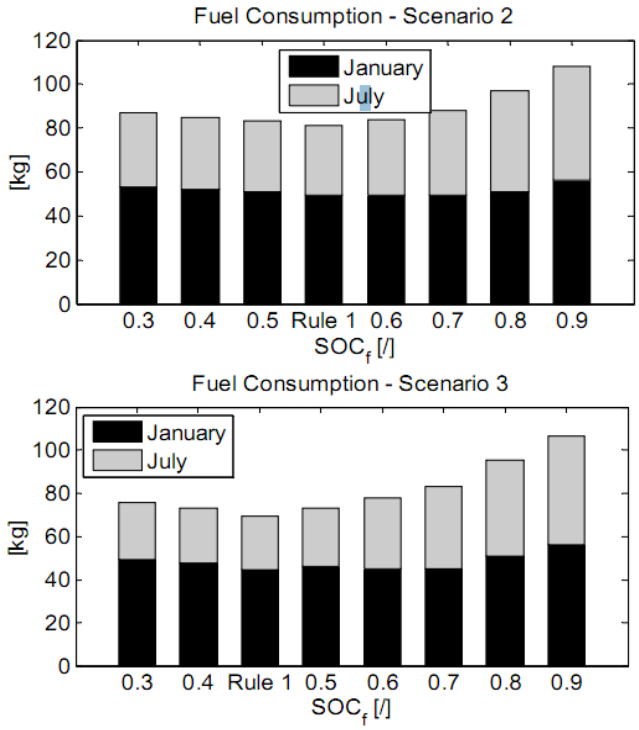

Figure 65 - Simulated Fuel Consumptions for Scenario 2 (η_{PV} =0.19) and 3 (η_{PV} =0.25).

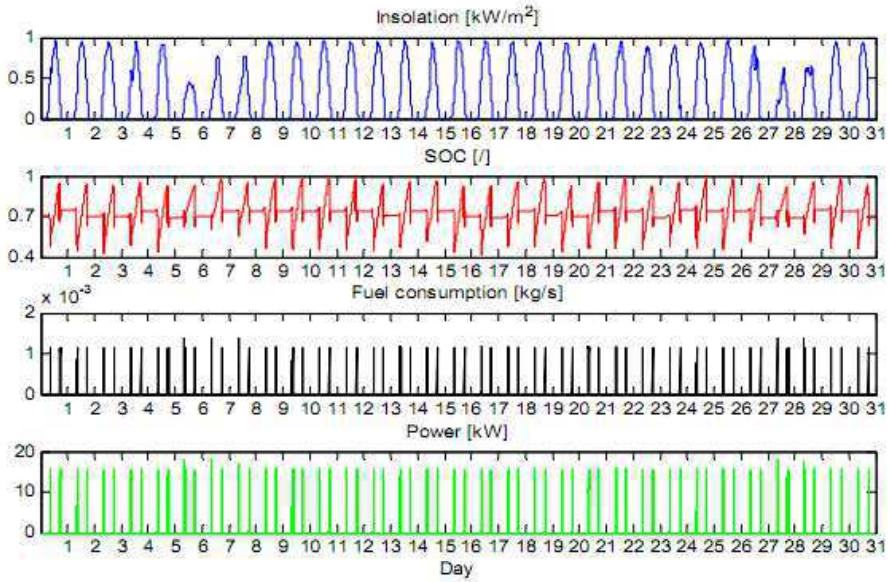

Figure 66 - Global simulation of July 1988. Scenario 2 optimal case with perfect solar power prediction.

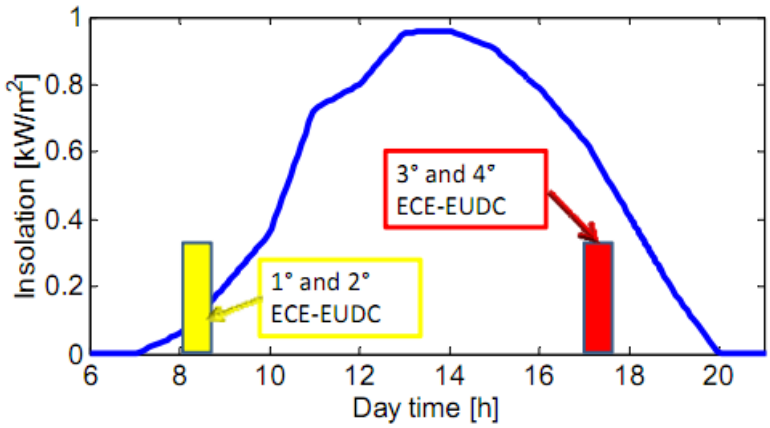

Figure 67 - Schematic representation of a generic daily simulation.

The results confirm that fuel consumption is significantly affected by the choice of final battery SOC, and that the lowest values are obtained by predicting the solar energy available during parking phase Figure 65. In this case, the occurrences of battery saturation are minimized Figure 66,

also avoiding unnecessary operation at low SOC values, where fuel economy is penalized.

4.3.1 Effects of forecast precision on vehicle management

The results presented in previous figures have been obtained by a perfect prediction of the solar energy that can be captured in next parking phase. Of course this prediction involves the estimation of both solar power and parking period, in terms of starting/ending time. It is therefore important to evaluate the sensitivity of the fuel consumption reduction to the precision in estimating the incoming solar energy. A series of simulations have been performed, introducing errors with respect to perfect prediction (the estimation of final SOC is performed with the perturbed data, while the simulation of fuel consumption utilizes the original data). The expected solar power data have been modified by introducing a Gaussian error, according the following formula:

$$P=P_{ref}+P_{ref,max}k\ RN \qquad (56)$$

The real power value P_{ref} is perturbed by adding a positive or negative term proportional to the maximum power during the day. RN indicates a random number from a normal distribution with zero mean and standard deviation one. The factor k has been varied between 0 and 0.4.

A comparison between the results obtained by perfect (k=0) and inaccurate (k=0.4) prediction is presented in Figure 68. It can be observed that, for perfect prediction, SOC values range usually from 0.5 to 0.9, while in case of inaccurate prediction they range in a wider interval, in some cases reaching saturation conditions (SOC=1).

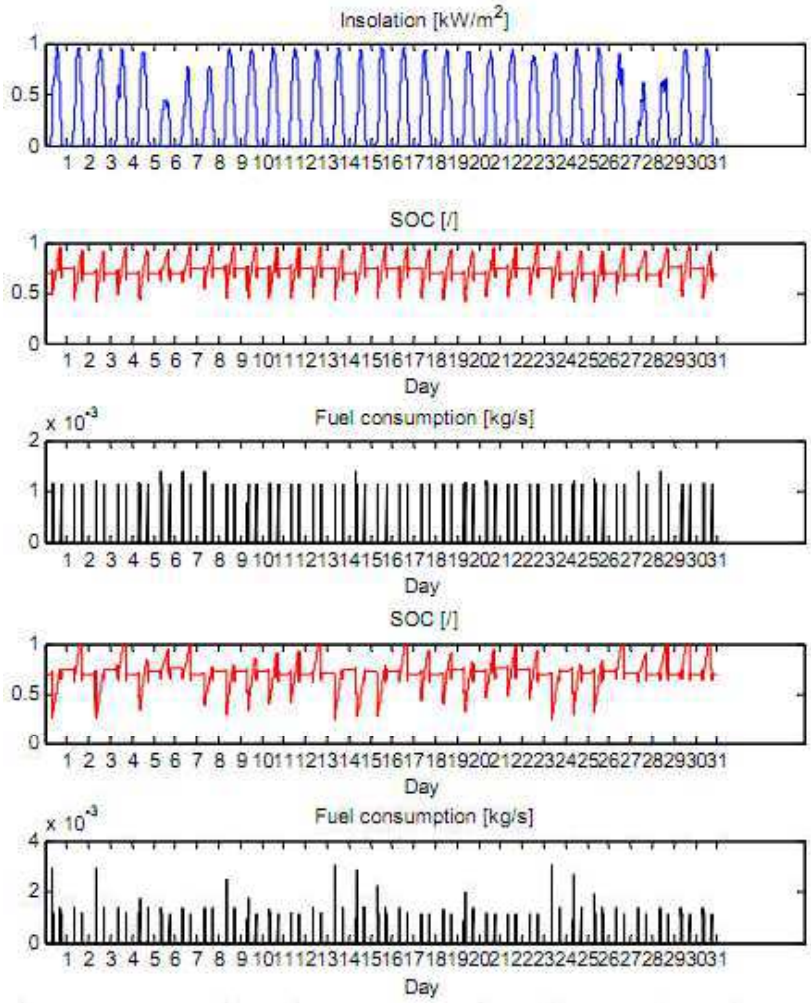

Figure 68 - Comparison between perfect (k=0, up) and non-perfect (k=0.4, bottom) prediction.

Consequently, fuel consumption values are quite regular in the former case, while some irregular peaks are present in case of inaccurate prediction. The results obtained by simulation analysis are summarized in next figures, in terms of fuel economy Figure 69 and percent degradation Figure 70 with respect to perfect prediction. In both cases, the best result obtained by parametric analysis, using a fixed value of final SOC, is also indicated (red line). It can be observed that, as expected, fuel economy

decreases when forecast error increases. Moreover, the spread of the results also increases significantly with forecast error. In particular, if forecast error is lower of about 0.15, the results obtained by use of solar power forecast are better than the best result obtained by a fixed value of SOC, while for higher errors there is not an apparent benefit in terms of fuel economy by using weather forecast.

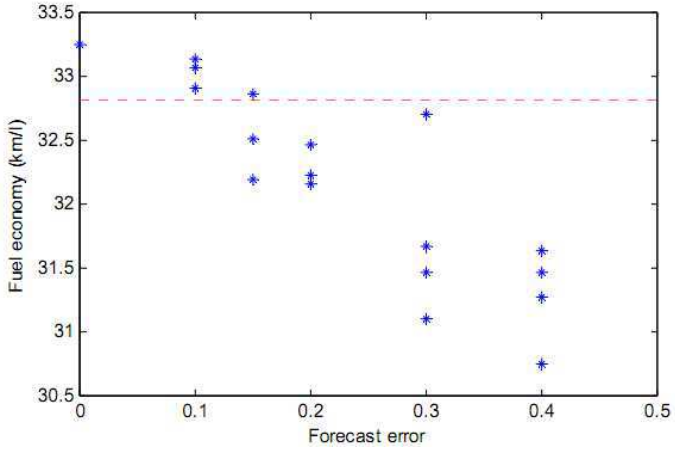

Figure 69 - Fuel economy vs forecast error (red line is the best parametric result).

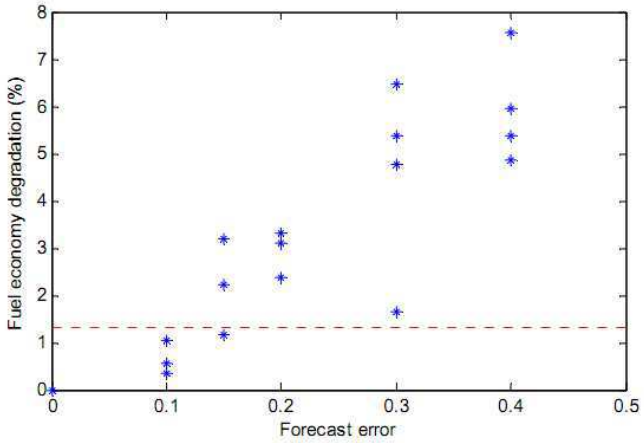

Figure 70 - Fuel economy percent degradation vs forecast error (red line is the best parametric result).

Anyway, it should be observed that the reference case considered (red line) represent the best result obtained by a parametric analysis, optimized for the months studied, and that the fuel economy values obtained by a non-optimized fixed value of final SOC would be lower.

4.4 Solar power forecast

The estimation of net incoming energy in next parking phase involves the estimation of both solar power and parking time. The estimation of the start of next parking phase could be accomplished by use of on-board navigator system, providing the expected end of the current driving cycle.

Considering the end of parking phase, this could be estimated starting from statistical data on the driver habits, also considering the influence of the day of the week. Alternatively, the driver could be asked to enter or confirm these data when he starts a new driving cycle.

In the following, the accuracy achievable in solar power forecast by using some on-line tools is analyzed. There are many websites that offer weather forecast, for different locations. Moreover, there are an increasing number of companies that offer forecasting for the energy sector, including solar power prediction, as for instance www.enfor.eu, claimed as "among the most accurate tools on the market for solar power forecasting today". Anyway, this tool is not currently available on-line. For this study, it has been selected www.wunderground.com, a service available on-line that allow obtaining forecasts for 5 days for a generic location. The site does not show the expected solar power, but instead provides the expected cloud cover, in percent, at various hours of the day (1, 4, 7, 10, 13, 17, 19, 23). This index can be correlated to solar power, according to some studies [4]. The forecast is based on interpolation from weather stations near to the given location.

A software tool to extract cloud cover estimation for a given location has been developed and implemented in MATLAB on a web server. In fig.4 an example of cloud cover forecast is shown, for the current day and for the three subsequent days.

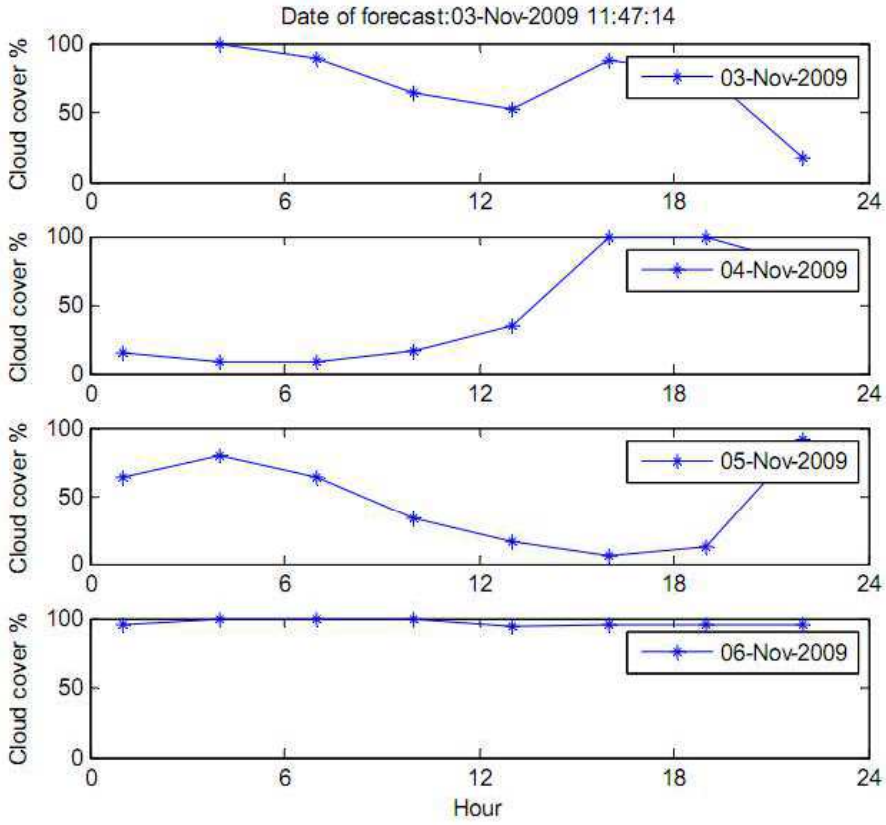

Figure 71 - Cloud cover forecast for Fisciano, Italy

In order to check the possibility to use such data for estimation, the global solar radiation on an horizontal plane in Fisciano has been measured by means of a pyranometer, in a period from March 21 to May 9, 2010. The data have been aggregated as hourly average. In parallel, cloud cover forecast data have been acquired on-line. For each day, the measured data E_m have been compared with theoretical radiation E_s, computed considering direct and diffused components in a sunny day, and the ratio f between them has been computed:

$$f=\frac{E_s}{E_m} \qquad (57)$$

The main variables defining sun position (declination δ, hour angle h, sun height α, azimuth Φ_s) are computed by the relationships expressed in Chapter 1, as a function of Latitude L and longitude φ:

The global solar radiation can be computed is composed by the direct and the diffuse solar radiation: even in this case all the variables necessary to compute the global solar radiation will be better explained in the rest of this work.

Next pictures show a comparison between measured and computed values, and the cloud cover data for the same day (this value has been acquired at the end of the day). In the first case, with an average cloud cover of 12% Figure 72, the daily measured radiation is about 94% of the theoretical one, while in the second case Figure 73 the measured radiation is significantly lower (about 50%), consistently with a higher value of cloud cover (34.5 %).

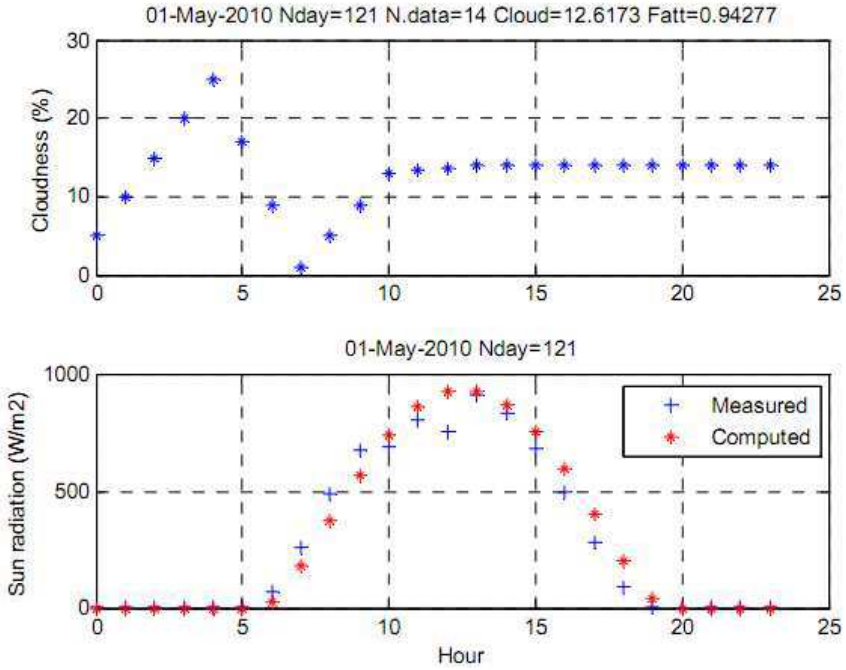

Figure 72 - Measured and computed solar radiation, and estimated cloud cover (May 1st, 2010).

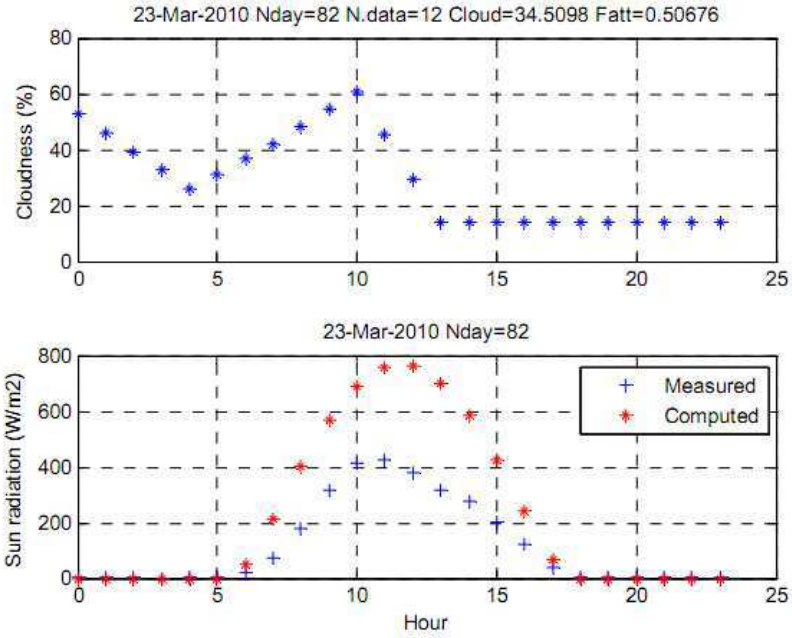

Figure 73 - Measured and computed solar radiation, and estimated cloud cover (March 23rd, 2010).

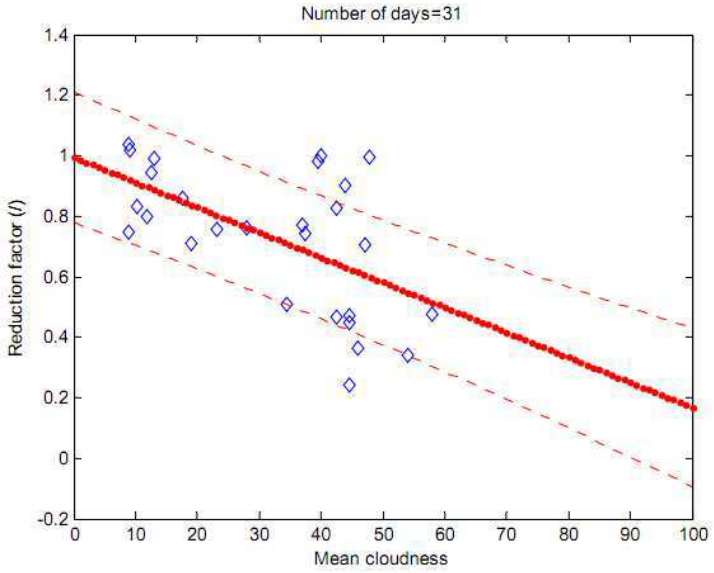

Figure 74 - Reduction in daily solar energy vs cloud cover.

Anyway, the study of the whole data has shown that there is not a significant correlation between the hourly cloud cover and the difference between measured and theoretical data, with a correlation coefficient almost equal to zero. This poor correlation may depend on several factors, as the need to interpolate from different and possibly distant weather stations.

Instead, better results can be found by aggregating the data on a daily base. In Figure 74, the ratio f (1) is plotted versus the daily mean cloud cover, while the red line represents the first-order regression curve. Figure 75, the error between the measured value of f and the value estimated by the regression line is plotted, versus mean daily cloud cover.

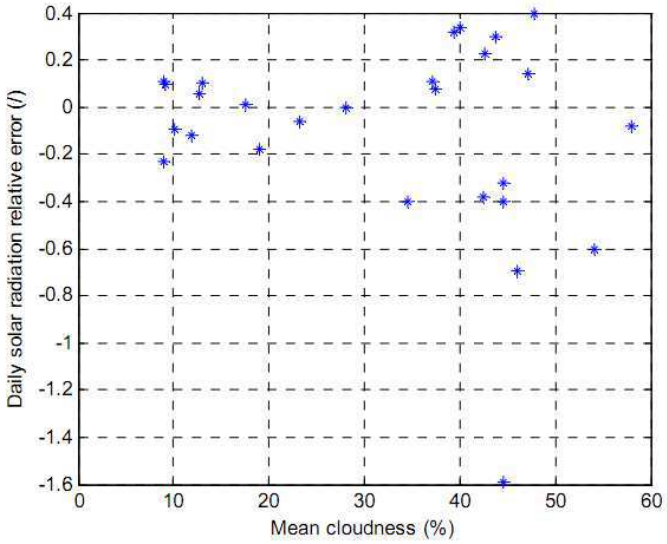

Figure 75 - Distribution of forecast error on daily base.

By analyzing the data corresponding to 31 days, and considering only days with at least 10 hourly measured data per day, it emerges that, when could cover is less than 30%, the relative error between the measured value and the value estimated by regression line is lower that 20%, while with higher values of cloud cover (30-60%) the uncertainty is larger, usually within 40%, apart some singular cases. It can be observed that with cloud cover between 40% and 50% there are roughly two clusters of data: one under the red line, corresponding to days with a reduced radiation, and one up the red line, corresponding to days with little reduction in radiation with respect to sunny day. At higher cloud cover (50-60%) the trend appears more regular. It could be considered that, when cloud cover is limited, the probability that clouds could obstruct sun rays is lower, and the data are more scattered, while the randomness is lower at low and high cloud cover values. [48]

Anyway, these conclusions should be confirmed by the analysis of a longer series of data, spanning over different periods of the year and, of course, extended to different locations.

However, it should be remarked that the factor k used in equation (56) does not coincide with the relative error plotted in Figure 75, although they are of course correlated.

4.5 Main variables adopted in experimental tests

To have also experimental demonstrations of the efficiency of RB strategy to each HSVs, as it has previously said this strategy has been tested on the prototype of HSV described in paragraph 2.4.2.1, considering an experimental driving cycle, realized in the campus of the University of Salerno.

Each scenario has been analyzed on a 860 s long driving cycle and its speed and the power of the electric motor are shown in Figure 76 and in Figure 77.

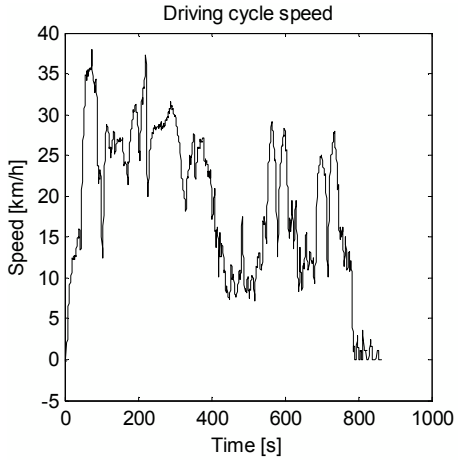

Figure 76 – Speed of the experimental driving cycle

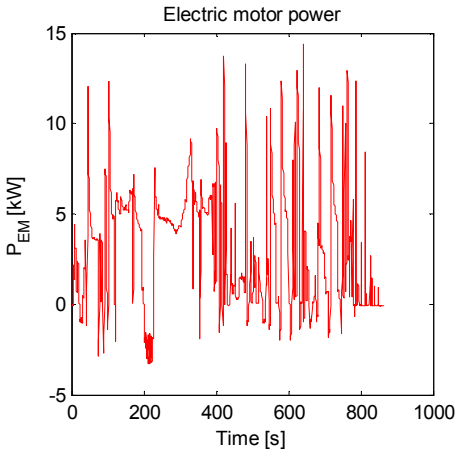

Figure 77 – Power of the EM in the experimental driving cycle.

The values of the prototype considered are different from the ones presented in Table 7 but refers to the HSV prototype developed at University of Salerno and they are presented in Table 11.

HSV specifications	
Nominal ICE-EG power	6
Fuel	gas
EM peak power [kW]	15
Number of Lead-acid battery modules	16
Battery capacity [kWh]	17
PV horizontal surface [m^2]	1.44
PV efficiency	0.10
Weight [kg]	190

Table 11 – HSV technical specifications.

A yearly average value of 4.31 [kWh/m^2] for the daily solar energy $\overline{E}_{sun,day}$ irradiating on an horizontal surface has been assumed.

The impact of solar energy contribution also has been investigated by varying the sun factor S_f in the range (0÷1.5), where S_f=1 corresponds to

the average daily energy that impacts on an horizontal surface at the University of Salerno region (4.31 [kWh/m^2]).

4.6 Rule-based control strategy applied to an HSV prototype

Rule – based control strategy has been also validated experimentally.

Previously, as it has been explained in paragraph 3.6, it has been validated against the optimization with Genetic Algorithm, and it has been preferred to Dynamic Programming because it is not necessary a previous knowledge of the driving cycle. All the main variables are presented in the paragraph 4.3.

The experimental validation has been realized comparing fuel economy obtained in three different scenarios:

1. RB strategy: PEG and dSOC are obtained by Eqs. (52)(53);
2. Parametric analysis with dSOC obtained by Eq. (53) and PEG variable in the range (0.25÷0.75) times the nominal EG power (i.e. 6 kW, as shown on Table 11).
3. Parametric analysis with dSOC variable in the range (0.01÷0.02) and PEG obtained by Eq. (52).

In scenario 1 (RB strategy fully active) fuel economies were simulated assuming both a-priori and a-posteriori knowledge of average power to be supplied by the series power train to the electric motor EM to meet driving cycle demands. As expected (see Figure 78), fuel economies with backward strategy are lower than the ones obtained with forward strategy.

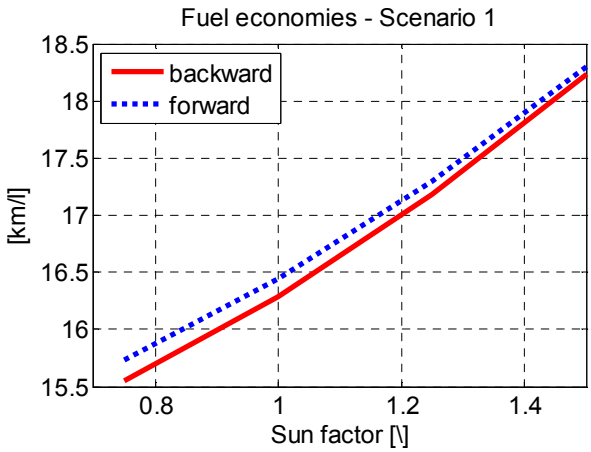

Figure 78 - Fuel economy with RB strategy

In Figure 79 and Figure 80 fuel economy was computed considering scenario 2 and scenario 3 assumptions, respectively.

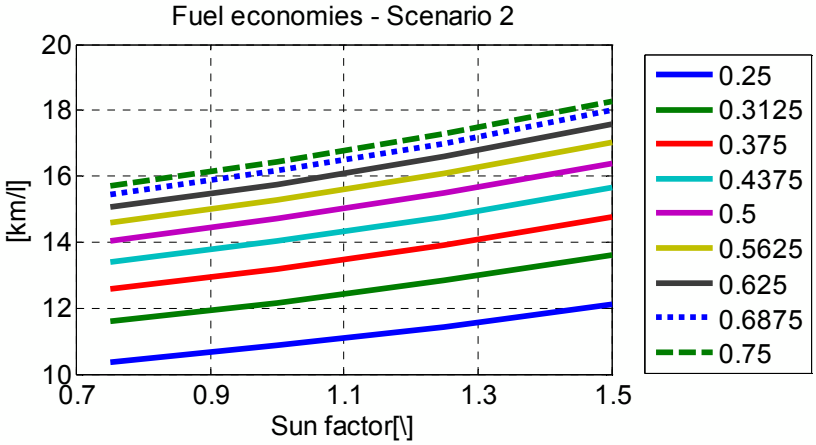

Figure 79 – Fuel economy for scenario 2

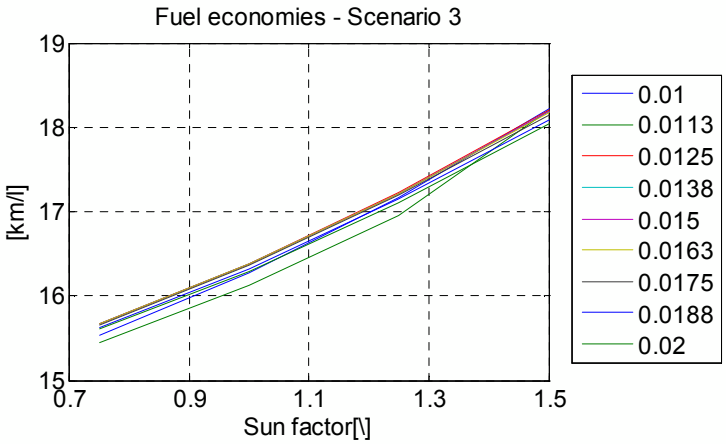

Figure 80 - Fuel economy for scenario 3

To check the convenience in adopting the RB strategy, the fuel consumption obtained in scenario 1 and the most convenient cases in scenario 2 and 3 have been compared (Figure 81). It emerges that even though RB does not achieve the highest fuel economy, its values always fall close to the best ones computed in scenario 2 and scenario 3. By considering that both in scenario 2 and scenario 3 several computations were needed to address the most convenient intermittent strategy for the internal combustion engine, it is possible to conclude that on-board implementation of the proposed heuristic strategy performs near to the optimal conditions. This result is consistent with previous analyses, where RB strategy was validated against the results of an off-line optimization achieved via Genetic Algorithms.[49]

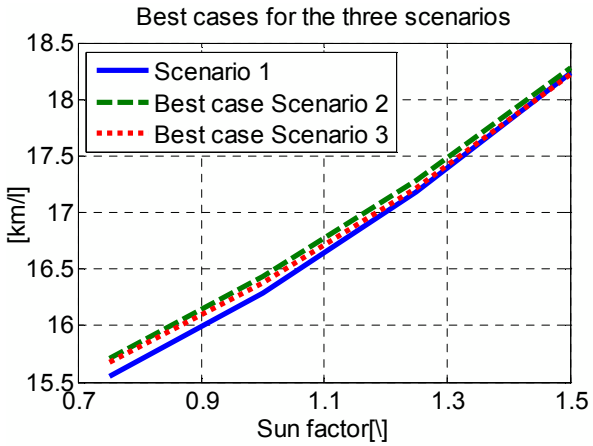

Figure 81 – Fuel economies in the three different scenarios

4.7 Going to on-board implementation of RB strategy

After proving its suitability for real-time energy management of HSVs, the RB strategy was then implemented on-board into a National Instrument compact Rio (NI cRIO®) platform, connected to a number of analog and digital input/output (I/O) ports. Main analog inputs include current, voltage, temperature, speed, angular speed, solar irradiation, torque and pedal position measurements. The digital outputs are mainly applied to electrical switches aimed at effectively performing the control actions addressed by the RB strategy, as shown on the flow diagram plotted in Figure 82.

The main inputs for the on-board RB strategy are:

- S_f: sun factor, depending on which the value of SOC_f is determined, see Eq. (51). S_f can be computed on-board as function of sun irradiation measured by a pyranometer.
- P_{EM}: electric motor power [kW], affecting equations (52) and (53).

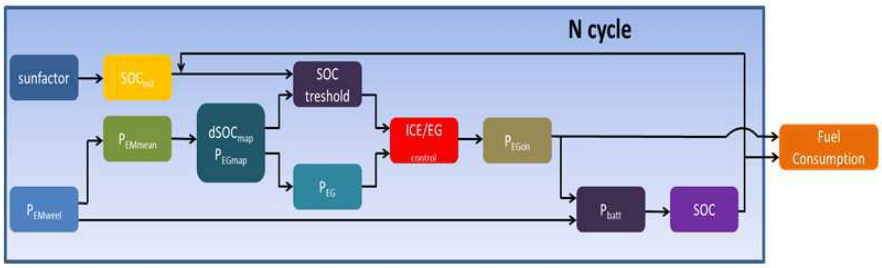

Figure 82 – Flow diagram of the RB strategy implemented into the NI-cRIO platform

A backward strategy is applied online to update every t_h seconds the average power requested by the EM to power the wheels ($\overline{P}_{EM}$). Then, according to $\overline{P}_{EM}$, the upper and lower SOC thresholds depending on which ICE intermittency is managed are evaluated. In order to estimate on-line the current value of battery state of charge as function of measured battery power, a battery model utilized in MATLAB® was transferred into LabVIEW environment.[49]

4.8 Experimental test on – board of the HSV prototype

The on-board implementation of the RB strategy was tested by running the HSV prototype along the driving route shown on **Errore. L'origine riferimento non è stata trovata.**-speed plot. During the test, a time horizon t_h =41.7s was imposed to suitably update average EM power. **Errore. L'origine riferimento non è stata trovata.** also shows the following measurements:

a) SOC and its thresholds;
b) Speed of the hybrid solar vehicle;
c) Power of electric generator;
d) Traction power, computed starting from the torque measured with a torquemeter;
e) Electric motor power;
f) Mean power of electric motor.

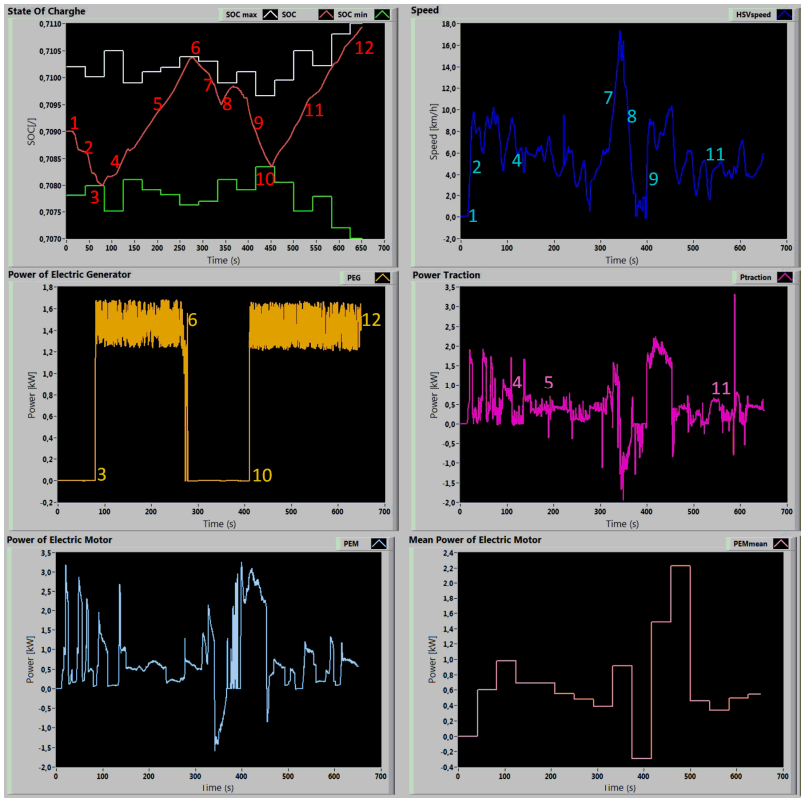

Figure 83 – Plots of main acquired variables during the on-board test of RB strategy.

In order to discuss the real operation of RB strategy, the values of SOC, speed, generator power and traction power are analyzed by referring to each section numbered in Figure 83.

1. In this section HSV's speed and power traction are zero, so there is no variation of SOC.
2. There is a strong SOC decrease due to a rapid acceleration from 0 to 10 km/h.
3. The value of SOC decreases until the value of SOC_{min} (point 3), as imposed by the RB strategy.
4. Despite the ICE is on there are two little battery discharges due to two strong accelerations.

5. There is a linear increase of SOC, as a consequence of the almost constant value of traction power.
6. The value of SOC grows till the SOC_{max} (point 6) value imposed by the RB strategy.
7. There is a rapid SOC decrease due to the high acceleration.
8. The ICE is off but there is a brief recharge. This happens because there is a strong braking (regenerative braking) as it is possible to see in the speed plot.
9. The value of SOC decreases again with a strong gradient due to high acceleration.
10. The value of SOC decreases until another value of SOC_{min} (point 10) that is imposed by the RB strategy.
11. The speed is almost low and constant, so the recharge of the battery is slow and linear.
12. It is clear, from the trend of SOC and its thresholds, that after a few seconds before the end of the cycle, the ICE shuts down. In fact after a few seconds the value of SOC reaches the value of SOC_{max} that is imposed by RB strategy.

Obviously the trends of SOC's thresholds depends on f) measurement.

It is worth mentioning that at the current stage it is not possible to fully apply the rule expressed by Eq. (52) on-board, due to the features of the battery charger through which ICE-EG and battery are interfaced that limits the maximum charging power to about 2 kW. This limitation will be overcome for future studies.[49]

CHAPTER 5

5 The mobile solar roof prototype

5.1 Introduction

In this chapter a moving solar roof for an Hybrid Solar Vehicle is presented.

With an optimal orientation of the roof, that means when the angle of incidence between the normal to the roof and the sun ray tends to zero, there is a considerable gain of energy.

The mobile solar roof has been realized as a parallel robot with three degrees of freedom. A mathematical model has been developed in MATLAB, the design has been realized through the software 3D SolidWorks, the control system had been realized at the beginning with a PLC [50], then with a webcam placed in the middle of the mobile roof and the control has been done with a program realized in LabVIEW.

The model of the proposed roof has been developed and validated over experimental data obtained by a small scale real prototype.

The effects of roof design variables have been analyzed, and the benefits in terms of net available energy assessed by simulation over hourly solar data at various months and latitudes.

The economic feasibility of this project but especially the energetic gain has been evaluated: this model has been designed to be mobile only during parking phases for two main reasons:

- The HSV analyzed must be used only for a urban use, so the driving phase lasts only 1-2 hours and the largest part of the day is a parking phase;
- If the solar roof is mobile also during the driving phase some aerodynamic losses and instability could happen.

The structure of a model based control to achieve the optimal orientation of the solar roof is also presented.

5.2 Tracking roof: fixed vs. mobile applications

There are some specific aspects that make the study of a moving roof on a car, even if only when parked, different from a fixed plant.

In fixed plant a solar tracker, briefly mentioned in paragraph 1.5.1.3, is a generic term used to describe devices that orient various payloads toward the sun. Payloads can be photovoltaic panels, reflectors, lenses or other optical devices.

In flat-panel photovoltaic (PV) applications trackers are used to minimize the angle of incidence θ between the incoming light and a photovoltaic panel. This increases the amount of energy produced from a fixed amount of installed power generating capacity. In standard photovoltaic applications, it is estimated that trackers are used in at least 85% of commercial installations greater than 1MW from 2009 to 2012.

5.2.1 Advantages of a tracking system referred to a fixed one.

Some data has been computed, based on 1961-1990 National Solar Radiation Data Base (NSRDB), considering real weather conditions, from a solar on-line calculator, named PVWATTS.

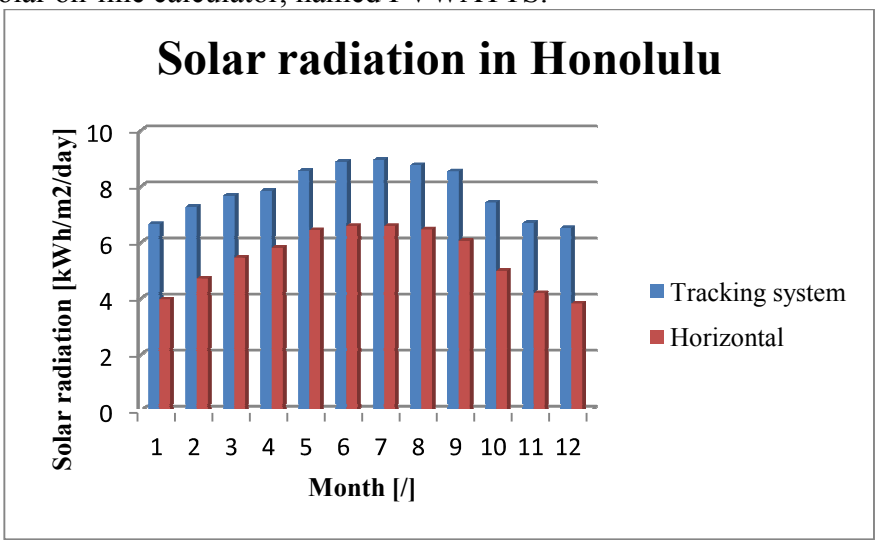

Figure 84 – Difference for the solar radiation in a tracking system and in an horizontal fixed one.

The data presented in Figure 84 refer to the solar radiation in Honolulu, in one day of each month for 1 m^2. In this figure is possible to see that each month, especially in winter the tracking system has a considerable gain of energy compared to a fixed horizontal system.

A common idea is that a solar panel could be useful in places with a little latitude, near the equator, so in sunny places. But trough experimental data next graph has been obtained.

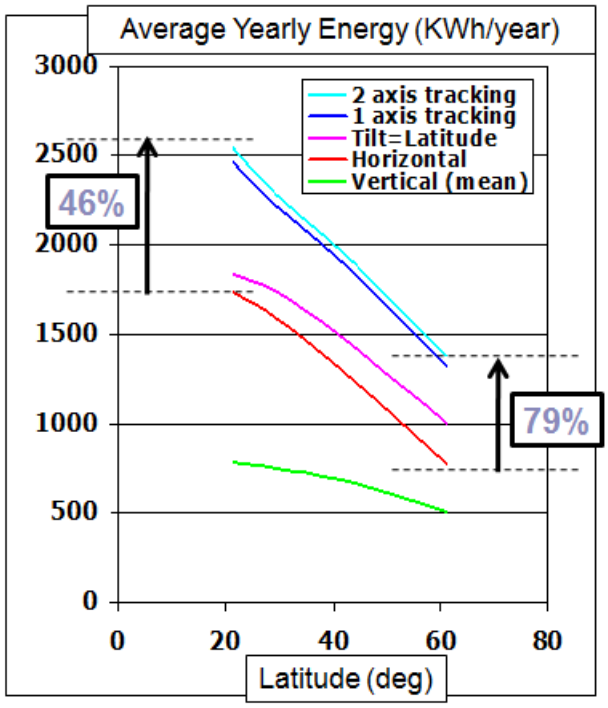

Figure 85 – Annual solar irradiation at different latitudes.

In Figure 85 the biggest gain of solar energy is at high latitude: the solar irradiance captured by a tracking system on 2 axes, a tracking system on 1 axis, a fixed system with the tilt angle like the latitude of the place and a fixed horizontal system. If it is necessary to have a fixed system, it is convenient that the tilt angle is like the latitude of the place considered.

So it is possible to say that a tracking system is always convenient in terms of gain of solar irradiance respect fixed system, in particular at high latitude.

5.2.2 Tracking system for mobile or fixed applications

Obviously there is a big difference if a tracking system is designed for mobile or fixed applications. Until now it is possible to see these tracking systems only in fixed applications, like on the roof of buildings or on open lands. The tracking system applied on cars has been considered for mobile applications. The main differences are:

- car orientation during parking is not fixed;
- solar exposure could be worse than in fixed plant;
- actuation must be faster than in a fixed plant;
- parking time may be not known;
- aerodynamic losses and additional weight should be minimized;
- perfect orientation could not be achieved in all conditions due to possible kinematic constraints.

Some of these points have been considered in the planning stage and they would be shown in the rest of this chapter.

5.3 When to move a solar roof in car applications

The possibility to store energy while the vehicle is parked is required for a solar roof panel to be able to convert a significant amount of energy. The amount of energy stored and finally used depends on various system parameters, for example the accumulator capacity or the efficiency of the solar roof panel. It also strongly depends on the driver's mobility behavior [52]: due to the setup described above the reduction of fuel consumption correlates with the electrical energy saved. This amount of saved energy depends on the electric power consumption and on the trip duration. The amount of converted solar energy that is available to support the vehicle electrical system depends on the time of day when the trips take place and on the parking duration between two trips. For instance, if the vehicle is parked outside between two trips longer than required to charge the accumulator the solar radiation during the remaining parking period will have no significant contribution to the vehicle's power supply; it might compensate the self-discharging effect of the battery. This effect will not be discussed in this paper. The main

influencing factors on the fuel reduction potential can be summarized as follows:

- driver's mobility behavior;
- ambient conditions (solar irradiance and ambient temperature);
- system parameters (accumulator capacity and solar module power).

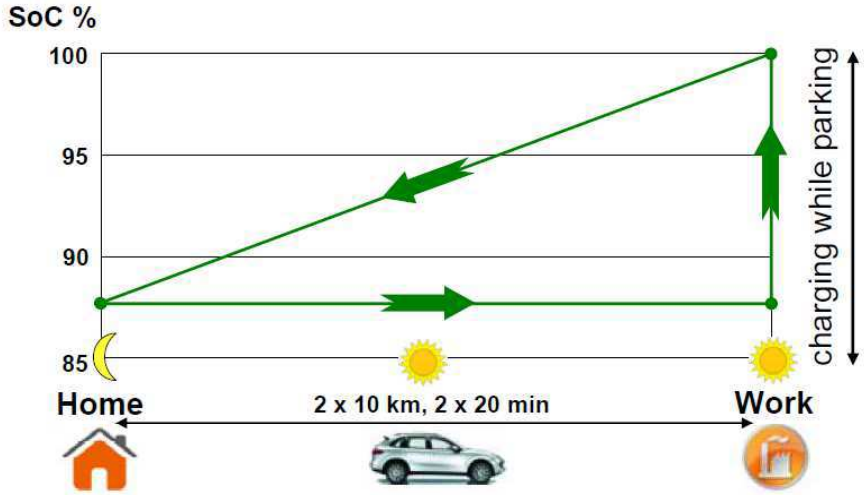

Figure 86 - Use case depicting the potential to use the solar roof module in order to reduce the load on the alternator, thus reducing fuel consumption [52].

For all these reasons it is possible to conclude that a moving solar roof, applied at cars, is suggested to use only during parking phases, because:

1. the use of this tracking roof during driving would result in car instability, aerodynamic losses, and excessive energy losses for orienting the panel, if car orientation is rapidly varying.
2. hybrid solar cars maximize their benefits when car is used no more than 1-2 hours per day, as it happens for a large number of users. Therefore, most of the solar energy is taken during parking.

The case 2 is justified by some recent studies of the UK government stated that:

- about 71% of UK users reaches their office by car;

- 46% of them have trips shorter than 20 min mostly with only one person on board.

5.4 Parallel robots

Parallel robots are articulated robots that use similar mechanisms for the movement of either the robot on its base, or one or more manipulator arms. Their 'parallel' distinction, as opposed to a serial manipulator, is that the end element (or 'hand') of this linkage (or 'arm') is connected to its base by a number of (usually three or six) separate and independent linkages working in parallel. 'Parallel' is used here in the topological sense, rather than the geometrical; these linkages act together, but it is not implied that they are aligned as parallel lines.

Parallel robots take an alternate approach. Each chain is usually short, simple and can thus be rigid against unwanted movement (compared to the serial arm). Errors in one chain's positioning are averaged in conjunction with the others, rather than being cumulative. Each actuator must still move within its own degree of freedom, as for a serial robot; however in the parallel robot the off-axis flexibility of a joint is also constrained by the effect of the other chains. It is this closed-loop stiffness that makes the overall parallel manipulator stiff relative to its components, unlike the serial chain that becomes progressively less rigid with more components.

This mutual stiffening also permits simple construction: Stewart platform hexapods chains use prismatic joint linear actuators between any-axis universal ball joints. The ball joints are passive: simply free to move, without actuators or brakes; their position is constrained solely by the other chains. Delta robots have base-mounted rotary actuators that move a light, stiff, parallelogram arm. The effector is mounted between the tips of three of these arms and again, it may be mounted with simple ball-joints. Static representation of a parallel robot is often akin to that of a pin-jointed truss: the links and their actuators feel only tension or compression, without any bending or torque, which again reduces the effects of any flexibility to off-axis forces.

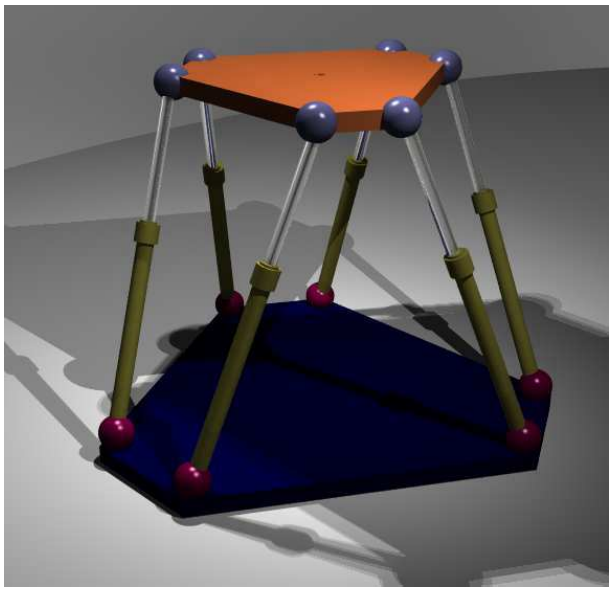

Figure 87 – A parallel robot: Stewart platform

A further advantage of the parallel manipulator is that the heavy actuators may often be centrally mounted on a single base platform, the movement of the arm taking place through struts and joints alone. This reduction in mass along the arm permits a lighter arm construction, thus lighter actuators and faster movements. This centralization of mass also reduces the robot's overall moment of inertia, which may be an advantage for a mobile or walking robot.

All these features result in manipulators with a wide range of motion capability. As their speed of action is often constrained by their rigidity rather than sheer power, they can be fast-acting, in comparison to serial manipulators.

Their major drawback is their limited workspace, because the legs can collide and, in addition (for the hexapod) each leg has five passive joints that each has their own mechanical limits. Another drawback of parallel robots is that they lose stiffness in singular positions completely (The robot gains finite or infinite degrees of freedom which are uncontrollable; it becomes shaky or mobile). This means that the Jacobian matrix, which is the mapping from joint space to Euclidian space, becomes singular (the rank decreases from six).[53]

5.4.1 Degrees of freedom

The number of degrees of freedom Dof, N_d, is computed with Grübler formula; this formula could be used only for rail joints:

$$N_d=\lambda(l-j-1)+\sum_{i=1}^{j} d_i \quad (58)$$

λ: factor of mobility in 2D level is 3, in 3D level is 6;
l: number of rigid bodies (including the fixed base);
j: number of joints;
d_i: degrees of freedom offered by the i-th joint (1 for joint R or P, 2 for C and U, 3 for S).

5.5 The first proposed prototype

In order to test the feasibility of such proposal, a prototype of mobile solar roof, to be oriented only during parking hours, has been developed at the University of Salerno.[50]

The mobile roof has been designed as a parallel robot because referring to Eq.(58):

- the roof is considered in the space 3D: $\lambda=6$;
- The number of rigid bodies is 8 : the fixed base(the roof of the car), 3 slidings, 3 legs and the platform of the mobile roof;
- The number of joints is 9: 3 globular joints between the three legs and the mobile roof, 3 revolute joints between the legs and the slidings, 3 prismatic joints between the slidings and the rectilinear cams.

$$N_d=6(8-9-1)+(3\cdot1+3\cdot1+3\cdot3)=3 \quad (59)$$

So it is possible to affirm that for the orientation of this model, with 3 Dof, 3 movements must be established: the three movements are the three displacements generated by three separate motors, connected to a PLC

(Programmable Logic Controller). An algorithm in MATLAB generates the input for PLC, to realize the desired panel's orientation.

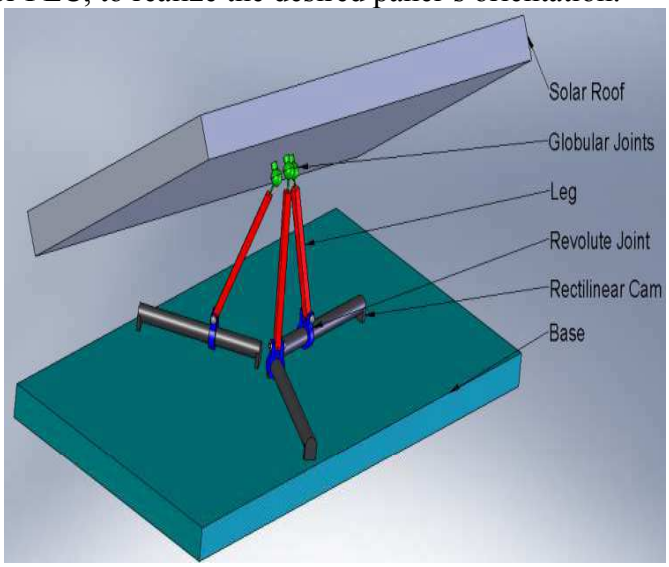

Figure 88 - The model of moving roof realized with Solid Works

The roof kinematic system is a 3-Dof triaglide PKM (Parallel Kinematics Machine) with constant leg length, actuated rectilinear cam joint on the base and a passive globular joint below the mobile roof, which is the tool center point of the PKM [54]. The rectilinear motion is allowed by a guided screw-nut system driven by DC motor. At the rest position, the slidings of rectilinear cams s_i have their minimum value, and the angle between axes of actuations and the legs has the value α_0. Such angle should be enough small to limit the height of the roof at rest, but should also ensure a sufficient lever arm to allow to start moving the roof.

The study of the roof has been performed through a kinematic model implemented in MATLAB, described in next paragraph and in references [51]. The model has also graphical capabilities (Figure 89). Moreover, VR (Virtual Reality) CAD simulation has been developed with SolidWorks (Figure 88)[55]. Both the models have been validated over the data measured on a small scale prototype (Figure 90).

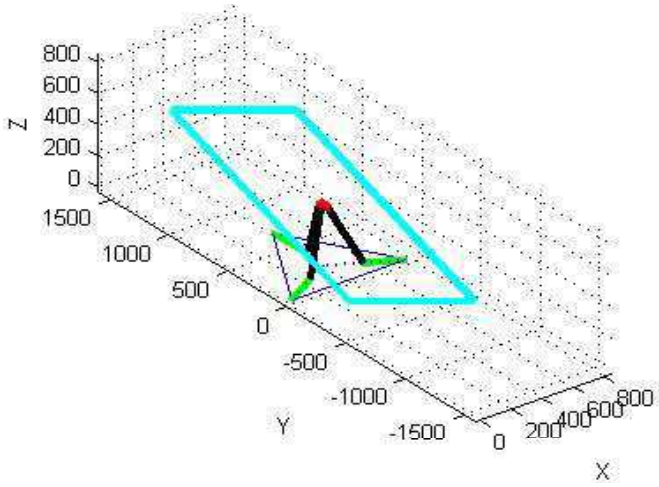

Figure 89 - Graphical output by the MATLAB model

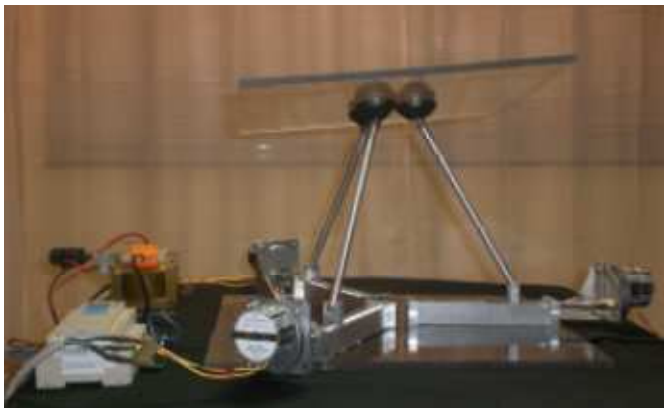

Figure 90 - Small scale prototype of moving solar roof

5.6 The kinematic model

In the following, the kinematic model of moving solar roof is presented. The geometry is defined in Figure 91 that represents the projection of the retractable roof on the horizontal plane. The variables are defined in the nomenclature. The coordinates of rectilinear cams can be computed through the following equations:

$$\begin{bmatrix} x_{s1} \\ x_{s2} \\ x_{s3} \\ y_{s1} \\ y_{s2} \\ y_{s3} \end{bmatrix} = \begin{bmatrix} x_{o1} \\ x_{o2} \\ x_{o3} \\ y_{o1} \\ y_{o2} \\ y_{o3} \end{bmatrix} + \begin{bmatrix} cos(30) & 0 & 0 \\ 0 & -cos(30) & 0 \\ 0 & 0 & 0 \\ sin(30) & 0 & 0 \\ 0 & sin(30) & 0 \\ 0 & 0 & -1 \end{bmatrix} \begin{bmatrix} s1 \\ s2 \\ s3 \end{bmatrix} \quad (60)$$

while the coordinates of globular joints can be computed as:

$$\begin{bmatrix} x_{b1} \\ x_{b2} \\ x_{b3} \\ y_{b1} \\ y_{b2} \\ y_{b3} \\ z_{b1} \\ z_{b2} \\ z_{b3} \end{bmatrix} = \begin{bmatrix} x_{s1} \\ x_{s2} \\ x_{s3} \\ y_{s1} \\ y_{s2} \\ y_{s3} \\ 0 \\ 0 \\ 0 \end{bmatrix} + \begin{bmatrix} c1\,cos\,30 & 0 & 0 \\ 0 & -c2\,cos\,30 & 0 \\ 0 & 0 & 0 \\ c1\,sin\,30 & 0 & 0 \\ 0 & c2\,sin\,30 & 0 \\ 0 & 0 & -c3 \\ s1 & 0 & 0 \\ 0 & s2 & 0 \\ 0 & 0 & s3 \end{bmatrix} \begin{bmatrix} r1 \\ r2 \\ r3 \end{bmatrix} \quad (61)$$

In this equation, it is c1=cos(α1), c2=cos(α2), c3=cos(α3), s1=sin(α1), s2=sin(α2), s3=sin(α3). The center of mass position and the computed length of legs are:

$$\bar{C} = \frac{\overline{B1} + \overline{B2} + \overline{B3}}{3} \quad (62)$$

$$l_c(i,j) = \sqrt{(x_{bi}-x_{bj})^2 + (y_{bi}-y_{bj})^2 + (z_{bi}-z_{bj})^2} \quad (63)$$

The normal to the plane of the mobile roof is identified by three angles obtained in this way:

$$A=[x_{b1}y_{b1}1;x_{b2}y_{b2}1;x_{b3}y_{b3}1] \quad (64)$$

$$B=[z_{b1};z_{b2};z_{b3}] \quad (65)$$

$$k=A/B \quad (66)$$

$$\beta_{x,y,z}=\text{arctg}\big(k(1,2,3)\big) \quad (67)$$

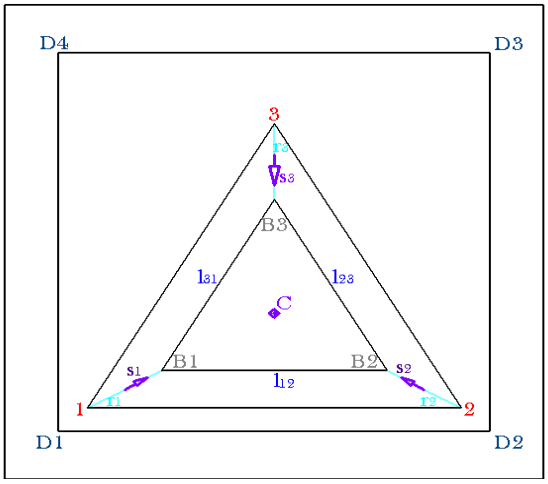

Figure 91 - Scheme of solar roof geometry

The roof geometry is evaluated by means of the kinematic model from (62) to (67) by solving a problem of constrained optimization:

$$min_x f(x) \quad (68)$$

subject to the constraints:

$$G_i(x) \leq 0 \quad (69)$$

And

$$E_i(x) = 0 \quad (70)$$

The six decision variables x are represented by the three sliding s_i of rectilinear cam and the three angles α_i between the axes of actuations and

their prismatic joint. The objective function f(x) to be minimized is the angle of incidence between the sun ray and the normal to the roof plane (Figure 8). The equality constraints E(x) express the condition that the computed values of the three legs $l_{ci,j}$ is equal to the assigned value l. The inequality constraints G(x) express the condition of no interference between i) the solar roof and the vehicle (i.e. the quote z should be greater than zero for all the points), and ii) between the legs and the solar roof. When the constraints (69)(70) are satisfied, the roof can be oriented exactly toward the sun, otherwise it would be oriented in the "best" way, to maximize the direct component of solar energy.

To know how to orient the mobile roof is necessary to compute declination δ and solar height α_s, as a function of latitude φ, hour angle ω, and year day N, presented in equations (4)(7)(8)(9)(10).

The direction of the sun ray, defined by angles $\beta_{x,opt}$ e $\beta_{x,opt}$, can be then computed as a function of the relative azimuth $\gamma_s - \gamma_v$ between sun and vehicle:

$$A_1 = \cos(\alpha_s) \cdot \sin(\gamma_s - \gamma_v) \quad (71)$$

$$B_1 = \cos(\alpha_s) \cdot \cos(\gamma_s - \gamma_v) \quad (72)$$

$$C_1 = \sin(\alpha_s) \quad (73)$$

$$\beta_{x,opt} = \operatorname{arctg}\left(-\frac{A_1}{C_1}\right) \quad (74)$$

$$\beta_{y,opt} = \operatorname{arctg}\left(-\frac{B_1}{C_1}\right) \quad (75)$$

To orient the roof exactly toward the sun, these two angles must coincide with the angles formed by the normal of the roof.

The problem (68)-(70) is solved by means of classical 2nd order optimization algorithms (Augmented Lagrangian approach combined with Quasi-Newton algorithm), implemented in the optimization tool of MATLAB. Computational time is order of few seconds, on a Sony VAIO PC.

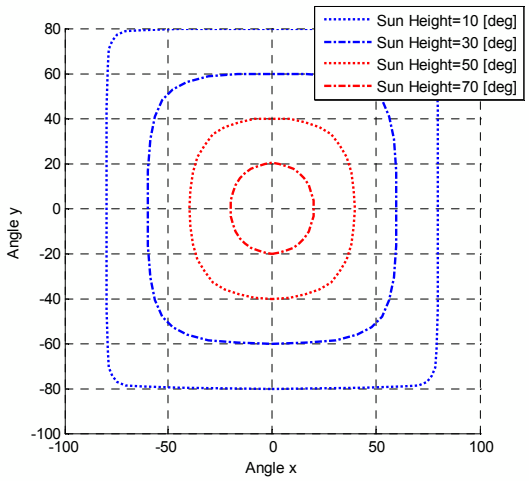

Figure 92 - Roof angles at different sun height

The position of the roof with respect to the vehicle can be characterized by the angles between the roof plane and the axes β_x and β_y (67), oriented toward vehicle width and length respectively (Figure 89). The angles corresponding to sun position at different sun height and for various orientations of the vehicle (relative azimuth of vehicle respect to sun) can be also computed by (74) and (75). Obviously, the orientation toward lower values of sun height (at daylight or sunset, or at high latitudes) requires actuating higher values of roof angles (Figure 92). It can be also observed that at higher sun height the curves are almost circular, and tend to be square at lower values.

5.7 Study and optimization of roof geometry

A systematic study has been carried out to observe the effects of the geometric variables on the performance of the roof, in terms of its capability to be oriented toward a large angular range. The study has been performed by determining numerically the limit conditions corresponding to incipient interference (i.e. $G_i(x)=0$) for various angles.

The calculation of this limit angles has been made for different geometry of the mobile roof: for each geometry represented in next

figure, it took about 7 minutes, with a PC Intel(R) Core(TM) i7 CPU 920 @2.67GHz, 8183 MB RAM.

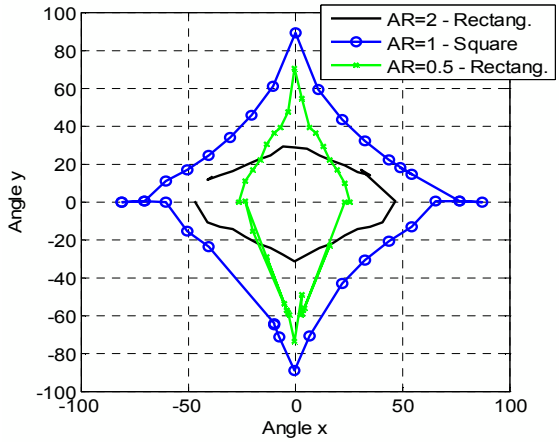

Figure 93 – Effects of aspect ratio

In terms of aspect ratio AR, defined as the ratio between roof length and width, the best results are obtained when the dimensions of the roof are equal (AR=1), while for a rectangular shape a smaller angular range can be reached (Figure 93).

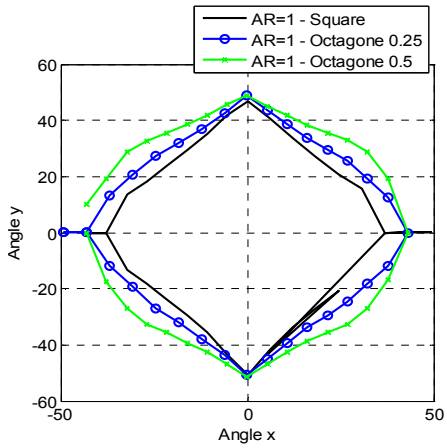

Figure 94 – Effects of beveling

The interference with the vehicle occur in correspondence of the roof vertices. The adoption of beveling can therefore allow reaching a larger angular range (Figure 94). Of course, beveling also reduces the net area for solar panels. Therefore, these aspects have to be examined jointly. The effect of the length of legs ***r*** and of the distance between the globular joints ***l*** has been studied. The best results are obtained with the highest values of ***r*** and the smallest values of ***l***, compatibly with space constraints and the stability of the roof (Figure 95).

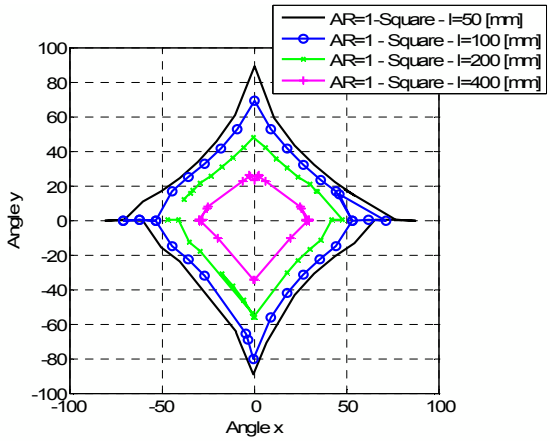

Figure 95 – Effects of the distance between the globular joints

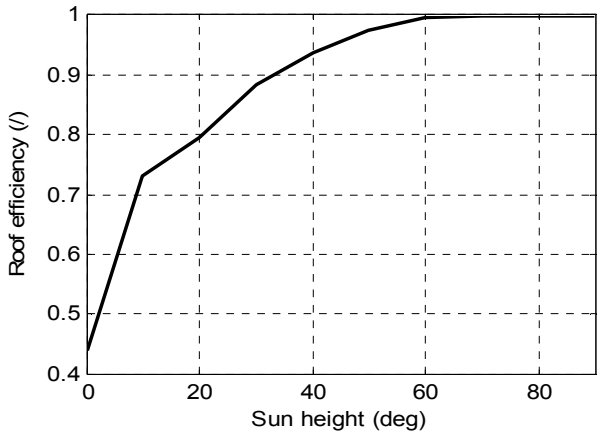

Figure 96 – Average roof efficiency vs. sun height

In order to characterize each roof in terms of energy efficiency, the mean value of cos(θ) can been evaluated for different values of solar height. Since optimal vehicle orientation (i.e. azimuth) could not be realized in most practical cases, due to space constraints in the parking places, for each sun height the efficiency is averaged over all azimuth angles, from 0° to 360°. An example corresponding to rectangular roof shape is shown in Figure 96.

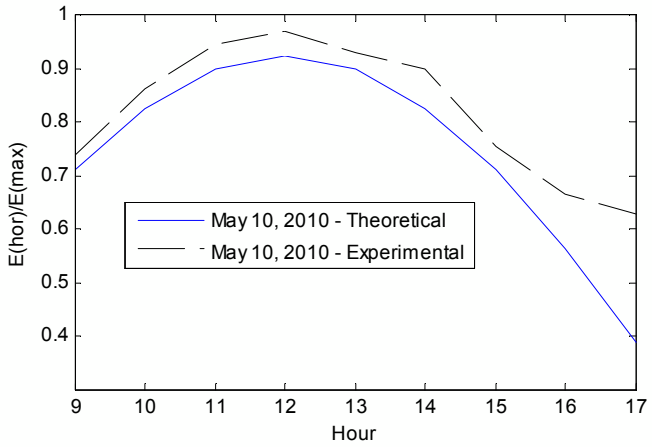

Figure 97 – Energy fraction at horizontal position. Theoretical vs experimental values (Fisciano, May 2010).

It has to be remarked that the ratio between energy taken at horizontal position and the maximum one is not necessarily equal to the value provided by Eq. (17), since diffuse and reflected components may be present, and also since kinematic constraints may prevent from reaching optimal orientation. A comparison of theoretical and experimental values, obtained by a pyranometer mounted on the roof prototype Figure 90 is presented in Figure 98. It can be observed that, although the trends are similar, some significant differences can occur, particularly at lower sun height (late afternoon).

5.8 Simulation over hourly solar data

Finally, a detailed analysis of the expected benefits of a moving solar roof has been performed by using hourly solar data available for different US cities [56].

The database provide the measured net power for a 2-axis tracking roof and for a fixed roof at horizontal position. For each hour, the sun height is evaluated, and the average roof efficiency with respect to the ideal 2 axis roof computed by the relative efficiency curve (Figure 96). The comparison of the energy collected on monthly basis in Los Angeles, normalized respect to its maximum value, is presented in Figure 98, while an analysis on yearly basis for four different locations at various latitudes is shown in Table 12. The results demonstrate that the proposed moving solar roof, even taking into account the kinematic constraints that do not allow perfect orientation, allows a significant gain in energy with respect to the horizontal panel, approaching the ideal 2 axis solution. The gain with respect to horizontal position range from 30% at low latitudes up to 47% at highest ones.

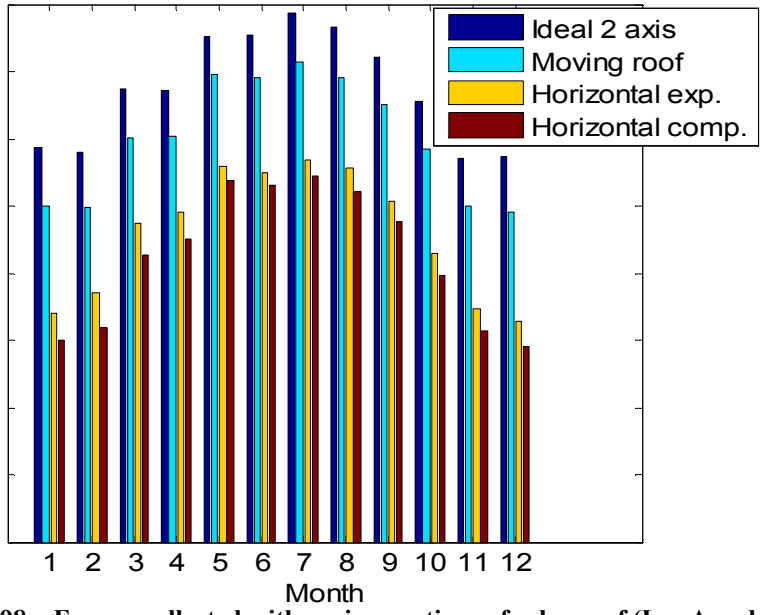

Figure 98 – Energy collected with various options of solar roof (Los Angeles, 1988)

Location	Latitude	A	B
Honolulu	21.33	46.57	30.70
Los Angeles	33.93	48.48	34.38
Chicago	41.78	52.27	35.83
Anchorage	61.17	78.74	46.89

Table 12 – Yearly percent gain with respect to horizontal position for ideal two axis (A) and real mobile roof (B)

It is timely to remark that these results have been obtained with a roof of rectangular shape, without beveling, which efficiency is shown in Figure 96. Even better results are expected by adopting an optimized geometry, as discussed in previous paragraphs. A trade-off between the benefits due to better orientation properties and the reduction in solar surface due to beveling and to the adoption of a non-rectangular shape should be also performed. It emerges that the design of the solar roof would be strictly connected to the design of the vehicle itself, impacting on its dimensions and shape, as well as on weight, aerodynamics and, of course, fuel consumption, emissions and cost.

5.9 Mechanical energy required to actuate solar roof motion

According to the roof kinematics and the involved mechanisms introduced in paragraphs 5.5 and 5.6, the contact along the screw/nut surfaces in relative motion may be analyzed by means of forces projection on a sloped plane with respect to the screw axis. Say ω the rotational speed of the screw, M_m the DC motor torque, r_m the screw radius, the following calculation of the mechanical work required for a general s_1-s_2 stroke of the leg base slider may be performed:

$$L_m = \int_{\theta(s1)}^{\theta(s2)} M_m(\theta)\,d\theta = \int_{\theta 1}^{\theta 2} F(\theta) r_m \tan(\alpha+\varphi)\,d\theta = r_m \tan(\alpha+\varphi) \int_{\theta 1}^{\theta 2} \frac{W_L(\text{roof\_orientation})}{\cos\beta(\text{roof\_orientation})}\,d\theta \quad (76)$$

Say μ and φ the friction coefficient and the friction angle ($\mu = \tan\varphi$) respectively, by taking into account the design constraints, the need to

achieve an irreversible mechanism and boundary lubrication regime between screw and nut, a good assessment of the mechanical efficiency of the transmission, with $\varphi \approx \alpha = 10°$ is given by:

$$\eta_{m=} \frac{\tan\alpha}{\tan(\alpha + \varphi)} \approx 0.48 \quad (77)$$

Assuming a motor speed of 100 rpm and a pitch of 3 mm, corresponding to a stroke of 300 mm in 60 s, a roof weight of 500 N, an axial force F equal about to 200 N, a mechanical work of about 460 J for each slider results by (75) and (76). Considering a roof energy gain equal to 30% and assuming an average power of 200 W for the solar roof in horizontal position, the energy spent to move the roof would be restored in about 23 s.

The evaluation of the mechanical work spent can be also integrated in to the roof model, to estimate the time required to restore the energy spent based on actual conditions. This feature will be used within the model based control depicted in the following paragraph, in order to decide if the roof should be actuated or not (for instance, this occurrence may result for low insulation in the late afternoon, and during night of course).

5.10 Toward a model based control of solar roof

The presented models represent the basis to develop a model based control system for the moving solar roof. It has been decided to move this roof only during parking phases because, in the prevailing use of such vehicles, most of solar energy is captured during parking time. The control scheme is being implemented on a small scale prototype of solar roof, actuated in LabVIEW by step motors.

The solar radiation is measured by a pyranometer mounted on the moving roof. A possible scheme, including both feed-forward and feedback control, is shown in Figure 99.

A GPS module provides vehicle position (latitude, longitude) and orientation (azimuth), and also actual date and time. The sun position (height, azimuth) is computed, and the optimal roof angles (β_x, β_y) that maximize direct solar energy are evaluated. The energy to be spent to move the roof is also estimated. Then, starting from the actual solar power and roof position, the minimum parking time to achieve a positive

gain in net energy is estimated. If the minimum parking time is lower than the expected duration of parking phase, the tracking system is actuated. The positions of rectilinear cams corresponding to the given angles (βx, βy) are read by a look-up table, previously computed by the presented kinematic model, and their values are actuated by the tracking system (step-by-step motors).

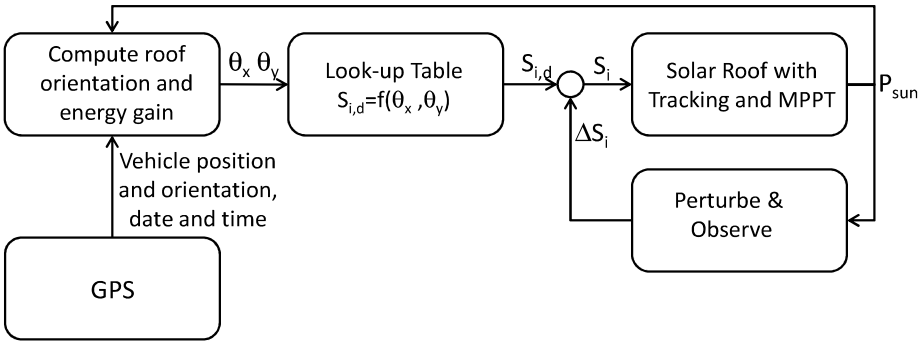

Figure 99 - Structure of solar roof control system

In real cases, it could happen that the position that maximizes the global energy may be different from the computed one, due to the presence of the diffuse and, possibly, of reflected energy. In this case, a P&O (Perturb and Observe) approach could be adopted. The measured values of solar power during the roof displacement from rest position to the predicted one can be utilized to identify a spatial model of solar power, so that to determine the optimal position of the roof taking into account all real world effects.

The best position can be of course found by processing the power data provided by PV panels, adopting for instance a Perturb & Observe approach. Of course, a suitable Maximum Power Point Tracking (MPPT) should be adopted, to maximize power extraction at each roof position[58][59][60].

But, since the PV panel provides a single maximum power data for a given roof position, it would be necessary to move the roof to perform such search. This method may lead to inefficient search, and therefore to

unnecessary energy consumption, in case that the relationship between position and power is complex, due to presence of clouds and obstacles.

In order to overcome these problems, it is proposed to combine the use of GPS data and of PV power data with use of a webcam, to detect the position of the sun. More in general, it should be decided if the solar roof has to be moved or not (for instance, this occurrence may result for low insulation in the late afternoon, and during night of course). The energy to be spent to move the roof is therefore estimated as a function of starting and final position, as shown in a previous paragraph 5.9 Eq. (76). Based on the estimate of maximum power achievable, the minimum parking time to obtain a positive gain in net energy is then computed.

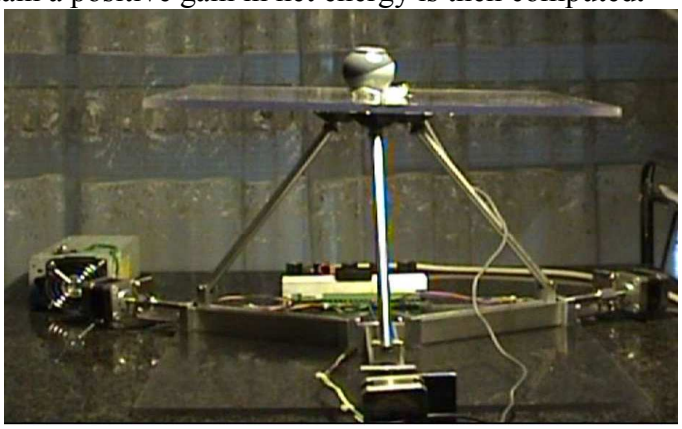

Figure 100 – Mobile solar roof prototype, moved by three step motors connected to a NI schedule and a webcam mounted in the middle of the roof.

If the minimum parking time is lower than the expected duration of parking phase, the tracking system is actuated.

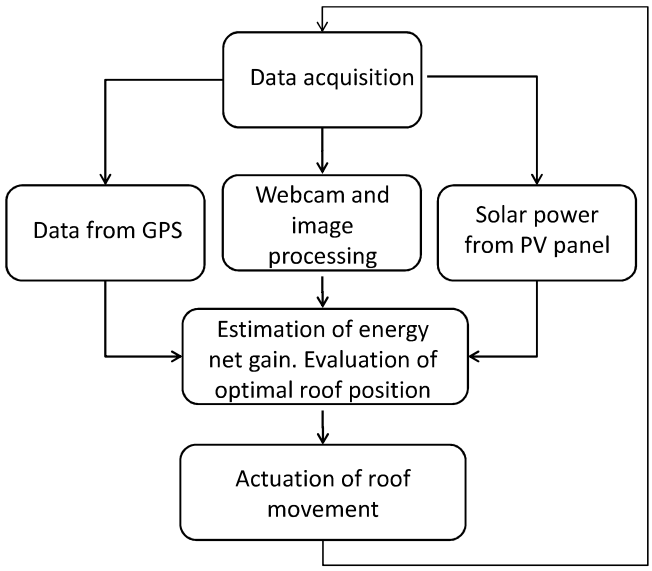

Figure 101 - Structure of solar roof control system

In this case, the roof angular position corresponding to maximum solar power is computed by the equations (78) - (82), and the relative positions of the slides are computed by a MATLAB module. Finally, the number of pulses for the step motors are computed and actuated by a LabVIEW module. When the target condition is reached, the process is repeated, to check if optimal position has been achieved.

5.10.1 The control through the use of a webcam

The digital camera (or webcam) is mounted in the center of the solar mobile roof, and takes a picture of the sky. The image data are processed by an algorithm in MATLAB, in order to compute the position of the sun and to estimate weather conditions.

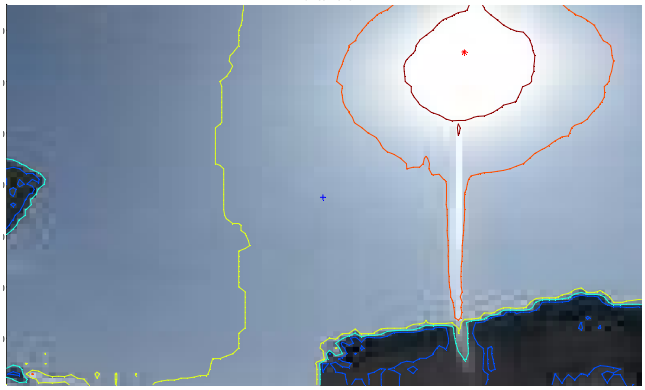

Figure 102 - Picture of the sky: sunny conditions.

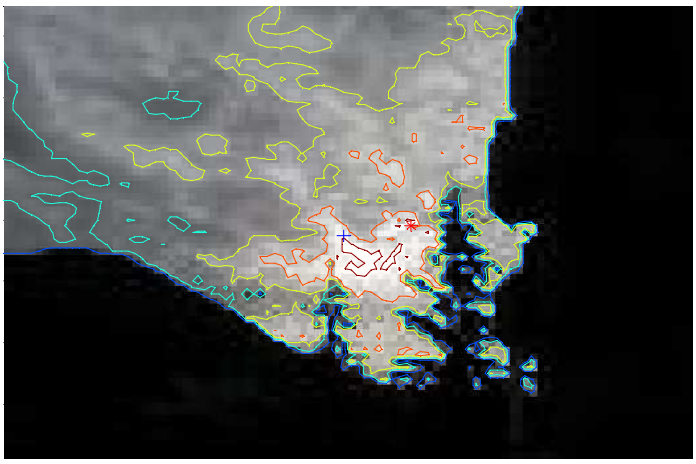

Figure 103 - Picture of the sky: cloudy conditions.

Typical pictures with sunny and cloudy conditions are shown in Figure 102 and Figure 103. The red symbol * (point R) indicates the center of mass of the points corresponding to maximum brightness and the blue symbol + (point B) indicates the center of the picture. Some iso-level curves of brightness are also plotted.

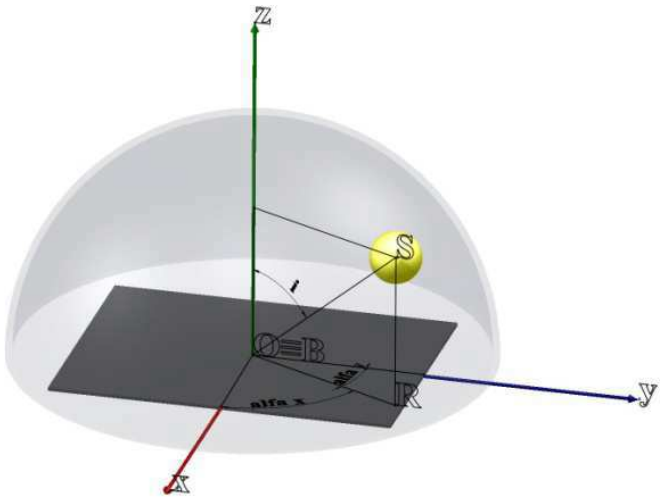

Figure 104 - Representation of solar roof and sun position.

In Figure 104, the gray plane coincides with the plane of the camera, fixed to the solar roof. The angle of incidence (signed with *i* in Figure 104) and the points B (center of the image) and R (maximum brightness), shown in Figure 102 and Figure 103, are also represented. The goal of the roof control is that the red and blue points (Figure 102 and Figure 103) must overlap, so that the direction of the normal coincides with the direction of the maximum brightness, and the solar power is maximized. The movement control can be achieved starting from the following geometric relationships:

$$\theta = \sin^{-1}\frac{\sqrt{x^2+y^2}}{\sqrt{2}} \quad (78)$$

$$\sin alfa_x = \frac{|x|}{\sqrt{x^2+y^2}} \quad (79)$$

$$\sin alfa_y = \frac{|y|}{\sqrt{x^2+y^2}} \quad (80)$$

$$\beta_x = -\theta \cdot \sin alfa_x \cdot sgn(x) \quad (81)$$

$$\beta_y = \theta \cdot \sin alfa_y \cdot sgn(y) \quad (82)$$

where x and y are the coordinates of R, θ is the angle of incidence, and β_x and β_y are the optimal values of the normal of the roof.

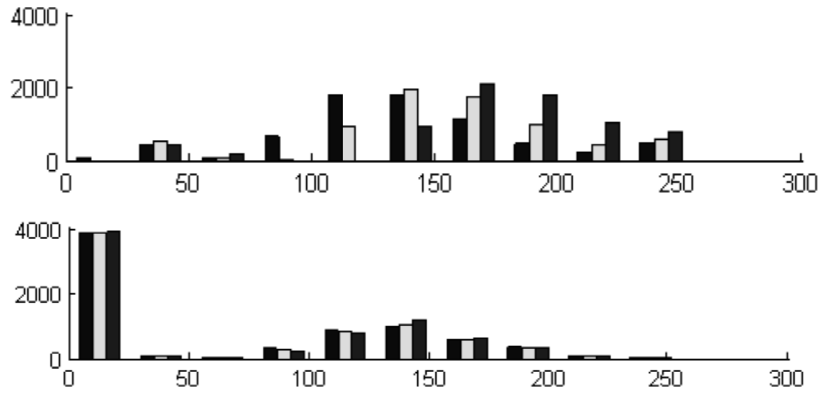

Figure 105 - Brightness distribution (0-255) for a grayscale, in sunny (upper) and cloudy (lower) conditions.

By processing image data, it is also possible to analyze sky conditions, in order to distinguish between sunny and cloudy weather, also to decide if solar roof should be moved or not. To this end, the distribution of brightness in a grayscale has been analyzed (Figure 105). It can be observed that in sunny conditions there is a higher number of pixels with high brightness, particularly for the medium gray color (3rd bar), while in case of cloudy conditions most of pixels have lower brightness values.

The pictures shown in Figure 102 and Figure 103 have been taken by a digital camera at high resolution and then reduced to low resolution (100x75 pixels), in order to reduce computational time. This resolution, compatible with low cost webcams, seems sufficient to extract useful information from the pictures, while computational time needed for image processing is less than 0.5 s, compatible with the exigencies of real-time control. Further studies have to be done to choose a webcam of adequate optical properties, compatible with outdoor use, and of limited cost.

5.11 Evaluation of net energy

In order to decide if the solar roof should be moved or not, it is necessary to compare the amount of energy required to achieve a specific orientation of the roof and the gain of solar energy between the optimal orientation and the actual position (the horizontal one when the vehicle is parked, and generally the previous one when the position should be updated). According to the roof kinematics and the involved mechanisms, it is possible to estimate the energy necessary to orient the roof.

Some experimental tests have been performed with the small scale mobile solar roof prototype. A pyranometer mounted in the middle of the roof measures the solar radiation at different hours, at horizontal position and at the optimal position, estimating the solar power gain P_g achievable by orienting the roof. The energy consumption E_M to move the step motors to the optimal position has been then measured (each motor has a nominal power of 4,8 W and a speed of about 1 mm/s). Therefore, the minimum time required to recover the energy spent for the orientation has been computed:

$$t_r = \frac{E_M}{P_g} \qquad (83)$$

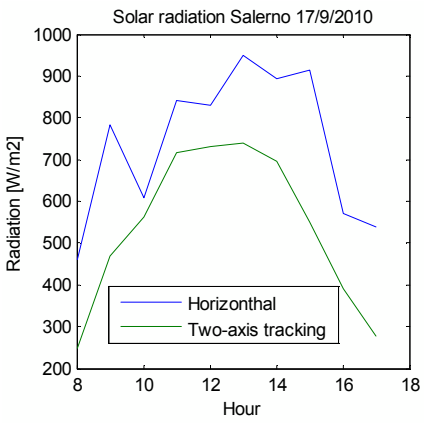

Figure 106 - Gain of solar energy compared to energy spent for the orientation during a partially cloudy

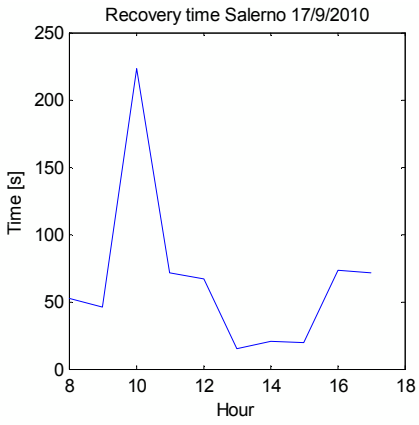

Figure 107 - Recovery time measured during a partially cloudy day 17/09/2010

day, 17/09/2010.

In Figure 106 the experimental values measured in a partly cloudy day at different hours are presented, while the minimum recovery time computed by (84) is presented in Figure 107.

The solar power gain (green line) is always positive, and reaches its minimum value at 10 AM, due to presence of clouds, where the recovery time is the maximum one (about 4 minutes). It could also be considered that, before the next starting of the vehicle, the mobile roof should return back to the horizontal position, with an additional energy consumption that, in our case, is almost equal to the energy consumption needed to reach the optimal position: the values presented in Figure 107 should be therefore doubled, so that the maximum recovery time in this case would be about 8 minutes. Considering that a PV assisted vehicle, in a typical urban use, should be parked for most of the day, it emerges that the recovery time can be considered almost negligible, thus confirming the convenience of a mobile solar roof.

5.12 Tracking strategy

An optimal sun tracking strategy has to be determined by maximizing the net energy received from the sun, considering the energy spent to move the roof. The mechanical energy spent can be expressed as the sum of a fixed term E_0^m, independent from trajectory, and a term E_1^m depending on the specific trajectory. The quantity E_0^m has a strong impact on the evaluation of the minimum time between successive roof actuation. The assessment on this energy amount required by each solar roof actuation, in its initial part, may be split into the analysis of three shares along the acceleration ramps of the electric motors, i.e. from each trajectory launch to motor steady speed conditions [62][63]:

- the electromechanical loss dissipated in motor armature resistance;
- the losses in the kinematical pairs due to the sliding/rolling friction in the mechanical pairs;
- the kinetic energy variation during start-transient.

The variable term E_1^m is roughly proportional to the distance from the initial and final roof positions and therefore to the incidence angle i, which in turn depends on the difference in sun height α_s and azimuth ϕ between starting and final positions:

$$E^m(\bar{t},\bar{t}+\Delta t)=E_0^m+E_1^m(\Delta\alpha,\Delta\Phi) \quad (84)$$

The term E_0 has been experimentally set to 5 J, for the prototype of solar roof shown in Figure 100. The term E_1^m corresponding to the entire day has been estimated 4.32 kJ, according to the considerations presented in the previous paragraph.

The tracking strategy requires the choice of two variables: the time interval Δt before next orientation, and the best roof orientation. In fact, if the roof has to be moved at discrete intervals, the best orientation during the interval (t, t+Δt) does not necessarily coincide with the optimal orientation at the time t. A simulation analysis has been performed starting from the solar irradiance captured by a fixed horizontal panel and a tracking one in ideal condition (clear sky) in Salerno (Figure 108). The power losses with respect to continuous tracking have been evaluated in two different cases (Figure 109): the back line has been obtained by orienting the solar roof at the start $\bar{t}$ of each interval (Δt = 1 hour), while the red line has been obtained by orienting the roof according to the optimal position that would be achieved at the half of the interval, i.e at $t=\bar{t}+\Delta t/2$: it is evident that the losses are much lower in the latter case.

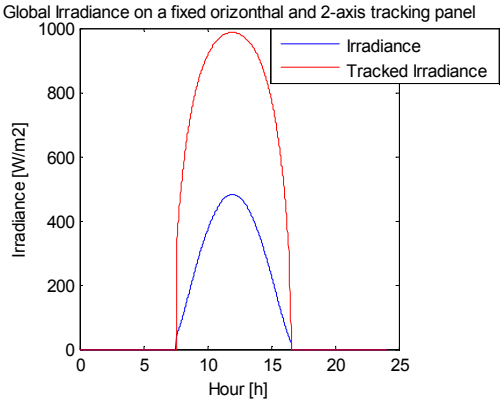

Figure 108 - Global irradiance in Salerno 15th January clear sky

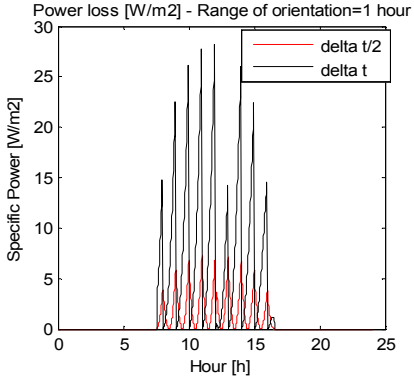

Figure 109 - Solar power losses during a day for two different

optimal orientation cases.

Therefore, the optimal time interval Δt before next orientation can be found by minimizing the sum of two terms:

- the solar power losses, expressed as the difference between the solar power that could be captured by a continuous tracking $\dot{E}_t^S(t)$and the solar power $\dot{E}_{\bar{t}+\Delta t/2}^S(t)$captured when the roof is at the fixed position corresponding to time $\bar{t} + \Delta t/2$;
- the mechanical energy (per unit time) $E^m(\bar{t}, \bar{t} + \Delta t)$ spent to move the sun roof from the optimal position at time $\bar{t}$ to the optimal position at time $\bar{t} + \Delta t$ e /2;

$$\min_{\Delta t} \frac{\int_{\bar{t}}^{\bar{t}+\Delta t} \left[\dot{E}_t^S(t) - \dot{E}_{\bar{t}}^S(t)\right] dt + E^m(\bar{t},\bar{t}+\Delta t)}{\Delta t} \quad (85)$$

The actual solar power is in general lower than the optimal one, obtained by continuous tracking. If only direct radiation is considered, the following relationship holds:

$$\dot{E}_{\bar{t}}^S(t)dt = \dot{E}_t^S(t)dt \cdot \cos\theta \quad (86)$$

where θ represents the incidence angle.

The solar power losses have different values along the day, being influenced by solar irradiance and by its gradient. The optimal time interval between two orientations is lower in the morning and in the late afternoon, and achieves higher values around noon, as shown in Figure 110.

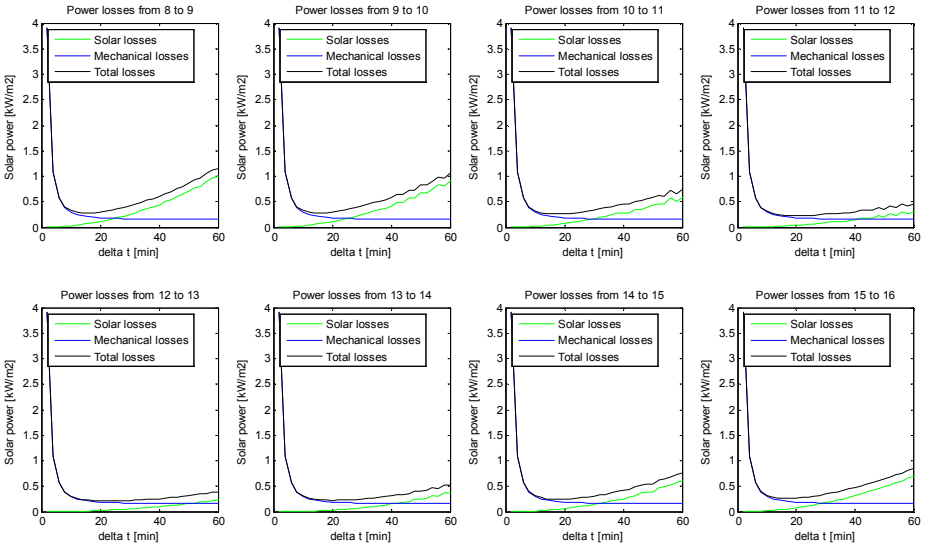

Figure 110 - Mechanical and solar losses during a day.

In Figure 111, the optimal time intervals during the day at different seasons (15th August and 15th January) and weather conditions are presented. The time interval varies by a factor two, and achieves the highest values at noon during cloudy days in the winter. It is therefore advisable to adopt the presented tracking strategy, in order to maximize the benefits of a mobile solar roof in solar assisted vehicles.

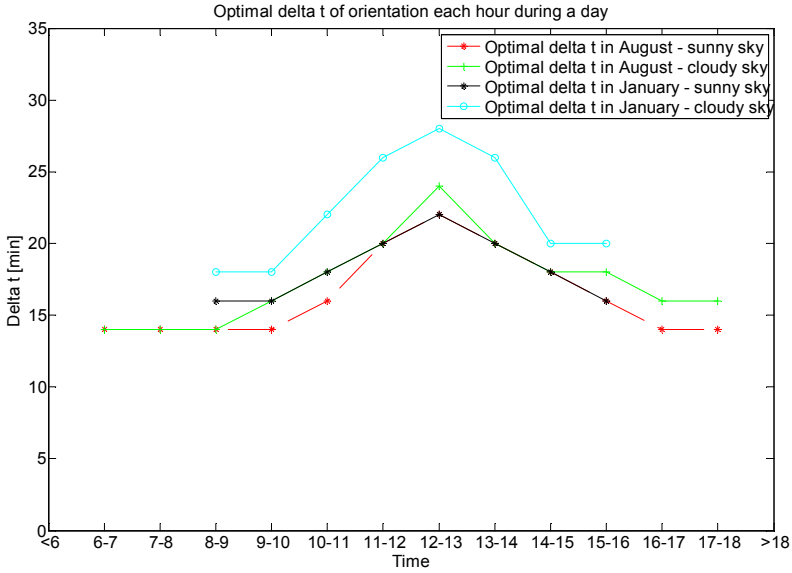

Figure 111- Optimal b Δt between two different of orientation considering months of opposite seasons (August and January) and for different weather conditions (sunny and cloudy day).

CHAPTER 6

6 Conclusions and future developments

6.1 Conclusions

Now days there is a growing attentions on sustainable mobility: traditional cars use fossil fuels that, as it has just been explained in Chapter 2, tend to finish, the oil price tends to grow and it is subject to unpredictable oscillations.

For this and many other reasons, largely explained in this work, a big interest has been developed for HEV; but in recent years HSV are attracting increasing interest. The last ones use solar energy that is a kind of energy gratis, largely diffused and unlimited. But there is a great difference between hybrid solar vehicles and solar cars: in fact solar cars now do not represent a realistic alternative for traditional cars, because they do not have a sufficient range, depend on sun availability and have high costs. Instead HSV do not have problems concerning the autonomy range, because they have an electric motor and also a traditional combustion engine.

These elements explain why the present research activity is focus on HSV, especially on two different aspects: the energy management applied on the HSV prototype developed at University of Salerno realized by the optimization strategy called Rule Based strategy, and the development of a mobile solar roof for vehicle applications to have a bigger gain of solar energy.

6.1.1 Conclusions for the RB energy management

In Chapter 3 the main optimization strategies have been presented: dynamic programming, genetic algorithm and Rule-Based strategy. The first two strategies have some difficulties so, for the optimal energy management of the HSV prototype, the last strategy has been adopted.

First of all Rule-Based methodology has been presented. Suited numerical procedures were set-up to develop heuristic rules aimed at

varying the Start & Stop strategies of the ICE-EG system as function of expected traction power demand and solar radiation.

The developed control architecture consists of two main loops. The outer level (i.e. external loop) estimates, on a daily time base, the final state of charge to be reached at the end of the driving cycle. This way, it is ensured that the battery will fully recover the solar energy captured during the following parking phase. At the inner level (i.e. the internal loop) real time estimation of quasi-optimal EG power and SOC deviation as function of current power demand and expected solar irradiation is performed.

Extensive simulations were carried out to test the proposed RB strategy. The potentialities offered by this approach were successfully demonstrated via comparison with fuel savings evaluated by means of genetic-algorithm-based optimization of ICE scheduling on the same driving cycle (i.e. ECE-EUDC). The numerical analyses also indicates that RB achieves satisfactory performance even without predicting future power demands. Of course, the availability of forecasting models will guarantee further improvement of RB performance.

The comparison with Dynamic Programming has not been done especially because DP optimization is very articulated with math expressions.

6.1.1.1 Benefits for an HSV in the use of look-ahead capabilities

In Chapter 4 a method to maximize the benefits obtainable with Hybrid Solar Vehicles, with more advanced look ahead capabilities has been presented and also the obtained experimental results have been shown.

In particular, the optimum compromise between two potentially conflicting aspects should be realized: i) to leave as much as possible room in the battery for solar recharge and ii) operate in a favorable battery SOC range in terms of energy losses and life cycle. The future recourse to V2G technology would reduce but not remove the need to estimate the net incoming energy. Simulation results at different months and locations have shown that the estimation of the incoming solar energy in next parking phase produces a more efficient energy management, with reduction in fuel consumption, particularly at higher solar radiation. It has also been analyzed how these benefits deteriorate themselves in presence of forecast inaccuracy. It has also been studied how measured solar

power is correlated to cloud cover, using a software tool available on-line. The results show that there is a significant scatter between the measured data and the data estimated by a regression line as a function of mean cloud cover, particularly when this index ranges from 30 and 50%. Anyway, the simulations performed have shown that the adoption of solar energy prediction can give interesting benefits on fuel economy even in presence of forecast errors within 10-15%.

6.1.1.2 Experimental validation of RB strategy applied at the prototype of HSV

In chapter 4 some experimental results obtained by the application of a since the results previously developed Rule-Based control strategy on a prototype of series hybrid solar vehicle developed at the University of Salerno have been presented. The strategy has been first successfully tested via simulation analysis, by comparing fuel economy obtained with the application of RB strategy with the best results of two extensive parametric analyses: fuel consumptions obtained through the application of RB strategy have been compared with two best results of parametric analysis and since the results are quite similar, the adoption of RB strategy is convenient because, first of all is more direct and rapid.

The RB strategy has been then implemented on the prototype through the development of a LabVIEW algorithm, which has been then embedded into a NI cRIO platform. Preliminary experimental tests highlight the high potential of the developed experimental test-bench to exhaustively investigate and further improve the proposed heuristic strategy.

6.1.2 Conclusions on the mobile solar roof

The adoption of a moving solar roof for vehicle applications can substantially enhance the energy recovered during parking phases, for a solar electric or hybrid vehicle. Moreover, this system can result particularly useful at high latitudes, where an horizontal panel would be strongly penalized by low sun height. The adoption of a moving roof can therefore extend the potential market of solar assisted vehicles.

6.1.2.1 Solar roof geometry

The kinematic model presented has allowed the optimization of roof geometry and shape. The best orienting properties are reached with shapes approaching a circular one, and with the minimum distance

between globular joints. The optimal solution has been determined by an integrated analysis of both roof and vehicle shape.

The control system structure for real-time solar tracking in feed-forward and feedback mode has been also described. Economic feasibility with encouraging results has been also considered.

6.1.2.2 Model based control of the mobile solar roof

In order to maximize benefits of the mobile solar roof, the energy consumption related to its movement must be minimized, and unnecessary movements avoided. To this end, a control procedure based on the use of insulation data provided by the solar panel, information derived by a GPS module and by processing the sky images taken by a webcam has been presented. The webcam has been placed in the middle of the mobile platform of the prototype, it makes a picture of the sky; in this picture two points are signed: the center of the picture and the center of mass of the points with maximum brightness. The main idea is that the center of the picture tends to go on the center of mass of the points of maximum brightness.

6.1.2.3 Computation of the best interval between two orientations

A model based control system has been developed, implemented in LabVIEW and tested on a small scale prototype with artificial light conditions. Procedures to estimate the minimum recovery time and an optimal tracking strategy have been presented and applied over a set of experimental data.

The mobile roof has been design not as a tracking solar roof but as a parallel robot which takes the best orientation at discrete time intervals. The conclusion is that during the day the interval between two different orientation changes, and it is convenient to orient the roof in the middle of each intervals, that means that if it has been computed that the best interval at 9.00 a.m. is one hour, there is a bigger gain of solar energy if the roof is oriented at 9.00 a.m. with the best orientation of 9.30 a.m. until 10a.m. and so on.

6.2 Future works

In next future the research activity concerning Rule-Based strategy and the mobile solar roof applied on HSV will continue to be developed.

6.2.1 Future works for RB strategy

1. The development of a method to maximize the benefits obtainable with Hybrid Solar Vehicles using advanced look ahead capabilities, the study of other specialized tools for solar power prediction recently available on the market, in order to assess their accuracy, will be analyzed. Moreover, the study, performed on a Lead-Acid battery, will be extended to other type of batteries, as Lithium Ion, also considering more articulate scenario's, including random variations in driving cycle profile, length and parking time.
2. About the application of RB strategy on the prototype of HSV developed at University of Salerno, future work will focus, on one hand, on extending the numerical analyses to other driving cycles and/or HSV architecture and, on the other hand, on further testing the correspondence of real fuel consumption measured on the vehicle and the ones obtained by a simulator developed in LabVIEW.

6.2.2 Future works of the mobile solar roof

1. Until now only a small scale prototype has been developed, so in next future the first thing to do will be the evaluation of the feasibility of such solution on vehicle.
2. Further developments are in progress to integrate the estimation of the optimal tracking strategy in the control system and to validate the control system in outdoor at different sky conditions.
3. Another idea is the realization of a different mobile system to make a comparison in terms of the range of angles obtained by the roof, in terms of energy spent to orient it and last but not least an economic valuation and comparison will be done.

BIBLIOGRAPHY

[1] Robert Foster, Majid Ghassemi, Alma Cota, "Solar energy, renewable energy and environment", Energy and Environment series, Series editor, Abbas Ghassemi, CRC Press Taylor & Francis Group.

[2] Quaschning V. (2003), "Technology fundamentals - The sun as an energy resource". Renewable Energy World 6 (5): 90–93.

[3] http://www.energysavers.gov

[4] Hammad M., Khatib T. (1996), Energy Parameters of a Solar Car for Jordan, *Energy Conversion Management*, **V.37**, No.12.

[5] Wellington R.P. (1996), Model Solar Vehicles Provide Motivation for School Students, *Solar Energy* **Vol.58**, N.1-3.

[6] Saitoh, T.; Hisada, T.; Gomi, C.; Maeda, C. (1992), Improvement of urban air pollution via solar assisted super energy efficient vehicle. *92 ASME JSES KSES Int Sol Energy Conf.* Publ by ASME, New York, NY, USA.p 571-577.

[7] Sasaki K., Yokota M., Nagayoshi H., Kamisako K. (1997), Evaluation of an Electric Motor and Gasoline Engine Hybrid Car Using Solar Cells, *Solar Energy Material and Solar Cells* (**47**), 1997.

[8] Seal M.R. (1995), Viking 23 - zero emissions in the city, range and performance on the freeway. *Northcon - Conference Record 1995. IEEE, RC-108*.p 264-268.

[9] Seal M.R., Campbell G. (1995), Ground-up hybrid vehicle program at the vehicle research institute. Electric and Hybrid Vehicles - Implementation of Technology *SAE Special Publications n 1105 1995*.SAE, Warrendale, PA, USA.p 59-65.

[10] S.Letendre, R.Perez, Christy Herig, Vehicle Integrated PV: a Clean and Secure Fuel for Hybrid Electric Vehicles, *Proc. of Annual Meeting of the American Solar Energy Society, June 21-26, 2003, Austin, TX*.

[11] Arsie I., Graziosi M., Pianese C., Rizzo G., Sorrentino M. (2004), Optimization of Supervisory Control Strategy for Parallel Hybrid Vehicle with Provisional Load Estimate, *Proc. of AVEC04*, Arhnem (NL), Aug.23-27, 2004.

[12] http://ww.itee.uq.edu.au/~serl/UltraCommuter.html

[13] Arsie I., Di Domenico A., Marotta M., Pianese C., Rizzo G., Sorrentino M. (2005); *A Parametric Study of the Design Variables for a Hybrid Electric Car with Solar Cells,* Proc. of METIME Conference, June 2-3, 2005, University of Galati, RO.

[14] Arsie I., Marotta M., Pianese C., Rizzo G., Sorrentino M. (2005); *Optimal Design of a Hybrid Electric Car with Solar Cells,* Proc. of 1st AUTOCOM Workshop on Preventive and Active Safety Systems for Road Vehicles, Istanbul, Sept.19-21, 2005.

[15] http://www.nrel.gov

[16] Wakefield, E. H. (1998), History of the electric automobile: Hybrid electric vehicles, Society of Automotive Engineers.

[17] Trum mel, M. and Burke, A. (1983), 'Development history of the hybrid test vehicle', Vehicular Technology, IEEE Transactions on 32(1), 7 – 14.

[18] Plache, L. (2011), Auto sales forecast 2011, Technical report, Edmunds.com: Auto Observer.

[19] Donitz, C., Vasile, I., Onder, C. and Guzzella, L. (2009), 'Modeling and optimizing two and four stroke hybrid pneumatic engines', Proceedings of the Institution of Mechanical Engineers, Part D 223(2), 255–280.

[20] Arsie I., Rizzo G., Sorrentino M. (2006 I), Optimal Design of a Hybrid Solar Vehicle, *AVEC06 - 8th* Intl. Symp. on Advanced Vehicle Control – August 20-24, 2006 - Taiwan

[21] Arsie I., Rizzo G., Sorrentino M., Petrone G., Spagnuolo G., Cacciato M., Consoli A. (2006 II) "Hybrid Vehicles and Solar Energy: a Possible Marriage?", In: Proc. of the International Conference on Automotive Technology ICAT. Instanbul (TR), 26 November 2006.

[22] Letendre S., Perez R., Herig C. (2003), Vehicle Integrated PV: A Clean and Secure Fuel for Hybrid Electric Vehicles, Proc. of the American Solar Energy Society Solar 2003 Conference, June 21-23, 2003, Austin,TX.

[23] www.itee.uq.edu.au/~serl/UltraCommuter.html

[24] Cheng W.K. and Santoso H., Mixture Preparation and Hydrocarbon Emissions Behaviors in the First Cycle of SI Engine Cranking. SAE paper 2002-01-2805.

[25] Zavala J.C., Sanketi P.R., Wilcutts M., Kaga T., Hedrick J.K., Simplified Models of Engine HC Emissions, Exhaust Temperature

and Catalyst Temperature for Automotive Coldtsart. 5th IFAC Symp.on Advances in Automotive Control, Aptos (USA), August 20-22, 20070.

[26] Arsie I., Pianese C., Rizzo G., Models for the Prediction of Performance and Emissions in a Spark Ignition Engine- A Sequentially Structured Approach. SAE 980779, SAE 1998 Transactions - Journal of Engines, Section 3, Vol. 106, pp. 1065-1079.

[27] Sciaretta, A., Guzzella, L. and Onder, C.H. (2003) `On the power split control of parallel hybrid vehicles: from global optimization towards real-time control', Int. J. of Automatisierungstechnik, Vol. 51, No. 5, pp.195±205

[28] Koot, M.W.T., Kessels, J.T.B.A., De Jager, A.G., Heemels, W.P.M.H., Van den Bosch, P.P.J. and Steinbuch, M. (2005) `Energy management strategies for vehicular power systems', IEEE-Transactions on Vehicular Technology, Vol. 54, No. 3, pp.771±782

[29] Scordia, J., Desbois-Renaudin, M.. Trigui, R., Jeanneret, B., Badin, F. and Plasse, C. (2005) `Global optimization of energy management laws in hybrid vehicles using dynamic programming', Int. J. of Vehicle Design, Vol. 39, No. 4, pp.349±367.

[30] Bellman, R.E. (1962) Dynamic Programming, Princeton University Press.

[31] Brahma, A., Guezennec, Y. and Rizzoni, G. (2000), Optimal energy management in series hybrid electric vehicles, in 'American Control Conference, 2000. Proceedings of the 2000', Vol. 1, pp. 60 –64.

[32] Kirschbaum, F., Back, M. and Hart, M. (2002), Determination of the fuel optimal trajectory for a vehicle along a known drive cycle, in '15th Triennial World Congress of the International Federation of Automatic Control'.

[33] Lin, C., Kang, J., Grizzle, J. and Peng, H. (2001), Energy management strategy for a parallel hybrid electric truck, in 'American Control Conference, 2001. Proceedings of the 2001', pp. 2878–2883.

[34] Lin, C., Peng, H. and Grizzle, J. (2004)," A stochastic control strategy for hybrid electric vehicles", in American Control Conference, pp. 4710–4715.

[35] Kolmannovsky, I., Siverguina, I. and Lygoe, B. (2002), "Optimization of powertrain operation policy for feasibility assessment and calibration: stochastic dynamic programming approach", in American Control Conference', pp. 1425–1430.

[36] Tate, E., Grizzle, J. and Peng, H. (2008), "Shortest path stochastic control for hybrid electric vehicles", International Journal of Robust and Nonlinear Control 18, 1409 – 1429.

[37] A. J. Chipperfield, P. J. Fleming, H. Polheim and C. M. Fonseca, "Genetic Algorithm Toolbox – MATLAB Tutorial", Department of Automatic Control and System Engineering - University of Sheffield.

[38] A. J. Chipperfield, P. J. Fleming and C. M. Fonseca, "Genetic Algorithm Tools for Control Systems Engineering", Proc. Adaptive Computing in Engineering Design and Control, Plymouth Engineering Design Centre, 21-22 September, pp. 128-133, 1994.

[39] E. Zitzler, "Evolutionary Algorithms for Multiobjective Optimization: Methods and Applications", Ph.D. Thesis, ETH Swiss Federal Institute of Technology, Zurich, Switzerland.

[40] Arsie I., Rizzo G., Sorrentino M. (2007) Optimal Design and Dynamic Simulation of a Hybrid Solar Vehicle, SAE TRANSACTIONS - JOURNAL OF ENGINES 115-3: 805-811.

[41] Arsie I., Di Martino R., Rizzo G., Sorrentino M. (2007) "Toward a Supervisory Control of a Hybrid Solar Vehicle" In: IFAC Symposium "Advances in Automotive Control" AAC07, August 20-22, 2007, Monterey (CA) Edited by: Elsevier.

[42] Arsie I., Di Martino R., Rizzo G., Sorrentino M (2008), "Energy Management for a Hybrid Solar Vehicle with Series Structure", Proc. of 17th IFAC World Congress, July 6-11, 2008, Seoul.

[43] Adinolfi G., Arsie I., Di Martino R., Giustiniani A., Petrone G., Rizzo G., Sorrentino M. (2008) "A Prototype of Hybrid Solar Vehicle: Simulations and On-Board Measurements", In: Proc.of Advanced Vehicle Control Symposium AVEC 2008, October 6-9, 2008, Kobe (Japan).

[44] Sakawa, M., Kato, K., Ushiro, S., Inaoka, M., 2001, "Operation planning of district heating and cooling plants using genetic algorithms for mixed integer programming", Applied Soft Computing Vol.1, pp. 139–150.

[45] Tona P., Gautier, P., Amari, R., 2008, “Modeling and Control of a Mild-Hybrid City Car with a Downsized Turbo-Charged CNG Engine”, In: Proc.of Advanced Vehicle Control Symposium AVEC 2008, October 6-9, 2008, Kobe (Japan).

[46] Rizzo, G., Sorrentino, M., Arsie, I. (2009). Rule-Based Optimization of Intermittent ICE Scheduling on a Hybrid Solar Vehicle. SAE paper 2009-24-0067.

[47] Burch, S., Cuddy, M., Johnson, V., Markel, T., Rausen, D., Sprik, S., and Wipke, K., (1999), "ADVISOR: Advanced Vehicle Simulator", available at: www.ctts.nrel.gov.

[48] Molyneaux A., Leyland G., Favrat D. (2003), Multi-Objective Optimization of Vehicle Drivetrains, 3rd Swiss Transport Research Conference, Monte Verita / Ascona, March 19-21, 2003.

[49] G. Coraggio, C. Pisanti, G. Rizzo, M. Sorrentino (2010), “Assessment of benefits obtainable in a Hybrid Solar Vehicle using look-ahead capabilities for incoming solar energy”. In: 10th International Symposium on Advanced Vehicle Control AVEC10, August 22-26 2010, Loughborough, UK Loughborough University Department of Aeronautical & Automotive Engineering & Transport Studies- ISBN 9780904947656.

[50] G. Coraggio, C. Pisanti, G. Rizzo, M. Sorrentino (2011),“Experimental validation of an heuristic strategy to optimize on-board energy management of a hybrid solar vehicle”, In: IFP Energies nouvelles, International scientific conference on hybrid and electric vehicles, RHEVE 2011, 6-7 December, Rueil-Malmaison.

[51] C. Pisanti (2008), “Sviluppo di un modello matematico di un tetto solare mobile per un veicolo ibrido solare”, University of Salerno, Italy 84084 Fisciano (Italy).

[52] Schnabel, F. (2009), Untersuchung der Einsatzmöglichkeiten und des Nutzens von solaren Systemen im Kraftfahrzeug, Institut für Arbeitswissenschaft und Technologiemanagement (IAT),Universität Stuttgart

[53] G. Legnani, “Robotica industriale”, Case Editrice Ambrosiana

[54] Tsai L. W. (1999), “Robot Analysis: the mechanics of serial and parallel manipulators”, John Wiley & Sons, Inc., USA.

[55] G. Coraggio (2008), “Progettazione di un tetto solare mobile per un veicolo ibrido solare”, University of Salerno, Italy 84084 Fisciano (Italy).
[56] www.nrel.gov/rredc/PVWATTS
[57] Coraggio G., Pisanti P., Rizzo G., Senatore A. (2010), ”A moving solar roof for a Hybrid solar vehicle”, 6th IFAC Symposium "Advances in Automotive Control", AAC10, July 11-14, 2010, Munich (Germany).
[58] Femia N., Lisi G., Petrone G., Spagnuolo G., Vitelli M. (2008), “Distributed Maximum Power Point Tracking of Photovoltaic Arrays. Novel Approach and System Analysis” IEEE Transactions on Industrial Electronics Vol. 55, No. 7, July 2008, pp. 2610 - 2621.
[59] Adinolfi G., Arsie I., Di Martino R., Giustiniani A., Petrone G., Rizzo G., Sorrentino M. (2008) “A Prototype of Hybrid Solar Vehicle: Simulations and On-Board Measurements”, Proc. AVEC 2008, Oct.6-9, 2008, Kobe (Japan) 917-922 Soc.of Automotive Engineers of Japan - ISBN: 978-4-904056-21-9.
[60] Femia N., Lisi G., Petrone G., Spagnuolo G., Vitelli M. (2008), “Analysis of Photovoltaic Systems with Distributed Maximum Power Point Tracking”, Proc. of IEEE International Symposium on Industrial Electronics ISIE08, June 30-July 2 2008 pp. 2408 - 2413.
[61] G. Coraggio, C. Pisanti, G. Rizzo, A. Senatore (2010), “Model Based Control of a Moving Solar Roof for a Solar Vehicle”. In: 10th International Symposium on Advanced Vehicle Control AVEC10, August 22-26 2010, Loughborough, UK Loughborough University Department of Aeronautical & Automotive Engineering & Transport Studies- ISBN 9780904947656.
[62] Chong Hui Kim and Byung Kook Kim, "Minimum-energy translational trajectory generation for differential-driven wheeled mobile robots," Journal of Intelligent and Robotic Systems, vol. 49, no.4, pp. 367-383, August 2007.
[63] Sergaki, E.S., Stavrakakis, G.S. & Pouliezos, A.D., “Optimal robot speed trajectory by minimization of the actuator motor electromechanical losses”, Journal of Intelligent and Robotic Systems, Vol. 33, No. 2, pp. 187-207, ISSN 0921-0296, 2002.

ACKNOWLEDGEMENTS

When you are asked "What are you doing?" and you say "I am a PhD student in Mechanical Engineering" very few people really know what you are doing. Then if they ask "And what is that really?" my answer becomes more complex as I feel compelled to tell my own experience: the doctorate is three years of study, research, application, and definitely rewarding after the master degree. The decision to take this path and the path itself has been entirely positive thanks also to many people to whom I wish to say thanks.

First of all, my first thank goes to my family, my mother, my father and my brother who always supported me in my choices and always gave me an extra boost when needed, obviously in different ways.

Definitely a special thanks goes to Professor Gianfranco Rizzo, from whom I learned many things, and all this experience is strictly connected to him: I would thank him for his professionalism and his knowledge, and also for his humanity; I has always trust in me, in my capacities and thank to him I have done some important international experiences .

I thank Professor Adolfo Senatore for his continuous willingness to give his help: he contributed to enlarge my capabilities thanks to his expertise and professionalism.

And I have to thank all members of the Lab I5: especially Gianpaolo Noschese, ing. Ivan Criscuolo, ing. Silvana Di Iorio, ing. Angelo Esposito, ing. Dario Marra, ing. Raffaele Petrone and Ing. Pierpaolo Polverino. During three years I lived with all these people in the laboratory in a friendly but professional, joyful but respectful way. To sum up I lived with them in a total positive climate.

Last but not least a big thanks goes to Ing. Gaetano Coraggio, my partner in life and study for almost 7 years, even this route was started, spent and finished together and I can say that the budget is totally positive. We advanced step by step together, we increased day by day and we have integrated our knowledge, and created a solid foundation in both business and interpersonal situations for our future.